Exploring 2D materials at surfaces through synchrotron-based core-level photoelectron spectroscopy

Luca Bignardi [a,*], Paolo Lacovig [b], Rosanna Larciprete [c], Dario Alfè [d,e], Silvano Lizzit [b], Alessandro Baraldi [a,b]

[a] *Department of Physics, University of Trieste, Via Valerio 2, 34127, Trieste, Italy*
[b] *Elettra Sincrotrone Trieste, Str. St. 14 Km 163.5 in AREA Science Park, 34149, Basovizza, Trieste, Italy*
[c] *CNR-ISC, Via Dei Taurini 19, 00185, Roma, Italy*
[d] *University College London, Gower Street, London, WC1E 6BT, United Kingdom*
[e] *Department of Physics, Università degli Studi di Napoli Federico II, Via Cinthia 21, 80126, Napoli, Italy*

ARTICLE INFO

ABSTRACT

The interest in understanding and controlling the properties of two-dimensional materials (2DMs) has fostered in the last years a significant and multidisciplinary research effort involving condensed matter physics and materials science. Although 2DMs have been investigated with a wide set of different experimental and theoretical methodologies, experiments carried out with surface-science based techniques were essential to elucidate many aspects of the properties of this family of materials. In particular, synchrotron-based X-ray photoelectron spectroscopy (XPS) has been playing a central role in casting light on the properties of 2DMs, providing an in-depth and precise characterization of these materials and helping to elucidate many elusive and intricate aspects related to them. XPS was crucial, for example, in understanding the mechanism of growth of several 2DMs at surfaces and in identifying the parameters governing it. Moreover, the chemical sensitivity of this technique is crucial in obtaining knowledge about functionalized 2DMs and in testing their behavior in several model chemical reactions. The achievements accomplished so far in this field have reached a maturity point for which a recap of the milestones is desirable. In this review, we will showcase relevant examples of studies on 2DMs for which synchrotron-based XPS, in combination with other techniques and state-of-the-art theoretical modeling of the electronic structure and of the growth mechanisms, was essential to unravel many aspects connected to the synthesis and properties of 2DMs at surfaces. The results highlighted herein and the methodologies followed to achieve them will serve as a guidance to researchers in testing and comparing their research outcomes and in stimulating further investigations to expand the knowledge of the broad and versatile 2DMs family.

1. Introduction

The family of two-dimensional materials (2DMs) is very broad and diverse, formed by many compounds that have attracted interests and incredibly stimulated research efforts in the last years. The possible implications of 2DMs in many sectors of science, ranging from electronics to optoelectronics, from catalysis to photovoltaics, are expected to revolutionize many sectors of technology. Therefore, the investigations about these materials have been conducted in an interdisciplinary way, involving experts in physics, chemistry and materials science, with countless and groundbreaking possible applications proposed, designed and realized.

Besides this transversal and technologically-oriented impact, the properties of 2DMs were found to be extremely interesting also from a fundamental point of view. The role played by surface science in these investigations has been proven since the beginning to be very crucial. In general these materials in their single layer or few-layers form behave very differently from their bulk counterparts, hence making them the ideal subject of studies employing techniques with high surface sensitivity. Moreover, it has been observed that the properties of 2DMs are deeply affected by the choice of the substate onto which 2DMs are deposited (or directly grown) and by the environment around them. In this respect, photoelectron spectroscopies (PES), both of core levels and of valence band, are an invaluable tool to understand the electronic

structure of 2DMs and the properties related to it.

X-ray photoelectron spectroscopy (XPS), which is often referred as electron spectroscopy for chemical analysis (ESCA), has been identified in general as an essential tool to investigate many aspects of the electronic properties of solids, surfaces and adsorbates by measuring the energy levels of the core electrons [1]. The surface sensitivity and the ability to disentangle differences in the core levels related to the surrounding electronic environment make this technique pivotal in providing accurate knowledge about the factors controlling the chemical composition, structure, oxidation state and reactivity of surfaces and interfaces, thus with a natural extensions to 2DMs. Starting as a technique developed with lab-based compact X-ray sources, the potentialities of XPS have been pushed much further by combining it with synchrotron radiation sources. Such an upgrade has boosted the capability of XPS of investigating element and bonding specificity typical of surface processes, such as diffusion and macroscopic reaction kinetics. These information, which are crucial to elucidate the reaction mechanisms of a broad range of surface reactions, are essential to study and improve the growth and characterization of 2DMs on surfaces. The working principle of photoelectron spectroscopy is simple and relies on the interaction of a photon of given energy $h\nu$ with an atom, causing the emission of an electron in the vacuum with a kinetic energy E_k measured by a suitable electron energy analyzer, characterized by a specific work function φ_A. For solid surfaces, the following relation is valid:

$$BE = h\nu - E_K - \varphi_A \tag{1}$$

with BE being the binding energy of the electron in the solid [2–4]. Although this relation is simple, there are several factors that might affect the final kinetic energy of the outgoing electrons, as already well-documented and described elsewhere [3,5–9]. The BE is essentially the energy difference between the ionic electronic state, i.e. after the electron emission, and the neutral electronic state before the ionization [5]. It is important to stress that the BE is not a one-electron quantity, since it is the difference in the energies of the N electron initial, un-ionized, state and the N-1 electron final, ionized, state [7]. Although a very complicated quantity to be determined, the BE identifies the electronic core level of a specific chemical element. Moreover, the BE is strongly related to the chemical environment, thus depending on the chemical structure of the compound to which the emitting atoms belong. These energy differences in the initial state of the electronic environment result in shifts of the BE of the core levels associated to different chemical composition, hence making XPS capable to selectively identify both the nature of the elements and the type of chemical bond or compound into which these elements take part.

The BE of a core electron in a solid as defined in equation (1) corresponds to the energy required to remove one electron from an atom and to place it at the Fermi energy, e.g. the highest energy at which electrons are found in the valence band. If we call n_c and n_v the number of electrons in the core and in valence, respectively, then we can define

$$BE = E(n_c - 1, n_v + 1) - E(n_c, n_v), \tag{2}$$

where $E(n_c, n_v)$ is the energy of the system in the ground state, and $E(n_c - 1, n_v + 1)$ the one in which one electron has been removed from the core of one atom and placed in the valence band. It is often the case that theoretical calculations based on density functional theory (DFT) do not explicitly include core electrons in the simulations, as the energies involved in typical atomic binding and in chemical reactions are much lower than the binding energies of the core electrons, and so the core wavefunctions are assumed to remain unperturbed from those of the isolated atoms. This approximation is implemented with the introduction of a pseudopotential (PP), which replaces the nucleus of the atom with its core. Within this approximation, total energies are not meaningful, because the core electrons have been taken out from the calculation altogether. They are however irrelevant, as physical quantities only ever depend on energy differences. For the same reason, only

atomic BEs are available, and so their shifts caused by different chemical environments would not be available. The typical solution to this problem then is to build a PP for an atom with a hole in the core, and to calculate $E(n_c - 1, n_v + 1)$ by adding an extra electron in valence [10–12]. Since one only wants to make a single core hole, the calculations are typically performed with a supercell geometry, in which several replicas of the unit cell are included in the simulation, and the hole is made only in one of the atoms of a single replica. For large surface systems, such as those including graphene on a substrate, the number of core binding energies to compute can be several hundreds, one for each non-equivalent carbon in the graphene layer, and so a full core-level shift (CLS) calculation can be about two orders of magnitude more expensive than a single total energy calculation. The calculation of $E(n_c - 1, n_v + 1)$ involves a full relaxation of the valence electrons, which screen the atom with a hole in the core. For this reason, this is usually called a *final state* calculation. DFT CLS usually agree with experiments within 10–20 meV [12–14].

The development of third generation synchrotron-radiation sources has given to the scientific community an outstanding and unique tool to investigate the intricate properties of 2DMs by means of experiments relying on the much higher brilliance of these sources with respect to conventional metallic-anode X-ray sources, on the high energy resolution (down to 20 meV at $h\nu = 200$ eV) and on the possibility to tune the photon energy. These potentialities constitute the primary ingredients to unravel the chemical nature and compositions of many pristine and functionalized 2DMs starting from the analysis of the core level peak spectral line shape. Moreover, the vast knowledge developed by means of synchrotron-based XPS in the last thirty years about the properties of many metallic surfaces and about the interaction of these metals with elementary gases [13,15] provided an excellent starting point to understand and govern the mechanism of growth of 2DMs on surfaces. The capability to follow the process of growth and many other chemical reactions taking place at surfaces is efficiently realized by acquiring spectra by means of fast-XPS (sometimes referred as real-time XPS) [16]. This technique constitutes a very powerful tool that was realized by combining the high brilliance of synchrotron radiation sources with newly-developed electron detectors, thus reducing considerably the acquisition time for the XPS spectra. Furthermore, X-ray photoelectron diffraction (XPD) at synchrotron radiation facilities constitute another powerful spectroscopic tool at scientists' disposal to explore the morphology of materials, in particular those of 2DMs and interfaces, combining structural knowledge with chemical selectivity [17–19]. XPD is indeed an outstanding tool for addressing issues related to the structural and configurational determination of the systems under study but with chemical sensitivity. Therefore, for the many 2D materials that are heteronuclear compounds, XPD diffraction patterns can be measured for a specific element, thus providing a direct characterization of the crystal structure around a well defined emitter. The chemical selectivity of XPD is an unsurpassed characteristic of this technique to get the structure of 2DMs at surfaces and it is unattainable in LEED I(V) or surface X-ray scattering experiments, for which it is not possible to obtain chemically-resolved information.

The progress in creating efficient and very bright synchrotron radiation sources has propelled the development of other two important techniques, namely valence-band angle-resolved photoelectron spectroscopy (ARPES) and near-edge x-ray absorption fine structure (NEXAFS) spectroscopy, which often are combined with XPS at synchrotrons to provide a comprehensive survey the electronic properties of 2DMs. ARPES has a prominent place when coming to delineate the valence band states of 2DMs, providing the momentum-resolved map of the bands. This technique has allowed to strongly expand the knowledge on the electronic properties of 2DMs, by providing insight into the most elusive properties of this class of materials to include them into technological application [20–22]. The combination of ARPES with XPS was crucial to fully depict the wholesome of electronic properties in 2DMs and to link the modifications observed in the core levels with the

features in the valence band, a key aspect of the characterization of 2DMs and of the assessment on them of, e.g., substrate, intercalation or functionalization. Similarly, also NEXAFS was successfully used to provide information about the oxidation state and chemical nature of the bonds in which the 2DMs are involved [23,24]. This whole set of techniques available at synchrotrons has made possible to describe comprehensively most of the properties of 2DMs and has made these facilities one of the forefront of the research about new 2DMs.

The scope that we had in mind when writing this review was not to provide a survey of the entire set of experimental results obtained using surface science techniques on 2DMs, which would constitute quite an arduous task. On the other hand, our intention was to show, with relevant examples, how core-level photoelectron spectroscopy carried out with synchrotron radiation is fundamental for understanding the synthesis and the properties of many 2DMs at surfaces. We believe that this kind of investigations has been extremely helpful in clarifying details that can not be elucidated otherwise, thus contributing significantly to the advancement of the knowledge about this class of materials. We have organized the topics dividing them by class of compounds and, in general, giving an overview on the information obtained about various growth mechanisms and the properties of each 2DM at the different surfaces. Beside this, we will also review some examples of functionalization/modification of the 2DM/substrate interfaces, always putting in the spotlight the contribution given by core-level photoelectron spectroscopy. A large part of this review will be dedicated to recap results obtained on graphene (GR) and hexagonal boron nitride (hBN), which are some of the most studied materials using XPS with synchrotron radiation. In the end, we will review the recent results on transition-metal dichalcogenides and borophene.

The results presented in this work are obtained in general from experiments performed at synchrotron radiation facilities in ultra-high vacuum (UHV) conditions. Most of the works reported herein are focused on experiments on 2DMs grown with well-known bottom-up approaches, such as chemical vapor deposition (CVD), molecular beam epitaxy (MBE) or physical vapor deposition (PVD). We have chosen to report mostly studies carried out in situ, since they are the best way to access directly the pristine property of the 2DM, avoiding, e.g., any contamination connected to air transfer and hence offering precise model systems, for which the properties can be accurately controlled. We will also review some important examples of surface-chemistry reactions which involve 2DMs, that can be described in an accurate and comprehensive manner by using of XPS.

2. Graphene

Graphene has a special place in this review, since, nowadays, it is certainly the most investigated 2DM and it has been extensively studied both from a fundamental point of view and for the potentiality related to technology-oriented applications. This transversal interest is motivated by the outstanding properties of this material, which make it a potential candidate to transform important fields such as electronics, photonics, optoelectronics and catalysis. In addition to that, carbon, the constituent of graphene, is very abundant in nature and at a low cost if compared to many elements and compounds on which technological applications currently rely.

Even before its isolation on silicon oxide wafers by Geim and Novoselov in 2004 [25], graphene was not totally unknown to the surface scientists. Already in the mid 60's of the 20th century, Somorjai and coworkers were trying to unravel the structural morphology of the catalytically-relevant Pt surfaces and they found that the quest for having a clean and reactive transition-metal catalytic surface was often disrupted by the formation of a single layer of graphitic carbon, a feature common to several transition-metal surfaces [26–30]. The carbon layer was appearing on the surface due to C impurities segregating from the transition metal bulk and aggregating on the surface at high temperature in the form of graphitic C. Such film was regarded as highly undesired,

since it impaired the reactivity of the Pt surface.

These results came to a new light when it was realized that the top-down way to obtain graphene proposed by Novoselov and Geim via micro-cleaving (or mechanical exfoliation) was indeed producing samples with a low density of defects and impurities but very hard to reproduce, a feature not desirable for including graphene in industrial processes preferably oriented towards the development of a bottom-up strategy of growth. The full understanding of a process such as the dehydrogenation of a hydrocarbon gas on a transition metal surface, with the subsequent carbon atoms rearrangement into graphene on a metallic reactive surface at high temperature, is the first step to understand the growth of graphene by CVD. This is a prototypical process that can be followed via fast-XPS. In this respect, the knowledge developed and acquired through XPS about the interaction of elementary gases (e. g. oxygen, ethylene, carbon monoxide) with single crystalline metallic surfaces was one of the elements on which to build the understanding of the mechanism of growth and the properties of pristine and functionalized graphene on metals.

2.1. Graphene on metals

In a paper of 1990, A. Tontegode reviewed the conditions of formation and the properties of surface carbon on transition metals (TMs), highlighting its role in physical and chemical processes on the surface [31]. The aim of that study was to identify the condition of formation of the undesired adventitious carbon layer impairing the catalytic properties of the metal, as mentioned earlier. Nevertheless, the information contained in that review were the seed for other investigations on graphene/metal interfaces, since they reviewed many earlier works that discussed extensively the formation of adventitious carbon on metal surfaces [26,27,29,32].

After the seminal work of Novoselov and Geim in 2004, it became evident to the surface science community that graphene could be obtained by CVD on metallic substrates and graphene grown according to this modality became the subject of numerous photoemission experiments, given the facility and reproducibility of this bottom-up approach. The graphene-metal interfaces are considered a pillar of the knowledge about graphene, with a very abundant production of literature covering all the aspects and techniques available in surface science [33–37].

However, the preparation of graphene-metal interfaces, despite seeming a process that can be achieved quite straightforwardly, is on the other hand rather intricate. A crucial element to be considered when talking about these interfaces is certainly the interaction between graphene and the metallic substrate, which can vary radically according to the choice of the TM. This ideally gives the possibility to tailor the electronic properties of graphene, such as doping or opening of a band gap in the electronic band structure, and also to affect the quality and morphological features. Another parameter to be considered is the C solubility in the chosen substrate, which can drive to the formation of multiple graphene layers or favor the growth of other carbon-metal compounds, such as carbides [33,38,39].

Core-level photoemission experiments are very sensitive to all these features as it was efficiently proven in a pioneering work by Preobrajenski et al. [40]. A series of synchrotron-based XPS experiments on graphene grown on different TMs evidenced the spectroscopical differences induced by the chosen substrate and tried to relate the spectroscopical features to the substrate-induced morphological changes in the graphene. In Fig. 1a, the C 1s core level measured for graphene grown on the different substrates is shown. We can observe that the different type of TM substrate dramatically affects the shape and position in BE of the C 1s level, signaling different extent of interaction with the substrate: the interaction is weak, for example, for graphene on Pt (111) and Ir(111), while it is stronger on Rh(111) and Ru(0001). Dahal et al. [41] have shown that the interaction strength between graphene and the metallic substrate can be estimated by observing the position of the C 1s core level and have found a relationship between the doping
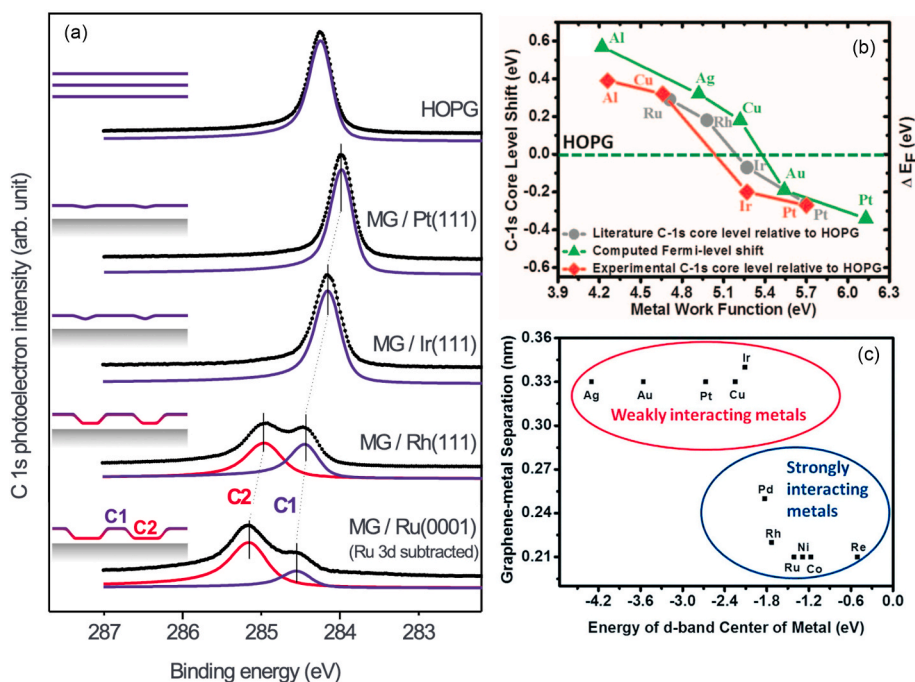
Fig. 1. (a) C 1s core level of single layer graphene on various metal substrates acquired with 400 eV photon energy. For graphene that exhibit a strongly corrugated graphene moiré-pattern two BE peaks are observed, which accounts for C atoms belonging to regions strongly and weakly interacting with the metal within the moiré-unit cell. Reproduced with permission from Ref. [40]. © American Physical Society. (b) Position of the C 1s vs the work function of the metallic substrate. Reproduced from Ref. [41] © 2013 The authors. (c) Ranking of the graphene-metal interaction, showing the graphene-metal separation vs the position in BE of the center of the metal d-band. Reprinted with permission from Ref. [39] © 2014 The Royal Society of Chemistry.

level and the work function of the metal/dielectric onto which graphene is deposited, as shown in Fig. 1b.

Another criterion to estimate the strenght of the graphene-metal interaction relates the latter with the binding energy of the center of the metal substrate d-band, which is usually responsible for major modifications in graphene band-structure. As reported in Fig. 1c, it was shown that a transition from weakly to strongly interacting substrates, signaled by a smaller graphene-metal separation, occurs at a d-band center energy of about 2 eV [39]. According to this criterion, graphene on Ni, Co, Fe, Ru, Rh, Re and Pd belong to a category of metals forming strong chemical bonds with graphene. On the other hand, graphene is weakly bound on Ir, Pt, Cu, Au and Ag. In the following we will review some experiments in which core-level photoelectron spectroscopy was essential to describe and understand the growth of graphene on the aforementioned metallic substrates, underlining the differences due to the various substrates used.

2.1.1. Graphene on weakly interacting metals

As we mentioned earlier, the reactivity of the metallic substrate can be successfully exploited to promote the growth of graphene. If the graphene-metal interaction is weak, this growth is generally not strictly templated by the crystalline symmetry of the substrate, thus often resulting in a GR layer characterized by the presence of crystalline domains with random azimuthal orientation. Nevertheless, highly-ordered GR layers can be obtained by properly tuning the growth conditions, among which the substrate temperature during the growth has a primary role. In this sense, high-resolution XPS with synchrotron light, complemented with techniques such as LEED and STM, has helped to relate growth conditions with the features of the grown GR layer, with a degree of precision unattainable with lab-based XPS setups. In Table 1 we have collected some of the most relevant studies on this class of interfaces.

GR on Pt and Ir interacts weakly. These two interfaces have been studied in details growing GR generally via CVD of a hydrocarbon gas, thus exploiting the catalytic reactivity of these metals. Specifically, GR on Pt(111) can be grown by CVD with a hydrocarbon gas, although growth via segregation of C from the bulk is also possible [42–47]. From a spectroscopical point of view, the C 1s is characterized by a single peak spectrum, centered at BE = 283.97 eV, a value that has been interpreted

Table 1

Overview of the studies on graphene grown on weakly-interacting metallic substrates reported in this review.

Substrate	Features investigated	Refs.
Pt(111)	Growth mechanism, morphology, electronic structure	[42–48]
Ir(111)	Growth mechanism	[49–52]
	Morphology	[53–58]
	Electronic structure	[59–62]
Ir(100)	Morphology, electronic structure	[63]
Ir(110)	Morphology, electronic structure	[64]
Cu(111)	Morphology, electronic structure	[65–67]
Polycrystalline Cu	Morphology, electronic structure	[68–73]

as sign of weak interaction with the Pt substrate [42]. This conclusion was corroborated by microARPES experiments on the single-crystalline graphene domains, which showed an almost intact Dirac cone, except for some residual hole doping due to charge transfer with the substrate [74]. On the other hand, the weak interaction is accountable for the several rotated crystalline domains, which can be detected in STM by the appearance of several moiré patterns [43,48].

GR on Ir(111) constitutes a remarkable example of graphene that can be grown efficiently by CVD using ethylene as a precursor. The observed efficiency of Ir(111) in C–H bond breaking of, e.g., small alcohols [29, 75], makes this surface one of the most active in the process of hydrocarbon dissociation. The formation of graphene on Ir(111) is self-stopping, since it is limited by the amount of bare metallic surface available, given the fact that hydrocarbon dissociation does not take place on GR. Moreover, the low solubility of C in Ir grants the formation of a single-layer of graphene, even if, under certain conditions, C segregation from the bulk and the consequent formation of bilayers have been observed [76]. This interface shows a very distinctive moiré superstructure, well visible in scanning tunneling microscopy and low-energy electron diffraction experiments, which have provided a complete overview of the morphological properties of this important interface [53,55,56,58]. Besides the growth on the Ir(111) surface, also the growth on Ir substrates with different crystalline orientation were investigated [63,64].

The C 1s core level can be fitted with a single component at BE =

284.12 eV, indicating that the graphene is only weakly chemisorbed on Ir(111) [40]. Complementary to that, ARPES showed that the Dirac cone is almost intact and only slightly shifted above the Fermi level due to a substrate induced p-type doping of graphene, that also affects the binding energy of the C 1s core level. Moreover, the moiré superstructure accounts for the opening of mini-gaps in the graphene band structure [59–61].

The temperature at which the adsorption of ethylene in the growth process takes place affects dramatically the features of the final GR lattice. It was shown that with a temperature growth of 1200 K or below the graphene layer exhibits high disorder, while temperatures between 1255 and 1400 K produced randomly oriented domains on the surface. The single domain, aligned along the main crystallographic directions of Ir(111), was obtained only with a temperature above 1500 K [57].

Synchrotron-based XPS acts as an incredibly effective tool to shed light on the mechanism of growth by means of experiments investigating the adsorption and de-hydrogenation of ethylene on this surface at different temperature towards the formation of graphene, which is *per se* a very structured process and has been studied in details [49,50]. As reported in Fig. 2, Tetlow et al. investigated the dissociation of ethylene on Ir(111), combining XPS experiments with DFT calculations [50]. Fig. 2c shows a series of C 1s core level spectra acquired during ethylene exposure at 90 K. At the beginning of the uptake two components at BE = 283.3 eV (a_1) and 283.8 eV (a_2) were observed. Their intensity increases coherently with increasing exposure, keeping a constant intensity ratio and BE difference, indicative of a single adsorbed molecular species with two non-equivalent C atoms and suggesting that the C–C bond is preserved.

This process can be studied efficiently by means of temperature programmed (TP)-XPS experiments, that is fast acquisition of XPS spectra while annealing the sample with a linear thermal ramp. Three different experiments were realized by starting from three different initial ethylene exposures (highlighted in red in Fig. 2a), corresponding to the presence of just the first $a_{1,2}$ spectral doublet (0.05 ML), a mix of the two doublets (0.12 ML) and the saturated surface, before the multilayer growth (0.60 ML). 2D intensity plots of the C 1s (Fig. 2b) acquired during annealing show the chemical evolution occurring at the surface, as evidenced by BE shifts and modifications of the C 1s line shape. Sharp transitions were observed at about 250, 380 and 500 K (high coverage series), while at high temperature (above 800 K) the C 1s spectrum smoothly becomes narrower and moves to a higher BE. Above 900 K, the appearance of a spectral component at a BE of 284.1 eV is observed, which is the fingerprint of the initial nucleation of graphene islands. Combining these results with DFT calculations was instrumental to draw the pathway for ethylene decomposition with eventual formation of carbon monomer species (Fig. 2c). Therefore, hydrogenation, dehydrogenation and C–C bond breaking reactions are required in order to form a graphene layer. Interestingly, the mechanism of formation of graphene on Ir(111) via CVD through dissociation of C_2H_4 was compared to the growth on the same substrate by means of MBE carbon deposition from a graphite evaporator [51]. Analysis of the C 1s acquired during the growth highlighted how the interaction between different C precursors (monomers and dimers) and the growing graphene flakes affects the growth rate of graphene. Moreover, in this case the graphene formation process is not self-stopping, since it does not rely on the reactivity of the bare Ir to promote the graphene growth, leading to the formation of both single-layer and multi-layer GR, thus offering a viable route to grow graphene on a wide variety of substrates.

High-resolution XPS, combined with DFT calculation, allowed the investigation of the morphological features of specific graphene structures on metallic surfaces. For example, this approach was instrumental to reveal the formation of graphene nanoislands on Ir(111) obtained by adsorbing ethylene at a temperature lower than that one employed to form large graphene domains. These nanoislands assume a peculiar
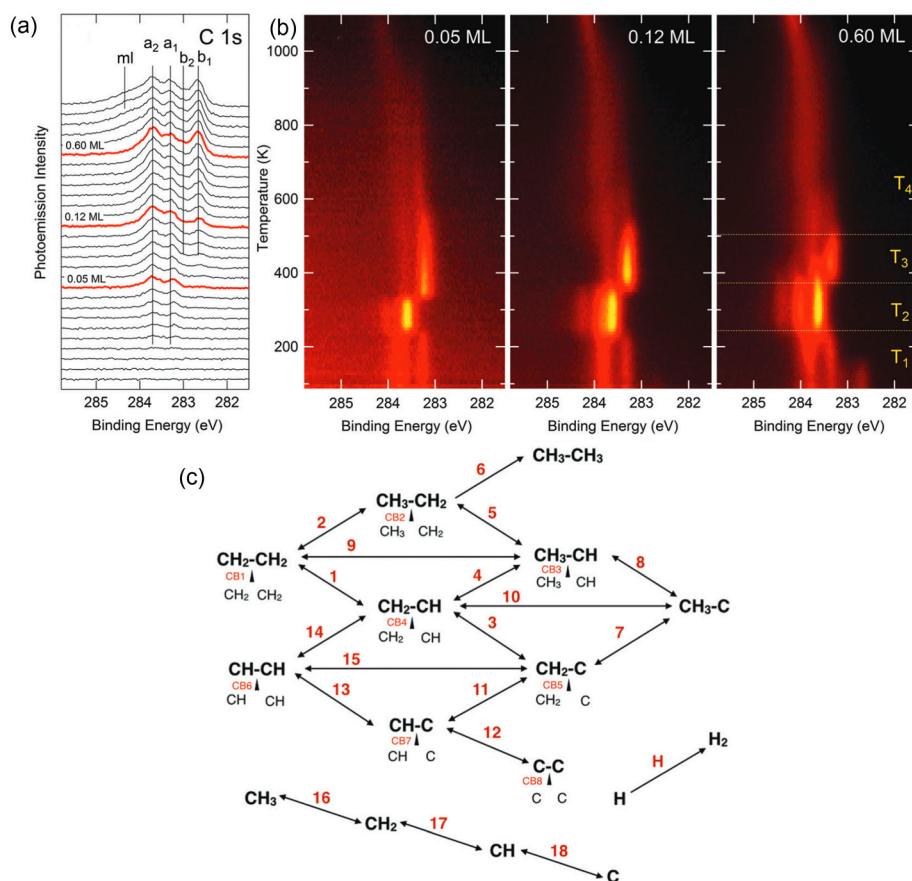

Fig. 2. (a) XPS C 1s spectra acquired during ethylene uptake at 90 K. The three spectra highlighted in red correspond to the three coverages used throughout the experiment. (b) 2D intensity plots corresponding to the TP-XPS C 1s spectral series acquired during the annealing from 90 K to high temperature for the three different ethylene coverages. (c) Proposed pathway for the ethylene decomposition reaction. Reproduced from Ref. [50] with permission from the PCCP Owner Societies. (For interpretation of the references to color in this figure legend, the reader is referred to the Web version of this article.)

domelike shape, whose interaction with the substrate is particularly strong at the edges of the dome [54]. The close correspondence of XPS results and theoretical data suggests that, while growing, the C clusters remain strongly bonded to the substrate only at the edges, as a result of the C 2p hybridization with the first-layer Ir *d* band. Small compact islands with a large number of atoms at the edge and near edge merge to form large islands at 1270 K. These outcomes have paved the way to a better understanding of the interaction with Ir of hydrocarbon and organic molecules and the formation of graphene dots and nanoribbons [52,77–80].

The high structural quality, single-crystalline orientation, lack of azimuthal disorder that can be achieved for GR on Ir(111) together with the weak interaction with the metallic substrate, were exploited in a high-resolution synchrotron-based XPS experiment to extrapolate some very elusive and peculiar features of the graphene lattice. One of the most surprising was the observation of the band dispersion of the C 1s core level, reported by Lizzit et al. [62]. This feature is typical of valence-band electrons but it was never observed for the localized electronic core levels of solids. The authors have argued that the observed modification is due to an initial state effect. The dispersion was observed as an emission-angle modulation of the C 1s binding energy. The picture proposed by the authors to explain this surprising feature relies on the formation of a σ-type band between the 1s states of the C atoms of graphene, as it stems also from tight-binding calculations. An interference effect, already observed in graphite [81] and that is caused by the presence of two atoms in the unit cell of graphene, explains why, under appropriate conditions of electron emission, only the bonding or anti-bonding states can be observed, thus explaining the observed shifts in the C 1s BE.

Graphene can be prepared via CVD on copper, both on single-crystal Cu(111) and Cu(100) [65–67]. The weak interaction between the metal and the graphene in this case is reflected by a weak n-doping of graphene, as clearly seen by ARPES experiments. Concerning the morphological structure of this interface, such weak interaction is responsible for the presence of azimuthally rotated domains with a wide set of possible orientations, which therefore produce a wealth of different moiré superstructures, easily observed in STM experiments [65,67,82]. It is important to mention that graphene can be obtained efficiently on polycrystalline Cu foils [68–73], a process that is extremely relevant in terms of technological applications: graphene grown on polycrystalline Cu can be easily transferred to other substrates by means a polymeric stamp after the dissolution of the metallic substrate [83]. Synchrotron-based XPS was able to shed light on the mechanism of formation of graphene/Cu foil, obtained by exposing the metal kept at 1170 K to benzene. This experiment showed that, due to the low solubility of C in Cu, no species other than graphene were present on the surface, except for some adventitious amorphous carbon [84].

2.1.2. Graphene on strongly interacting metals

The strong interaction between graphene and metal can significantly complicate the process of formation of GR and lead to the formation of unwanted features, such as adventitious chemical compounds on the surface. Such strong interaction acts on the properties of GR layer in a twofold manner. From one point of view, the increased interaction indicates the likelihood to form C-metal compounds on the surface, such as metallic carbides, which are in direct competition with the formation of graphene. On the other hand, a templating effect may take place during the growth, with the possibility to have GR matching the orientation of the substrate. However, this does not exclude the formation of corrugated structures and moiré patterns. Such structural features can be detected through structural techniques such as STM or LEED. However, XPS and XPD with synchrotron radiation have been capable to unravel the finer points and complications of the growth process and linked the spectroscopical features observed in the C 1s spectrum to the morphological features of the GR. Moreover, the possibility of acquisition of XPS spectra at high temperature and in fast-XPS mode was crucial to

understand the mechanism of growth of graphene-metal interfaces for which the metal-carbon phase diagram is generally very rich and depending on the temperature of the substrate. In Table 2 we have summarized the studies investigating this family of interfaces.

The GR/Ni(111) interface constitutes a remarkable and prototypical example of strongly-interacting graphene on metal. From one side, there is an almost perfect matching of the lattice parameters of substrate and overlayer. Moreover, the high solubility of C in Ni and the probability to easily form surface Ni carbides make the formation of multilayer graphene very likely, although in competition with the formation of carbides [39]. Such strong interaction, and the consequent formation of a strong chemical bond, alters considerably the valence band structure of graphene, leading to an almost complete dissolution of the Dirac cone and strong graphene electron doping[85, 94, 96], although other authors have shown through ARPES measurements that the cone remains intact though shifted more than 2.8 eV below the Fermi level [95]. The mechanism of growth of graphene on Ni(111) has been extensively studied by means of synchrotron-based XPS and with microscopy techniques (primarily STM) and it is probably one of the most intricate [85–90]. The growth on Ni is usually obtained through CVD, exposing the metal to a hydrocarbon gas (generally ethylene or propylene), although given the high solubility of C in Ni, segregation from the bulk is also possible. The growth mechanism is very peculiar and it sees competing atomistic mechanisms, since it involves dissolution of C in the metal bulk and Ni carbides formation. Moreover, for this interface it can be observed that graphene assumes on Ni(111) a wide variety of adsorption configurations, a somehow surprising effect given the almost perfect matching of the surface lattice parameters of adsorbate and substrate [90, 97, 98].

Grüneis et al. have explored the dynamics of growth acquiring in real-time the evolution of the C 1s core level, dosing propylene as precursor at various substrate temperatures. They firstly evidenced the influence of the temperature at which the growth takes place, individuating the optimal value to maximize the graphene structural quality, revealing also that formation of adventitious compounds (Ni carbides and/or unreacted or partially reacted propylene) other than graphene takes places on the surface during the growth.

Other experiments (Fig. 3a) dosing ethylene on the surface kept at 790 K, i.e. close to the optimal temperature individuated by Ref. [85], revealed that at the early stages no C is sticking to the metal surface [88]. This can be interpreted as the initial dissolution of C in the top layers of the Ni substrate, eased by the high C solubility in Ni, thus aiming to the fact that before having any surface adsorbate the Ni layers immediately below the surface have to be saturated with carbon. The formation of graphene, signaled by a peak rising at BE = 284.85 eV is preceded by the formation of surface carbides (BE = 283.0 eV) [85], which remain in place also when the graphene layer is complete. Besides

Table 2
Overview of studies on graphene grown on strongly-interacting metals reported in this review.

| Substrate	Features investigated	Refs.
Ni(111)	Growth mechanism	[39,85–91]
	Morphology	[86, 88, 92, 93]]
	Electronic Structure	[85, 90,94–98]
Co(0001)	Growth mechanism	[99, 100]]
	Morphology, electronic structure	[95,100–105]
Fe(110)	Growth mechanism, morphology, electronic structure	[106, 107]]
Re(0001)	Growth mechanism	[108, 109]]
	Morphology, electronic structure	[109, 110]]
Ru (0001)	Growth mechanism	[56,111–113]
	Morphology, electronic structure	[40, 74, 111, 114–122]
Pd(111)	Morphology, electronic structure	[123, 124]]
Rh(111)	Morphology, electronic structure, growth mechanism	[125]
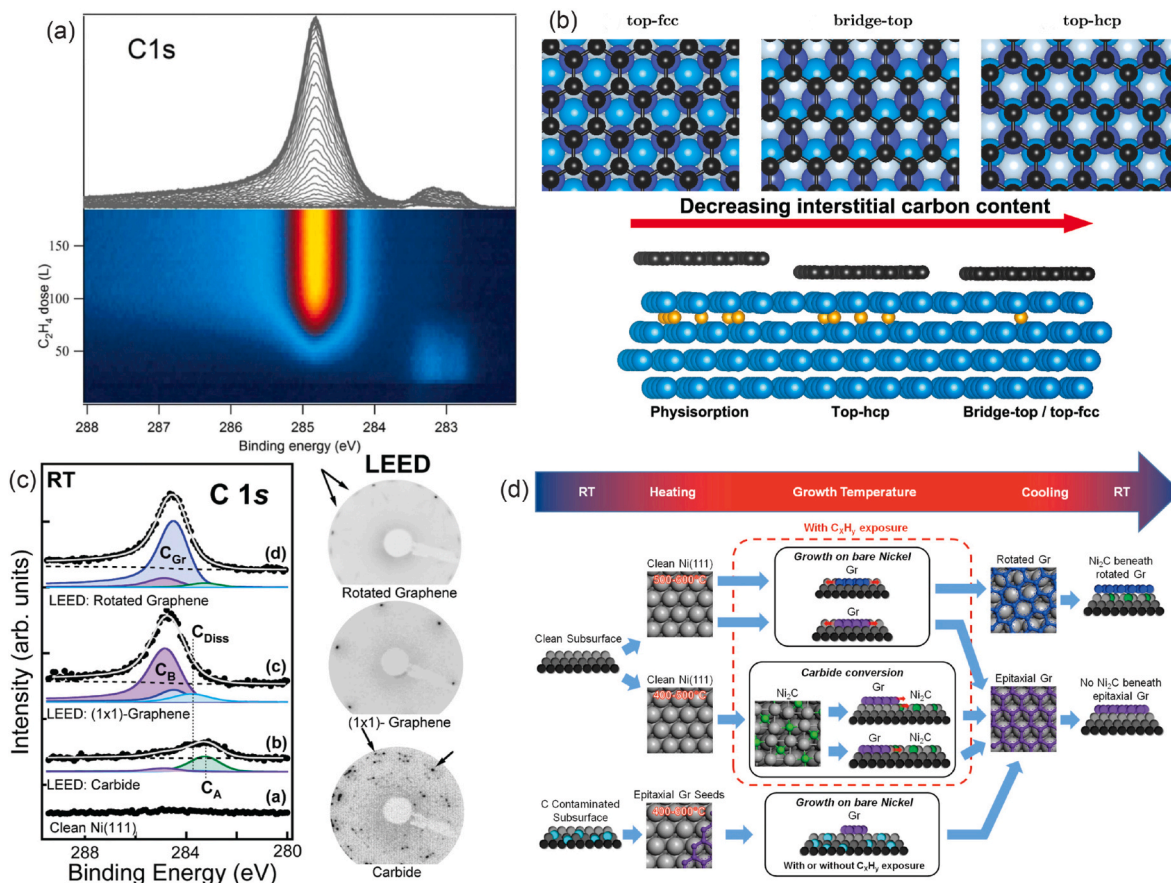
Fig. 3. (a) Growth of GR on Ni(111): 2D intensity plot of the evolution of the C1s signal during the exposure of the Ni(111) surface to ethylene at 790 K. The photon energy is 400 eV. Reprinted with permission from Ref. [88]. © 2016 American Chemical Society. (b) Different adsorption configuration of graphene on Ni(111) vs the content of subsurface interstitial C. Reprinted with permission from Ref. [91], © 2018 American Chemical Society. (c) C 1s XPS spectra (left), and corresponding negative of the LEED patterns (right) of clean Ni(111), carbide, epitaxial graphene, rotated graphene phases. Reprinted with permission from Ref. [86]. © 2013 American Chemical Society. (d) Schematic overview of the different graphene growth routes on Ni(111) from combined high-pressure XPS and STM experiments. Reprinted with permission from Ref. [86]. © 2013 American Chemical Society.

the carbide peak, the C 1s peak associated with graphene has a broader lineshape than for the case of graphene on Ir(111) and can be generally fitted with two components: One more intense at BE = 284.85 eV sided by a shoulder at BE = 284.45 eV, with some debate arising about attribution of these components. In an early report, Zhou et al. performed some high-resolution XPS upon different growth conditions and, corroborated by DFT calculations, they have attributed the high BE component to graphene adsorbed on Ni with a *bridge-top* configuration, while the latter was associated with graphene in a *top-fcc* adsorption configuration [98]. The same research group has later pointed out the impact that interstitial subsurface carbon has on the energetically preferred adsorption geometry of graphene on Ni(111) surfaces:, as shown in Fig. 3b at higher interstitial carbon concentrations chemisorption in *top-hcp* geometry is preferred over the *bridge-top* and *top-fcc* adsorption configuration, which are dominant at small concentrations [91].

Other reports have integrated this knowledge and showed the importance played by the residual surface carbides, which form at the early stages of the growth process, attributing the component at low BE (Fig. 3c) to graphene regions not in contact with bare Ni but supported by Ni_2C surface carbides [86,88,92,93]. These results have been later integrated with LEEM and μ-ARPES experiments, indicating that the graphene on surface carbides has a different band structure and doping level than graphene on bare Ni, thus justifying the lower BE observed for the carbide-intercalated regions [97].

Patera et al. [86] have investigated by means of a combination of

STM and in-situ near-ambient-pressure XPS the growth mechanism at temperatures below 870 K, spotting also in this case the crucial role played by the temperature at which the growth takes place (Fig. 3d). The exposure of the bare Ni to ethylene, keeping the substrate at 770–870 K, leads to the formation of graphene. If the exposure to C_2H_4 takes place in temperature range 670–770 K, there might be the formation of surface carbides which are partially converting into graphene. In these two cases graphene grows both epitaxially aligned to the Ni substrate and with rotated domains supported by residual surface carbides. Interestingly, it was shown that the temperature promotes the migration of the subsurface C, which acts as C feed to form a graphene layer on the surface, irrespective of the presence of the hydrocarbon precursor leading to the formation of epitaxial graphene [33]. An experiment, combining in situ XPS and X-ray diffraction, pointed out a similar mechanism also for the growth on polycrystalline Ni films [126], showing that graphene forms both isothermally exposing the Ni surface to hydrocarbons and by precipitation on cooling of the sample after the hydrocarbon exposure [127]. These spectroscopical measurements were complemented later with STM based experiments [90], which have pointed out the catalytic role played by Ni single metal adatoms during the growth of the graphene layer.

Graphene was grown via CVD on Co(0001) revealing a complex surface chemistry. Depending on the temperature used for the growth, polycrystalline mis-oriented graphene rather than epitaxial graphene can be obtained, with the latter obtained for a growth at a substrate temperature of ca. 750 K [100,101,103,104].

High-resolution spectra of the C 1s are very sensitive to this differences, with the presence of two distinct components C_h and C_t, associated to C atoms in the hollow and top adsorption sites (Fig. 4). On the other hand, in the case of polycrystalline graphene, the C 1s did not show these two-component structure, but just a single, broader peak. Such attribution was supported by energy-dependent photoelectron diffraction, proving a large-scale sublattice asymmetry in graphene on Co(0001). This interpretation was backed by ARPES experiments. Due to the high hybridization of Co 3 d bands and graphene π-state, this interface assumes the character of a spin-polarized interface [102], similarly to what observed for graphene on Ni [96]. This hybrid state has conical dispersion near the Fermi level and it is not observed for the polycrystalline, misoriented graphene.

Usachov et al. proved the possibility to recrystallize the polycrystalline, defect-rich graphene grown at low temperature just by further thermal annealing up to 750 K [100]. Moreover, low-energy electron microscopy (LEEM) and X-ray photoemission electron microscopy (XPEEM) experiments were able to further investigate this conversion process and to point out the underlying mechanism for the formation of epitaxial graphene, finding that this transformation takes place via the growth and propagation of mesoscopic carbides islands [105]. The process of growth on Co(0001), starting from the gaseous precursor, revealed a complicated chemistry by means of fast-XPS combined with STM [99]. Dosing ethylene at 360 K produced an acetylene-saturated surface, which evolved into graphene islands, located on the close-packed terraces without clear preference for step sites, upon heating to 630 K. A dose of ethylene at 630 K was able to create a ca. 0.5 ML atomic carbon-covered surface, which underwent surface reconstruction. The graphene islands formed were found to encapsulate cobalt atoms, with indications of a role played by graphene in restructuring the Co surface. The presence of atomic carbon in the Co surface layers weakens but does not inhibit adsorption of CO and H_2, while, on the other hand the graphene layer covers the surface completely and inhibits adsorption of CO and H_2. This study fostered further investigations that lead to the understanding of the properties of interaction of small hydrocarbon molecules on the catalytically relevant Co surface [104,127,128].

The formation of graphene on Fe surfaces is complicated by a very rich Fe–C phase diagram, which can be accounted for by the high solubility of C in Fe. It was shown that an ordered graphene layer can be achieved on Fe(110), where it creates a periodically corrugated pattern resulting from the substrate-adsorbate lattice mismatch and from strong interfacial C–Fe interaction [106]. The acquisition of C 1s during the annealing of this interface showed that the system is stable up to 900 K, even if prone to a slow C diffusion in the Fe bulk. At temperatures higher than that, irreversible carbides formation was detected, with the most common phases being Fe_3C (cementite) and Fe_7C_3 (Eckström-Adcock carbide) [107].

A crucial reason behind the study through XPS of other graphene-metal interfaces with a strong substrate-adsorbate interaction is related to the considerable configurational modifications induced in graphene by the presence of the metal, with the formation of a moiré pattern and considerable corrugation in the carbon layer. GR on Re (0001), for example, is strongly corrugated, with regions closer to the metallic substrates and others more distant from the metal [109]. Such corrugation, visible immediately in STM images, is affecting as well the shape of the C 1s core level. Miniussi et al. have studied the shape of the C 1s, shown in Fig. 5a, and interpreted it with the support of DFT calculations [110]. By simulating core-level shifts in DFT (bottom of Fig. 5a) they were able to fit the measured C 1s by assuming that graphene on Re(0001) has a consistent buckling of 1.6 Å. The measured C 1s spectrum exhibits two main components, with a separation of ca. 700 meV. The authors have indicated that such a double-peak line shape overshadows the presence of a manifold of components, due to a different degree of interaction of the C atoms of graphene with the metal beneath and cannot be reduced to a simple dual strongly-weakly interacting system. Such observation can be deduced from Fig. 5b, in which the BE of each core-level shift calculated through DFT is reported vs the C–Re distance, a fingerprint of the extent of the GR-Re interaction. The excellent data agreement between the simulated core level and the experimental spectrum proved that the shape of the C 1s spectrum arises from an almost continuous, rather than binary distribution of C–Re distances.

The CVD growth process on Re(0001) was also shown to be very intricated [108]. Specifically, the formation of a long-range ordered graphene layer on Re (0001) without carbon bulk saturation was found to be achievable with the growth parameters, i.e. substrate temperature, hydrocarbon gas pressure and exposure time, properly set in narrow range of values. The analysis of the C 1s core level acquired during the growth allowed the determination of the optimal conditions to achieve ordered graphene. While the low temperature regime was shown to be dominated by the formation of a chemisorbed carbon phase, the authors showed that at high temperature a complex interplay between graphene and surface carbides takes place. Qi et al. have also investigated the same growth process on Re(0001), revealing a novel transition from graphene to metal carbide in the CVD growth process, something
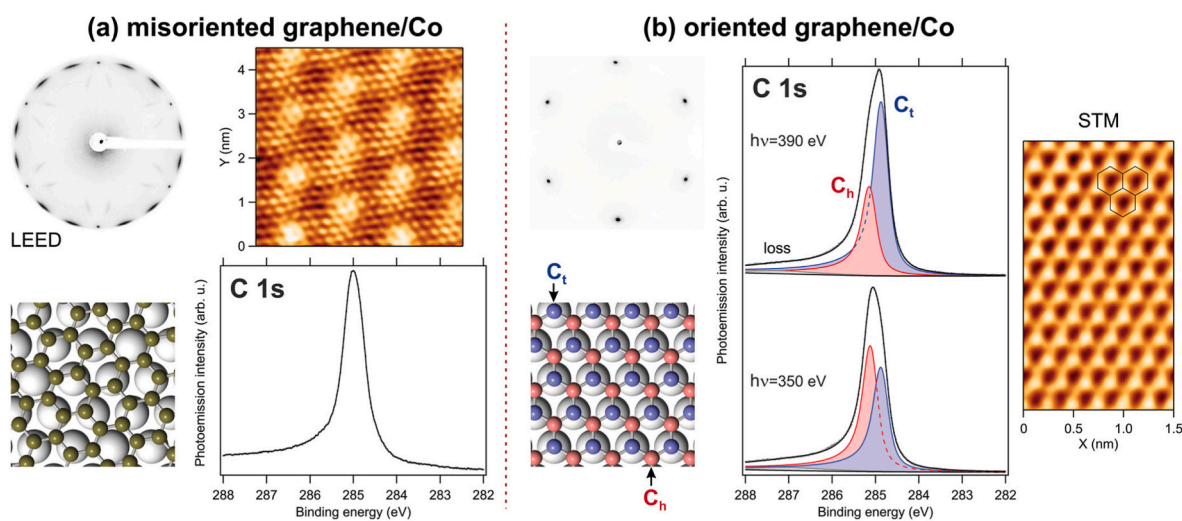

Fig. 4. LEED patterns, crystal structure models, XPS spectra, and STM images of (a) misoriented and (b) oriented graphene on Co(0001). The XPS spectrum of misoriented graphene/Co was acquired using a photon energy of 320 eV. The LEED patterns were obtained with an electron beam energy of 70 eV. The STM images were obtained using a bias voltage of 5 mV at a constant current of 2 nA. Reprinted with permission from Ref. [103]. © 2016 American Chemical Society.
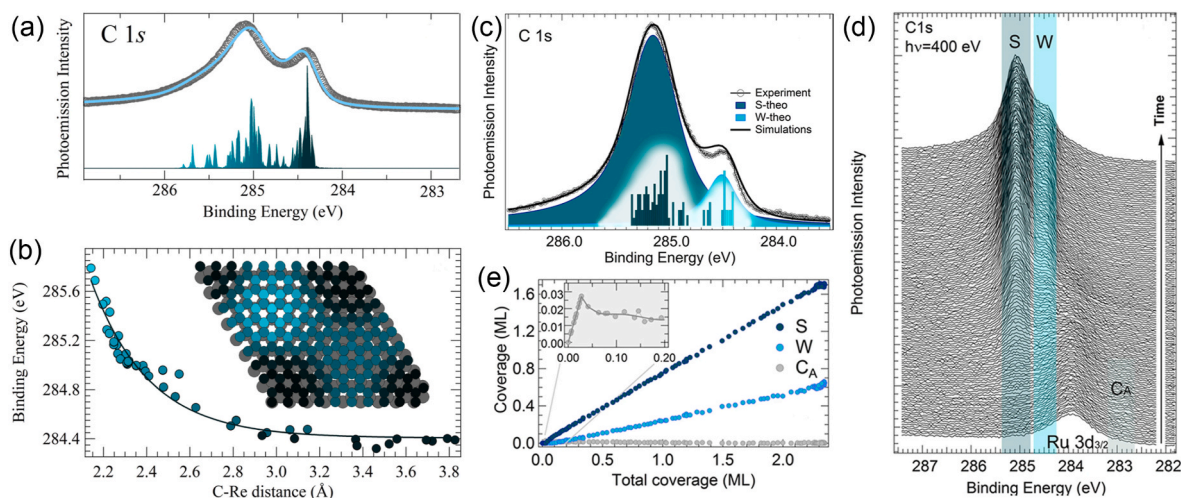
Fig. 5. (a) C 1s core levele measured on GR on Re(0001), with DFT calculated core level shifts from which the fit to the experimental data (light blue line) is generated. (b) BE of the calculated core-level shifts for C 1s reported vs. calculated C–Re distances. The color code identifies the various points the moiré unit cell represented. Reprinted with permission from Ref. [110]. © 2011 by the American Physical Society. (c) C 1s core level measured for GR/Ru(0001), reported with the calculated core-level shifts distribution. The decomposition of the theoretical spectrum into strongly (S-theo) and weakly (W-theo) interacting components is also shown, along with the histogram of the calculated BE distribution. (d) Fast-XPS of the C 1s core level measured during the growth of GR on Ru(0001). (e) Spectral intensity of the various components of the C 1s spectrum during the graphene growth on Ru(0001). Reprinted from Ref. [111]. © 2013 The Authors. (For interpretation of the references to color in this figure legend, the reader is referred to the Web version of this article.)

different from what usually happens for metals such as Ni or Ru. This transition leads to graphene decomposition, dissolution, and carbon segregation [109].

GR on Ru(0001) is one of the most explored and exploited interfaces with strong metal-graphene interaction. On this metallic surface, graphene can be efficiently obtained by decomposition of ethylene keeping the metal at high temperature. Graphene shows a well-defined moiré superstructure, distinctly observed in STM measurements [114] as for GR/Ir(111), together with a remarkable surface corrugation. However, differently from the layer grown on Ir(111), graphene on Ru(0001) is strongly bound to the substrate, as effectively seen in ARPES experiments [40,74,115,117]. Likewise, the strength of the interaction changes the shape of the C 1s core level, similarly to GR/Re(0001) and reflects the strong corrugation of the layer with the appearance of two distinct components, at 284.47 eV and at 285.13 eV (Fig. 5d) [40,110]. The assignment of the observed spectroscopic components to different regions of the corrugated graphene lattice could be achieved by combining high-resolution XPS and DFT calculations and followed the scheme proposed already by Preobrajenski et al. [40]. Alfè et al. showed that the peak at lower BE stems from a continuous distribution of non-equivalent C atomic configurations in the region of the corrugation far apart from the substrate (hills), while that at higher BE is originating similarly from C atoms in closer contact with the substrate (valleys), which consequently brings a stronger interaction with the metal [111]. This interpretation is in line with the outcomes of several STM and LEED I(V) experiments [114,117–122,129] and follows the scheme already adopted for GR on Re(0001). Moreover, Alfè and co-workers, in the aforementioned paper [111], via the analysis of the XPS spectra with the support of calculated core levels, showed a minimum C–Ru distance of 2.15 Å, with a corrugation of 1.5 Å. These values are to be compared with the outcomes of LEED I(V) experiments showing values from a minimum C–Ru distance of 1.5 Å up to a maximum of 2.1 Å [119], while STM investigations by Wang et al. have revealed larger distances (from ca. 2 Å up to ca. 4 Å) [129]. It is interesting to mention that Wang et al. have also observed lateral displacements of C atoms and a significant buckling in the underlying Ru layers, which are the sign of strong local C–Ru interactions. The large electronic corrugation results in a nano-structured periodic landscape of electron and hole pockets [116].

The formation process of this interface was also investigated in

Ref. [111]. By acquiring C 1s during the exposure to C_2H_4 at high temperature, as reported in Fig. 5e) it was observed that, at the beginning, an unidentified C species (C_A) was detected showing up as a small shoulder at BE = 282.82 eV, which was observed before graphene appearing on the surface with its peculiar two-component C 1s core level, as shown in Fig. 5d. It was proven that C_A belongs to C monomers adsorbed at *hcp* sites on the atomic terraces, forming a 2D lattice gas which supplies C atoms for the formation of the graphene layer, as proven by LEEM investigations [56,112,113]. Before this investigation, there was only an indirect confirmation of the presence of monomers on the surface by reflectivity measurements. Zhang et al. [130] have studied the process of formation of GR on Ru as well, investigating the dissociation of ethylene on Ru(0001) at room temperature, which is followed by a full dehydrogenation at 700 K. They observed that higher temperatures promote the diffusion of carbon on Ru terraces and the formation of well-ordered graphene structures.

Other examples of transition metal substrates showing strong interaction with graphene are Pd and Rh. On Pd, graphene can be generally obtained by segregation of C from the substrate crystal bulk and by exposure to ethylene [123,124]. Gotterbarm et al. have successfully grown graphene epitaxially on Rh(111), indicating the importance of propene pressure and surface temperature in achieving graphene with low defect density on this surface [40,125]. In agreement with previous studies on surfaces with similar electronic structures, the authors found that C 1s has two distinct components, indicative of graphene regions exhibiting strong and weak interactions with the Rh substrate.

In conclusion of this section, we believe it is important to remark the importance of XPS performed with synchrotron radiation in depicting the electronic and morphological structure of many graphene/metal interfaces family and in the understanding of the mechanism of growth, in a way that it is not immediately accessible by other surface science techniques.

2.2. Growth on SiC surfaces

As we have seen, a broad part of the studies on graphene at surfaces has been realized using metals as a substrate for the GR growth. However, there are also important examples of graphene directly grown on substrates different from transition metals. Among these, the direct

synthesis on silicon carbide (SiC) surfaces constitutes certainly the most explored case [131,132]. Several experiments using synchrotron-radiation based XPS have deepened the knowledge about the formation and the electronic structure of Gr/SiC, which can be epitaxially grown on several SiC polytypes, such as 4H- or 6H–SiC(0001) [133–136] and SiC(000$\bar{1}$) [137]. Since the formation of graphene on SiC is not achieved by decomposition of a C-containing precursor molecule due to the reactivity of the substrate, it was necessary to develop a different method to epitaxially grow graphene on SiC. The most used one consists in the thermal annealing in vacuum of SiC substrate basal planes, which leads to the graphitization of the surface due to the sublimation of Si atoms [138]. Since the SiC surfaces are usually non-conductive while photoemission requires conductive substrates, GR is generally grown on nitrogen-doped SiC surfaces, in order to prevent any surface charge during XPS experiments.

The C 1s and Si 2p core levels provide considerable information about the configuration of these interfaces before and after the graphene growth. The $(6\sqrt{3} \times 6\sqrt{3})R30°$ reconstruction of the 6H–SiC(0001) surface has been identified as the process through which we can obtain the growth of graphene [135] and it persists at the interface upon the growth of few layer graphene, being often referred to as buffer layer. An example of the modification of the C 1s and Si 2p core level spectra during this process is reported in Fig. 6. The C 1s of the $(6\sqrt{3} \times 6\sqrt{3})R30°$ buffer layer, displayed in panel (a), shows both the SiC bulk component and the S1 and S2 reconstruction-related peaks. After graphene formation by thermal desorption of Si atoms by vacuum annealing [134], the buffer layer is buried below the graphene layers. In comparison with the 0 ML graphene in panel (a), the C 1s peak for monolayer graphene in Fig. 6b can only accurately be fitted after introducing a fourth component (G), which arises from the graphene layer. This component increases in intensity for higher graphene

coverage as shown for bilayer graphene in Fig. 6c. The persistence of the S1 and S2 components even after formation of graphene bilayer indicates that the buffer layer remains chemically unaltered upon graphene formation. Notably, the GR peak shifts towards lower binding energy with increasing number of layers, in good correlation with the shift of the band structure due to the intrinsic n-doping of epitaxial graphene [134,135]. The Si 2p spectrum, measured at 330 eV incident photon energy, shown in Fig. 6d for a GR monolayer, shows the bulk SiC component, the component associated with the SiC reconstruction and a component that was identified as related to surface defects. This proves the lack of any chemical bond between Si and the formed graphene monolayer. This interpretation is confirmed by the acquisition of the Si 2p core level at different graphene coverages, as shown in Fig. 6e, since the Si 2p lineshape does not depend on the coverage. The strong interaction imposed by this interface ensures a very well-ordered epitaxial relationship between the substrate and graphene. On this surface also the growth of different numbers of graphene layers can be achieved and controlled precisely.

On the other hand, on SiC(000$\bar{1}$) the initial graphene layer develops in coexistence with the intrinsic surface reconstructions without the presence of an interface layer [139]. Interestingly, some rotational disorder in graphene is observed on this surface, indicating a weak coupling with the substrate.

2.3. Intercalation

This very rich landscape of graphene-based interfaces has stimulated several studies that aimed at finding reliable and reproducible approaches to precisely modify and control the properties of GR at surfaces. These strategies are based on putting the graphene layer in contact with atoms, molecules, thin films capable of altering its electronic
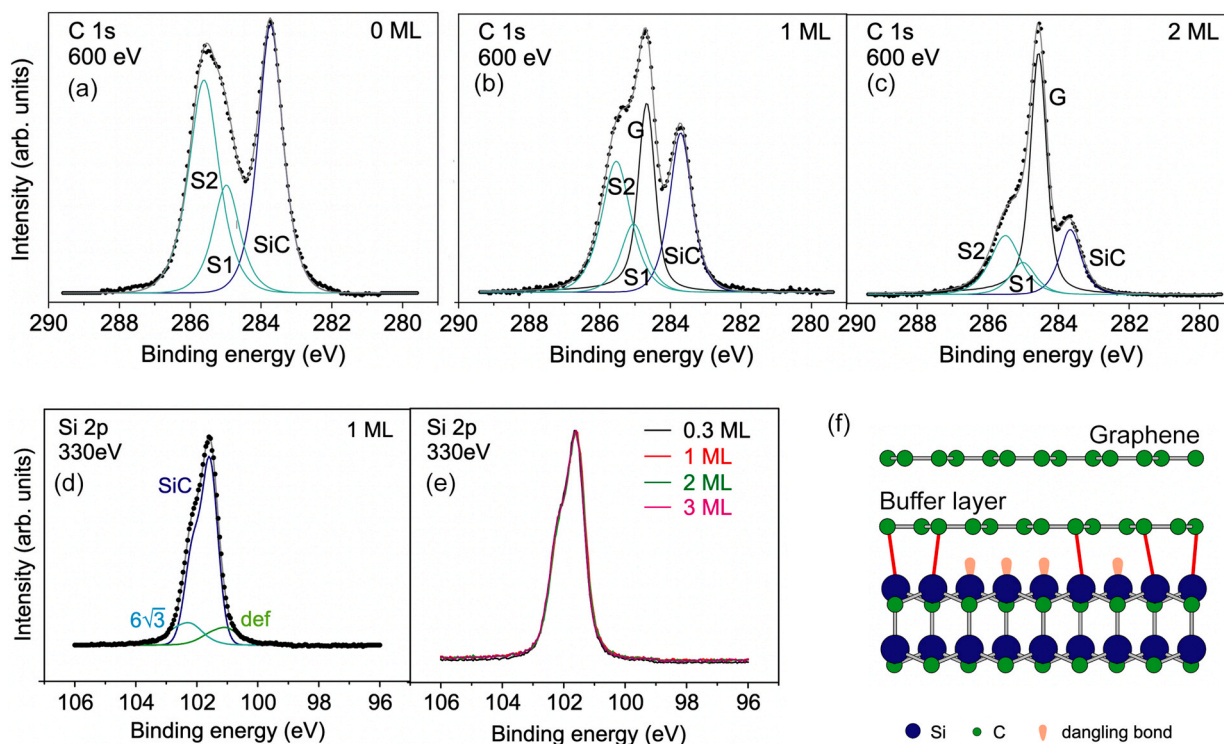
Fig. 6. C 1s spectrum for (a) $(6\sqrt{3} \times 6\sqrt{3})R30°$ SiC(0001) reconstructed surface and for (b) mono- and (c) bilayer epitaxial graphene together with their deconvolution into bulk (SiC), graphene (G) and $(6\sqrt{3} \times 6\sqrt{3})R30°$ reconstruction (S1 and S2) related components. The photon energy is 600 eV. (d) Si 2p spectra for monolayer epitaxial graphene together with the deconvolution into bulk (SiC), $(6\sqrt{3} \times 6\sqrt{3})R30°$ reconstruction $6\sqrt{3}$ and defect (def) related components. The incident photon energy is 330 eV. (e) Si 2p spectra for different graphene coverages (normalized). Structural model of (f) monolayer epitaxial graphene on SiC(0001) in side view. The graphene is growing on top of the $(6\sqrt{3} \times 6\sqrt{3})R30°$ reconstructed interface layer (buffer layer). Reprinted with permission from Ref. [134]. © 2010, IOP Publishing Ltd.

structure and/or the electronic structure of the interface of which graphene is part.

An extremely powerful way to modify in a controlled and homogeneous way the electronic and structural properties of graphene is by intercalation, which can lead to the functionalization of the graphene layer [140,141]. Intercalation consists in inserting atoms or molecules between graphene and the supporting substrate, thus bringing significant alteration to the interface electronic and structural properties. Such operation may lead ultimately to the electronic decoupling of the graphene from its substrate and the consequent alteration of its band structure. The efficiency of this process is strongly correlated to the nature of the graphene-metal interface and the conditions needed to maximize the efficiency of this process depend on a number of factors, such as the temperature at which the process takes place, the flux of intercalating species arriving on the substrate and the extent of the graphene-substrate interaction. Furthermore, one has to consider the role played by defects and domain boundaries in the graphene lattice, which are often the gateway through which the intercalation takes place. In the following, some relevant examples that show how XPS is crucial in fully understanding the intercalation mechanism will be presented. XPS has the advantage, with respect to other techniques, of directly accessing to the type of the chemical bonds formed during the intercalation process. Such feature, often combined with ARPES measurements of the valence band, has provided a comprehensive view of the mechanism of intercalation and on the newly-formed interface. Moreover, photoelectron spectroscopy gives access to electronic and structural features of the on-top graphene layer but also to what lies underneath, revealing for example the oxidation state or the chemical nature of the bonds formed by the intercalated species, a series of information which is extremely hard to obtain with other techniques. Furthermore, with XPS it is possible to understand whether the intercalation process is complete or if there are remains on the graphene surface and/or intercalating species reacts with the graphene layer itself.

2.3.1. Intercalation with metallic atoms

Deposition of metallic atoms on graphene is one of the mostly explored strategies to modify the properties of graphene and often was proven to achieve the intercalation of the deposited metallic atoms between graphene and substrate. A wide set of metals has been used as intercalating species for graphene, a list of which is reported in Table 3. Such wealth of possibilities has lead to countless different interfacial configurations, each one with peculiar properties given by the combination of graphene, intercalating species and substrate. The modification of the surface potential of the graphene via intercalation has shown important implications in favoring the formation of molecular self-assembled lattices on the surface, whose arrangement is closely related to the nature of the intercalating material [142–148]. In addition to that, the intercalation of selected species under graphene opened to the possibility of performing chemical reactions in the confined space between graphene and substrate [149].

Table 3
Metallic species employed for graphene intercalation, described in this review.

Intercalating metal	Refs.
Au	[42–48, 74]]
Cr	[150]
Co	[142,151–153]
Ru	[153]
Fe	[106,154–158]
Ag	[159]
Rh	[153]
Cu	[160]
Ir	[153]
Pb	[161–163]
Alkali Metals	[164–168]
Rare Earths	[168–173]

A very direct way to asses the modifications induced by intercalation in the electronic structure is certainly through ARPES. However, the acquisition of core levels can return important information about the intercalation process, the nature of the intercalating layer and the modifications induced in graphene. As an example, we mention the process of intercalation of metals at the weakly-interacting graphene on Ir(111). Presel et al. [153] have shown that the intercalation of GR with Ru, Rh and Co atoms can alter considerably the shape of the C 1s core level with respect to the pristine graphene. They observed a significant increase in the graphene-substrate interaction when intercalating Rh, Ru and finally Co, which has, on average, the strongest interaction with graphene among the systems studied. Combining this analysis with theoretical modeling of the C 1s core-level by DFT, the authors verified that the C 1s spectral barycentre has a linear relationship with the d-band center position, a further confirmation of the strong influence of the coupling between graphene and the metal surface. The acquisition of several spectra taken at the various stages of the intercalation shed light on the mechanism of intercalation itself for the different intercalating species.

For Gr/Ni(111), the quenching of the hybridization of 3 d Ni bands and graphene π states was realized through the intercalation of an apt species. In many cases, this operation was shown to lead to the formation of a quasi-free standing graphene layer. This was observed by intercalating for example Au [85,94], Al [174], Fe [175] and Cs [176]. For intercalation of Au, ARPES data have shown clearly the Dirac cone at the K point of graphene Brillouin zone, a clear sign that the hybridization with the Ni 3 d bands was lifted [94]. Similar effects have been also observed for intercalation of Au on GR/Ru(0001) [177].

As already mentioned earlier, the formation of a chemically-different layer at the metal-graphene interface can alter the properties of graphene. Such trend was confirmed by alloying the intercalated species with the first atomic layers of the substrate, with important repercussions on the control of the doping level of graphene [111, 178–182].

Vilkov et al. [178] have exploited this strategy to grow graphene-capped silicides that are reliably protected against oxidation and can cover a wide range of electronic materials/device applications. Synchrotron-based XPS was essential in determining the stoichiometry of the silicides layers produced at different stages of a temperature-promoted gradual intercalation of Si under graphene on Ni (111) (Fig. 7a). The deconvolution of the Si spectra evidenced two components likely reflecting electron emission from Si atoms residing at the surface and in the bulk of the silicide layer. These data combined with the well-known phase diagrams for the Ni–Si system indicated that the different stages of intercalation have altered the stoichiometry of the silicide layer going from the Ni-rich phase Ni_3Si to NiSi.

Brede et al. [179] have shown the evolution of the core levels during the process of formation of a FeIr alloy supporting graphene. Starting from an intercalated Fe layer between the graphene and Ir(111) surface, they showed that it was possible to fine-tune the graphene-substrate interaction by Fe–Ir alloying at the interface. When a critical Ir-concentration close to 0.25 ML was reached in the Fe layer, the Dirac cone of graphene was largely restored and could thereafter be tuned across the Fermi level by further increasing the Ir content. In this case the acquisition of the Ir 4f and Fe 2p core level was essential in determining the degree of alloying of the metallic layer interfacing graphene. (Fig. 7b).

2.3.2. Other intercalation strategies

Besides metals, the intercalation of simple molecules was certainly one of the most explored, with O_2 [93,183–192], CO [193–195], and H_2 [196,197] being among the most employed. The intercalation of molecular oxygen was one of the most successfully achieved on graphene-covered metal surfaces. It was proven that, despite the passivation effect of graphene with respect to the bare surface [69], intercalation is possible upon an apt choice of O_2 partial pressure and
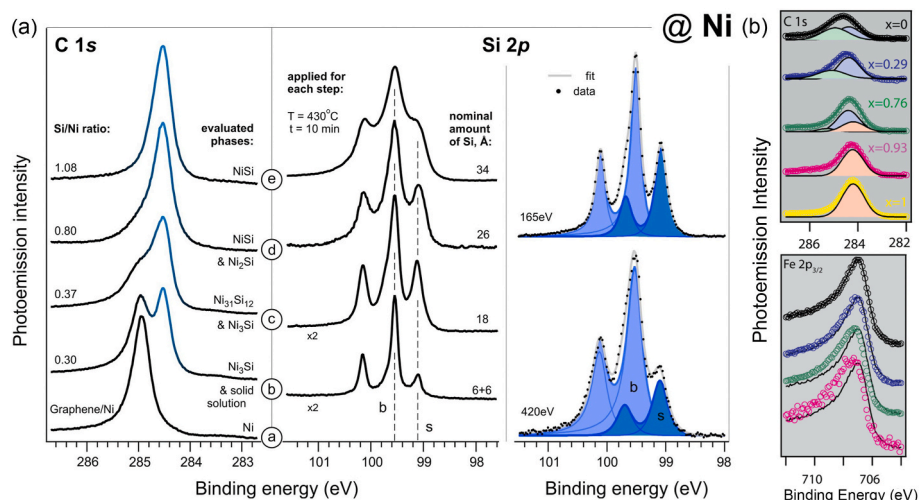
Fig. 7. (a) Left panel: C 1s and Si 2p acquired at different stages of the gradual Si intercalation promoted by thermal annealing at 700 K. Right panel: Deconvolution of the Si 2p spectra taken at 165 eV and 420 eV to individuate the bulk (b) and surface (s) component of the silicide layer. Reprinted by permission from Ref. [178]. © 2016. (b) C 1 and Fe 2p core level measured at different extents of the Fe–Ir alloying. Reprinted with permission from Ref. [179] © IOP Publishing Ltd.

substrate temperature, regardless the extent of the graphene-metal interaction. Mapping the modifications of the core-levels helped to clarify, as much as it happens for intercalation of metals, the stages of the intercalation and the modifications induced at the graphene-metal interface, which can range from the formation of quasi-freestanding graphene to the formation of an oxide layer.

The intercalation of molecular oxygen was successfully obtained on graphene on Ir(111), leading to the decoupling of graphene from the substrate [184,185,198]. Such process can be followed in details again by acquiring the C 1s core level for different oxygen exposures [184]. Oxygen intercalation originates a shift of the C 1s core level towards lower BE which is ca. −0.6 eV when the Ir surface is saturated with oxygen. A slightly sharper C 1s peak is observed for the intercalated

system, which is a further indication of the change of the GR-substrate interaction. Moreover oxygen-induced p-doping of the graphene layer and lifting of the moiré superstructure and the moiré-induced mini-gaps are evident from ARPES measurements of the band structure and STM inspection after the intercalation took place [185,198].

The temperature of the substrate was found to have a primary role in this process, promoting the efficiency of intercalation. Larciprete et al. [184] have shown that upon annealing oxygen de-intercalation takes place leading to the landing of graphene back on the Ir surface. Oxygen intercalation is then a reversible process. However, repeated intercalation/de-intercalation cycles cause damage of the graphene up to a level that it can be lifted from the Ir(111) surface already at room temperature and moderate O_2 pressure. In Fig. 8b it is possible to
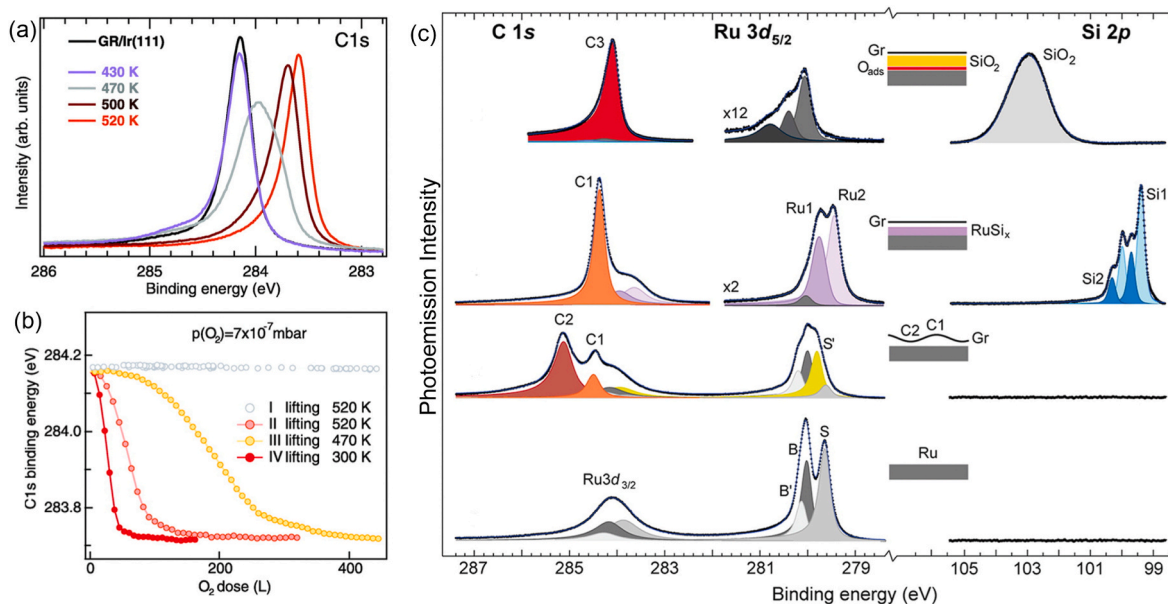

Fig. 8. (a) XP-spectra of the C 1s region of graphene/Ir(111). spectra for different intercalation steps of oxygen under graphene/Ir(111). Oxygen was dosed 5×10^{-3} mbar for 10 min and at a sample temperature ranging from 430 to 520 K. (b) C 1s binding energy measured during oxygen exposure at 5×10^{-3} mbar and different sample temperatures on the as-grown graphene/Ir(111) (I lifting) and for graphene/Ir(111) defected through previous intercalation/deintercalation cycles (II, III, and IV lifting). Reproduced with permission from Ref. [184] © 2012 American Chemical Society. (c) C 1s, Ru $3d_{5/2}$ and Si 2p core levels acquired at different stages of silicon and oxygen intercalation under graphene on Ru(0001) to form a thin SiO_2 layer. Intercalation of Si generated Ru silicide, which was converted into a SiO_2 layer by the intercalation of oxygen. Reproduced with permission from Ref. [199] © 2012 American Chemical Society. (For interpretation of the references to color in this figure legend, the reader is referred to the Web version of this article.)

observe that, whilst the pristine, as-grown graphene layer is not inter-calated by moderate O_2 pressure ($p = 7 \times 10^{-7}$ mbar), the process is instead happening with a much lower O_2 dose. Further attempts show that the intercalation takes place also at lower temperature, conversely to what observed for the as-grown graphene layer [184]. With further intercalation-deintercalation cycles the complete etching of the graphene layer can be achieved, in pursue of a quantitative estimate for the activation energy of the O-induced etching [200]. In a similar way, it was possible to achieve reversible intercalation of oxygen under graphene grown on the more strongly-interacting Ru(0001) surface, restoring its nearly free-standing character and removing the structural corrugation [121,186,187,191].

Intercalation of oxygen at the graphene-Ni(111) interface interest-ingly lead to the formation of an antiferromagnetic NiO layer at the interface between graphene and the ferromagnetic Ni, with the gra-phene fully decoupled from Ni and strongly p-doped [93,190]. Despite the formation of this NiO layer, the intercalation was proven to be fully reversible with no damage of the graphene layer upon annealing for oxygen de-intercalation. It was interestingly observed that graphene domains which are not fully aligned with the orientation of the Ni un-derneath are the first to be intercalated and act as gate through which the intercalation of the full layer takes place. In these regions, oxygen diffuses under graphene and then dissociates on the Ni surface, forming initially a (2×2) adsorption structure, which is followed by the growth of a thin layer of Ni oxide at higher oxygen exposure [93].

Intercalation of different species offers a way to the formation of more complex interfaces. The formation of thin oxide layers, for exam-ples, constitutes an important step towards the possibility to employ graphene in electronic and spintronic applications [201] and as an essential element in building new architectures for more efficient cata-lysts [202]. The formation of a thin SiO_2 layer was successfully achieved intercalating subsequently Si and O at the graphene-Ru(0001) interface [199,203]. It was found that Si atoms intercalated at 720 K below the graphene and formed a silicide with the metal substrate. Such layer was later oxidized by exposing the sample to oxygen to form a SiO_2 layer supporting and decoupling graphene from the metallic substrate. The different phases of this process were followed by recording XPS spectra at each stage of the process (Fig. 7b). The experiments revealed the chemical nature of the intercalated layer and the removal of the moiré corrugation and the efficient electronic decoupling of GR from the metal substrate.

Together with SiO_2, alumina (Al_2O_3) is another relevant material from the technological point of view, since it is often included as high-k oxide in transistors and low-power chips. Omiciuolo et al. [189] have individuated through the study of the C 1s during intercalation a straightforward and efficient way to prepare graphene supported by an alumina layer (Al_2O_3). Starting from epitaxial growth of graphene by CVD of ethylene on the (111) surface of the bimetallic Ni_3Al alloy sur-face, they were subsequently able to form a 1.5 nm thick alumina nanosheet below graphene by intercalation of molecular oxygen while keeping the substrate at 520 K. An interesting feature of the system is that the thickness of the oxide layer is comparable to the values used in spin transport devices. Finally, the authors have shown that other oxide layers could be deposited on top of the GR–oxide interface, leading to the possibility of building oxide–GR–oxide sandwiched heterostructures.

Other examples of the formation of oxide layers between graphene and the metal substrate through intercalation were achieved at the GR/Ir(111) interface, realizing Fe and Ti oxide below graphene [155,204, 205]. In both these cases, the acquisition of the core levels at each stage of the formation of the nanoarchitecture was employed to monitor and to understand the evolution of the intercalation process and the for-mation of the oxides. De Angelis et al. [205] have shown how to prepare a GR/TiOx nanoarchitecture, with a layer of $TiO_{1.5}$ intercalated below graphene on Ir(111) and titania nanoparticles deposited on top of it. Ti oxide constitutes one of the most important materials studied in the last

thirty years because of its catalytic properties [206]. Moreover, such combination has attracted considerable interest, since graphene and Ti oxide may constitute two capital ingredients of newly-designed mate-rials with important implications for catalysis and photovoltaics [207, 208]. In the aforementioned paper, De Angelis et al. have shown that the position in BE of the C 1s core level acquired at each stage of the for-mation of the heterostructure, together with the measurement of the work function of the sample, were crucial to assess the charge transfer from graphene towards the substrate and the supported particles. This information was essential to understand and explain the enhanced photocatalytic activity of this heterostructure towards the hydrogen evolution reaction, motivated by different doping level induced in gra-phene by the $TiO_{1.5}$ intercalated oxide layer and by the shifts of the Ti *d*-band of the titania NPs on graphene. It is worth mentioning also the possibility to form oxide thin films directly on graphene, an essential step in realizing device-oriented architectures [181,209].

Hydrogen intercalation has a particular importance in the case of epitaxial graphene on SiC surfaces. In particular, it is possible to inter-calate the first surface layer of the $(6\sqrt{3} \times 6\sqrt{3})R30°$ SiC(0001) recon-struction (i.e. the "buffer layer"). The topmost Si atoms, which for epitaxial graphene are covalently bound to this buffer layer, are indeed saturated by hydrogen turning the buffer layer into a quasi-free-standing graphene monolayer [196,197]. A uniform and homogeneous intercal-ation can be achieved. This can be immediately spotted in C 1s core level acquired on H-intercalated regions of the sample, with the appearance of a single component spectrum, which is assigned to quasi-freestanding graphene, an outcome corroborated also by ARPES measurements showing the typical linear π bands [134,196]. Remark-ably, this intercalation is fully reversible upon thermal annealing. Fig. 9c shows the C 1s evolution during such a process, going from the inter-calated graphene (bottom spectrum) to a sample annealed up to 1060 °C (top spectrum) that shows a full recovery of the spectral features typical of the buffer layer, thus implying a full de-intercalation of Si-bound hydrogen.

2.4. Functionalization and chemical doping

The substantial knowledge developed about the intercalation mechanism of several species below graphene has supported the assumption that, by a proper choice of substrate, one can considerably alter the properties of the graphene layer, thus fostering the attempt to functionalize the normally rather inert graphene layer. In this respect, doping graphene by contacting it with another chemical element can be considered as the simplest form of functionalization. Such observation is central, for example, when doping of graphene with metal contacts to realize a device. The choice of the dopant element can alter, even only locally, the electronic structure of graphene, an information essential to design and build devices that integrate a graphene layer [210–212]. These early observations opened the way to a new series of experiments with the declared aim to find a strategy to chemically alter the electronic properties of graphene by functionalization, rather than relying on the modification induced by a substrate or by an intercalating layer. In this respect, XPS, given the chemical sensitivity, constitutes a prime-choice tool to individuate and understand the chemical modifications pro-duced in the graphene layer and the modification to the stoichiometry produced by any external functionalizing agents.

In a review dedicated specifically to this subject, Grüneis [213] has categorized three different types of graphene functionalization, which can take place via: 1. ionic and 2. covalent functionalization by adatoms or 3. by substitutional functionalization. In the case of ionic function-alization, the host atom donates or accepts charge without sharing this charge with the graphene, i.e. the charge is fully transferred from host to graphene. The donated charge then becomes delocalized over the whole graphene layer. The functionalizing atom is usually located on top of the C hexagon. An excellent example of this mechanism is the deposition of
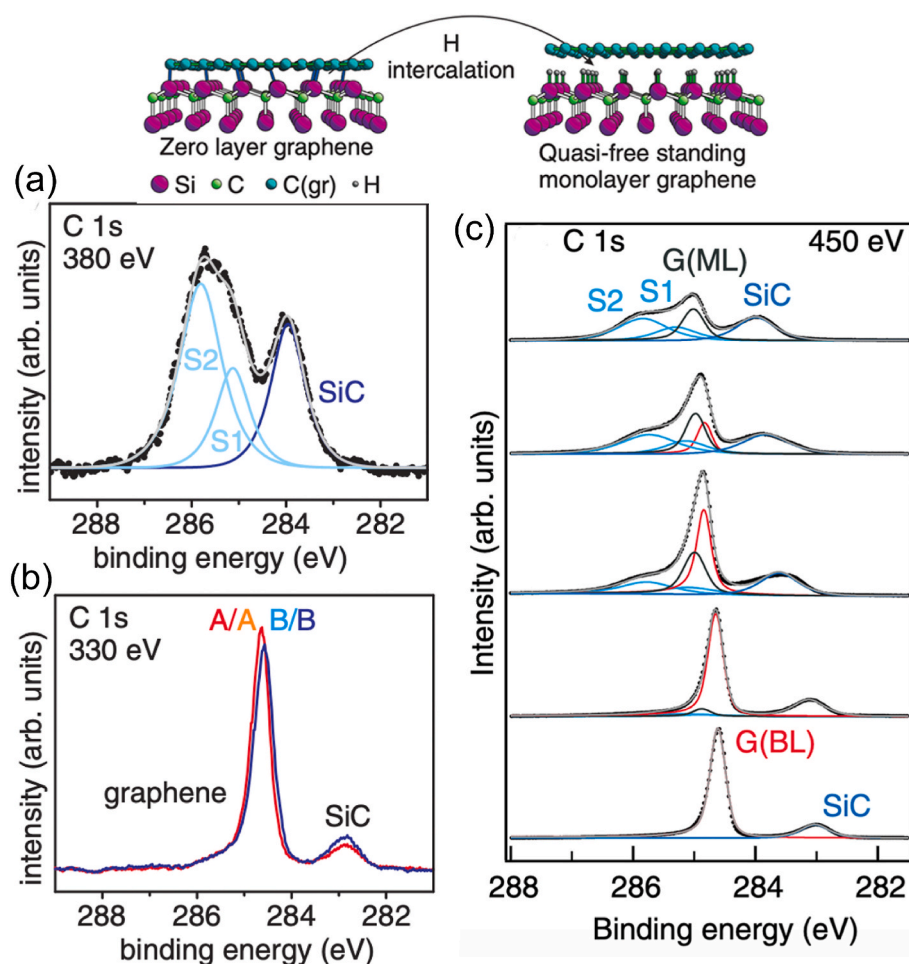
Fig. 9. C 1s core level for (a) the $(6\sqrt{3} \times 6\sqrt{3})R30°$ reconstruction ("buffer layer") and (b) of a fully H-intercalated quasi-freestanding graphene layer. Top scheme: mechanism of H intercalation. Reprinted figures with permission from Ref. [197] © 2011 American Physical Society. (c) C 1s core level spectra for a hydrogen-treated monolayer graphene sample (bottom spectra) and the same sample annealed at increasing temperatures. Reprinted with permission from Ref. [196]. © 2009 by the American Physical Society.

alkali-metals and rare-earths, whose effects are especially visible in ARPES measurements, with significative alteration of the band structure in terms of positioning of the Fermi level [164,166–168,213,214]. Such shifts in the Fermi level are expected to cause also a shift in the position in BE of the C 1s core level [41,210]. It has been showed that the relationship between Fermi level and C 1s peak position holds as long as the Fermi-level shift is smaller than 0.5 eV [168,204]. In this regime, it is thus possible to estimate the effects of the functionalization in terms of doping by monitoring the evolution of C 1s.

Covalent functionalization leads to significant alterations of the C 1s core level, indicating a change in the chemical structure of the carbon layer. In this case the functionalizing species is generally located on top of a carbon atom or on top of a C–C bond and shares an electron with the nearby atom or atoms, thus producing a distortion of the graphene lattice. Functionalization with H and O are belonging to this category, and both cases are particularly relevant. The addition of these simple atomic species has been shown to change the electronic band structure of graphene from that of a semi-metal to that of a semi-conductor or insulator [215–217]. Substitutional functionalization can be seen as a specific example of covalent functionalization and it takes place whit the replacement of a C atom by a chemically similar atom such as B or N. Different configurations, and different reactivity properties, can be obtained according to the site in which the substitution takes place, with important implications in the reactivity properties of graphene and in the design of graphene-based single-atom catalysts [218–220].

2.4.1. Hydrogen functionalization

Functionalization with hydrogen has been investigated in depth from different points of view and it can lead to the formation of graphane, i.e.

a fully-hydrogenated graphene layer. The importance behind this process resides in the fact that it was theoretically predicted to be one of the easiest ways to open a band gap in graphene band structure [222], as later verified experimentally both for graphene on metals [223] and SiC [224,225]. However, XPS experiments have revealed that hydrogenation of graphene on metallic surfaces is a complex process with different steps leading to the graphane formation. A remarkable example is the hydrogenation of graphene on the weakly-interacting Ir(111) surface. On this substrate, as much as on the weakly-interacting Pt(111), hydrogen atoms adsorb preferentially on carbon atoms in the valleys of the corrugated moiré structure, forming a so-called graphane-like structure [216,221,226,227].

The acquisition of XPS spectra during the different phases of hydrogenation, which is generally obtained by sending a flux of atomic hydrogen towards the sample in UHV, have showed the presence of two types of hydrogen adsorbate structures at the graphene/Ir(111) interface, namely, graphane-like islands and hydrogen dimer structures, as shown by Balog et al. [221] and reported in Fig. 10. This process was also proved to be highly-dependent on the substrate temperature during the hydrogen exposure. Keeping the sample at 300 K during the exposure to atomic H lead to the formation of hydrogenated regions coexisting with H dimer structures. Annealing at 630 K was enough to remove dimer structures from the surface, whilst for temperatures above 645 K hydrogen adsorbs exclusively on the hcp regions of the graphene/Ir(111) moiré structure [221]. ARPES and STM measurements proved the preferential functionalization of just one region of the moiré supercell and showed that this results in the opening of a band gap in the band structure at the K-point of the Brillouin zone of graphene [223], whereas with very limited associated broadening of the graphene π band
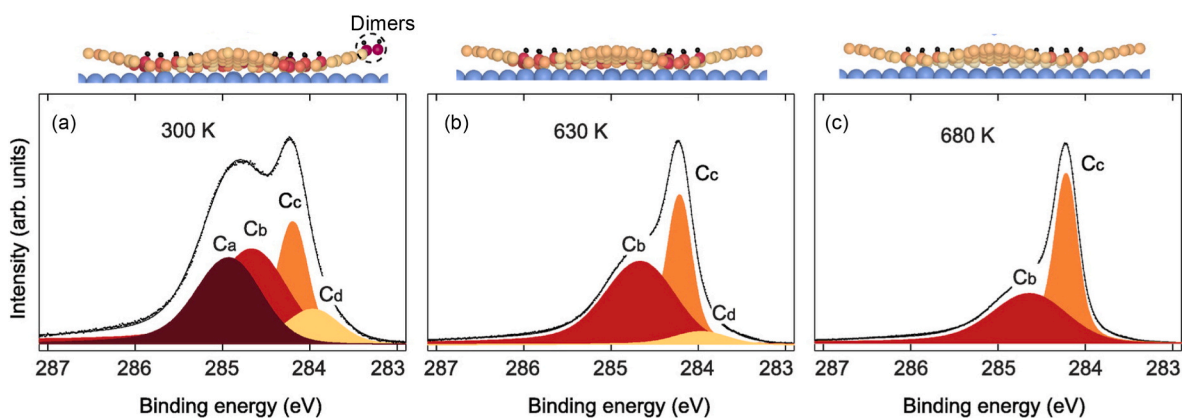
Fig. 10. Fitted C 1s core level spectra for hydrogen-saturated graphene at 300 K. Two main hydrogen structures are observed, namely, dimers –detected by the presence of the Ca component– and graphane-like clusters detected by the presence of Cb and Cd components. (b) Hydrogen-saturated graphene after annealing to 630 K. Dimer structures have been removed from the surface, leaving vacant graphane-like clusters on fcc and hcp areas. (c) After annealing hydrogenated graphene to 680 K, graphane-like clusters become smaller in size as seen by the disappearance of the Cd component and the reduction of the Cb component. Reprinted with permission from Ref. [221]. © 2013 American Chemical Society.

[216]. Thus, hydrogenation at elevated sample temperatures provides a pathway to efficient band gap engineering in graphene via the selective functionalization of specific regions of the moiré structure. The adsorption of hydrogen was proven to be a fully-reversible process, since a thermal annealing up to 720 K was enough to restore the original graphene layer. Balog et al. discussed in Ref. [221] also the stability of these graphane-like clusters depending on the position they occupy in the moiré superlattice of GR/Ir(111). These observations were pivotal to propose the possibility to pattern the graphene layer with a precise amount of hydrogen.

Interestingly, it was shown that hydrogenation could be effectively obtained by vibrationally excited H_2 molecules instead of using atomic hydrogen, since the former dissociatively adsorb on graphene on Ir(111) resulting in nanopatterned hydrogen functionalization structures [228]. Such process is made possible by the presence of the Ir surface supporting graphene, which lowers the dissociation barrier for the H–H bond, leading to the formation of H atoms that can thus hydrogenate graphene.

Graphene on Pt(111) was successfully hydrogenated, although with a lower efficiency than for Ir(111) [226]. Panahi et al. have investigated the properties of graphene and hydrogenated graphene on Pt(111) and on the Pt(111) surface with embedded Fe and Co atoms [229]. A combination of XPS investigations and C K-edge NEXAFS spectral analysis revealed a reduced graphene pinning when 3d metal atoms (Fe and Co) were embedded in the substrate compared to bare Pt(111). This was understood by acquiring core level spectra during thermal ramps (5 K/s) carried out on the hydrogenated graphene sample both for bare graphene/Pt(111) and for Fe and Co intercalated graphene/Pt(111). The different temperatures at which the components associated with hydrogenated graphene (GR-H) and with graphene in contact with the 3d intercalated metal disappear from the surface are indicating that H desorbs at different temperatures according to the intercalated species. This was attributed to the different p-doping level in graphene, which depends on the extent of the interaction with the substrate, strongly affected by the presence of 3d metal atoms in the first layer under the Pt surface. Hydrogenation was found to change the interaction between graphene and the modified substrate dramatically and to induce surface segregation of 3d atoms. The interaction of hydrogen and graphene can therefore be controlled by the presence of the 3d metals and their surface segregation. Moreover, such a mechanism changes the desorption energetics of hydrogen significantly.

Haberer et al. have shown that Au-intercalated graphene epitaxially grown on Ni(111) can be functionalized with H, which efficiently opens a band gap whose width can be tuned up to 1 eV according to the amount

of hydrogen supplied [230]. High-resolution XPS of the C 1s level showed that this hydrogen induced gap formation is completely reversible by annealing without damaging the graphene. Calculations of the BE of the C 1s upon different hydrogen loading and of the spectral function of graphene were found to be in excellent agreement with photoemission experiments. In this kind of experiment XPS was crucial in determining the H/C ratio and relate it to the observed band gap in ARPES experiments. Remarkably, the study of the same process but with deuterium instead of hydrogen showed an unusual kinetic isotope effect, since the graphene deuteration reaction proceeds faster than hydrogenation and leads to substantially higher maximum coverages of deuterium (D/C ~35% vs H/C ~25%). These results were explained by the fact that in the atomic state H and D have a lower energy barrier to overcome in order to react with graphene. More importantly, D has a higher desorption barrier than H due to quantum mechanical zero-point energy effects related to the C–D or C–H stretch vibration [231].

The specificity of the graphene/metal interface can lead the hydrogenated layer to assume peculiar features. An example of this is the hydrogenation of graphene on Ni(111) via dosing atomic H on the sample. The choice of employing atomic H has been proposed by some authors to be the most suitable route to achieve graphone, i.e. a graphene layer, where the hydrogen atoms are only on one side of the carbon sheet, which is predicted to be a semi-conductor with a smaller band gap than the aforementioned graphane. Ng and co-workers [226] first reported on the possibility to hydrogenate graphene on Ni and on other transition metals. They combined XAS and XPS measurements putting in the spotlight the differences due to the different degree of the graphene-metal interaction, also discussing the dependency on the metallic substrate of the density of graphane patches formed after hydrogenation. By combining XPS, TPD and DFT calculations, Zhao et al. [232] have studied the process of intercalation of hydrogen between graphene and the nickel substrate. They found that the highly reactive hydrogen atoms are trapped by the graphene sheet, forming covalent C–H bonds on the vacuum side of the graphene sheet.

Lizzit et al. [233] have provided a comprehensive description of the process of hydrogenation of GR/Ni(111) by using XPS and STM combined with DFT calculations. The steps of the hydrogenation (with the equivalent H doses) at room temperature are reported in Fig. 11a, going from a low dose of 0.7 kL up to 29 kL (L = Langmuir = 10^{-6} torr·s). The main C_0 peak of pristine graphene/Ni is progressively converted into new components, namely, A_1 (284.98 eV), A_2 (285.43 eV), B_1 (284.35 eV), and B_2 (283.84 eV), which, according the DFT calculation of the C1s the core level shifts (see Fig. 11b), are assigned to C atoms bonded to H monomers and dimers (A_2) and larger clusters (A_1), and to the C sites
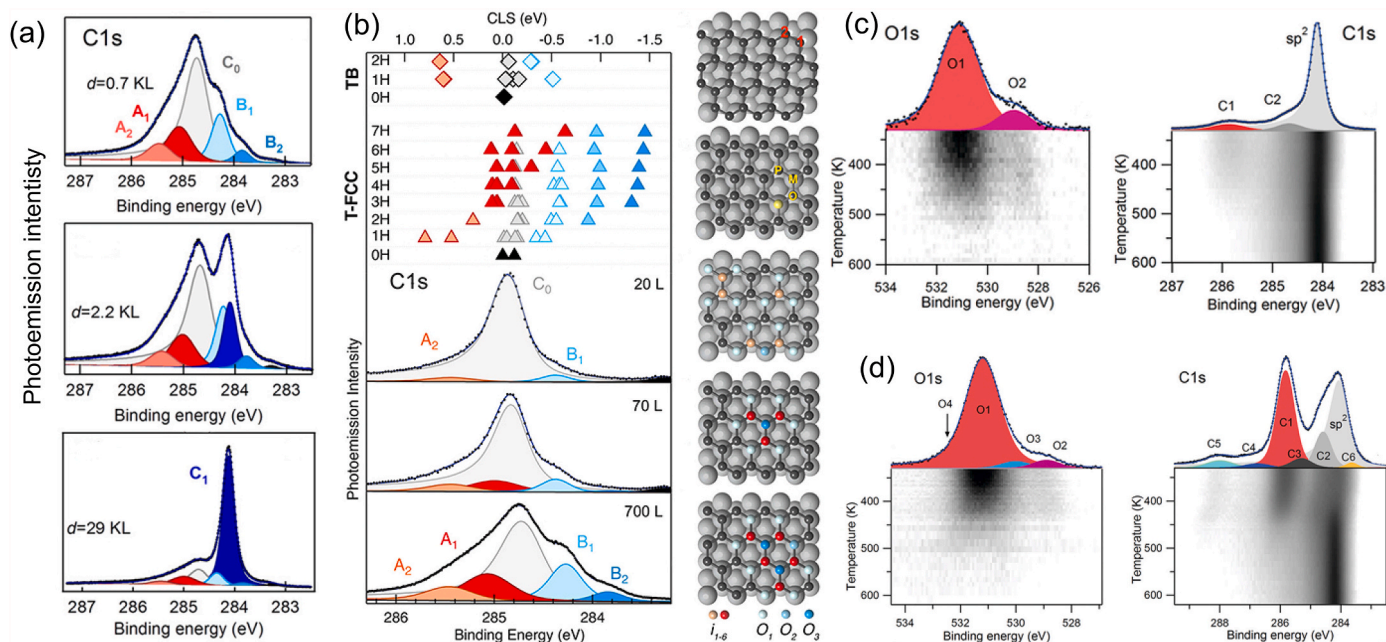
Fig. 11. (a) High-resolution C 1s spectra measured at selected doses of atomic H at room temperature, shown with best-fit curves and spectral components. The indicated H exposure d is expressed in kiloLangmuir (KL). (b) DFT calculated C 1s core level shifts for top-bridge (diamonds) and top-fcc (triangles) Gr/Ni(111) hydrogenated with H clusters of increasing sizes. On the right hand side, various geometries of the pristine and hydrogenated graphene on Ni(111). Reprinted with permission from Ref. [233] © 2019 American Chemical Society. (c) O 1s and C 1s core level spectra measured on graphene/Ir(111) with an oxygen coverage of 0.03 ML. (d) O 1s and C 1s core level spectra measured on graphene/Ir(111) with an oxygen coverage of 0.25 ML. The best fit curves and the spectral components are indicated by the blue lines and the colored peaks. Reprinted with permission from Ref. [234] © 2011 American Chemical Society. (For interpretation of the references to color in this figure legend, the reader is referred to the Web version of this article.)

that are first neighbor of one (B_1) or two and three C–H bonds (B_2). The growth of these new components proceeds until a stable configuration is reached and then, at H dose of ca. 0.6 kL, it stops indicating the saturation of the H chemisorption on graphene. With these assignments the C 1s spectrum reveals that at RT not more than one-quarter of the C atoms form C–H bonds (those contributing to A_1 and A_2). This implies that hydrogen chemisorption saturates at 0.20–0.25 ML GR. These findings are compatible with previous helium scattering measurements reporting hydrogen saturation of graphene at a H/C ratio of about 20% [235]. Hydrogenation progressively shifts the main C_0 component, which at saturation is located 0.2 eV below its BE position for clean GR and has about half of its pristine intensity. In parallel, H atoms intercalate below graphene with a much slower rate and bind to Ni surface sites. This intercalation progressively destabilizes the C–H bonds and triggers the release of the hydrogen chemisorbed on graphene. ARPES and NEXAFS measurements demonstrated that the graphene layer is fully lifted when the Ni surface is saturated with H. The same authors also reported STM images showing that at low coverage H atoms predominantly adsorb as monomers, in agreement with the calculations predicting a high stability for this arrangement. The graphene layer, besides offering a storage volume for the intercalated H, stabilizes it above room temperature, rising by a few tens of K the H_2 release temperature with respect to the bare Ni(111) surface. Moreover, this hydrogenation was proven to be reversible: whereas the H atoms chemisorbed on graphene remain unperturbed over a wide temperature range, the intercalated phase abruptly desorbs 50–100 K above room temperature. The effectiveness of these results can be expanded by using Ni substrates with large specific surface, as nanoparticles or nanostructured foils or foams, which, when covered with graphene, might become media where hydrogen can be loaded and stored above room temperature [236]. Moreover, the information achieved in this experiment were fundamental to understand the mechanism of water splitting of H_2O on graphene on Ni(111) [88].

2.4.2. Oxygen functionalization

Besides hydrogen, oxygen is the most employed species to functionalize graphene. Specifically, this process is strongly related to the understanding of the formation mechanism of graphene oxide, which, unlike graphene, is less inert and has great potential in a great deal of technology-oriented applications [237]. Moreover, the understanding of the interaction of graphene with oxygen assumes a marked importance in view of the use of graphene as efficient coating against corrosion of metals [238].

Oxygen functional groups (epoxy, hydroxyl, carbonyl and carboxyl) induce sp^3 defects in the graphene structure and distort the π-conjugated system, reducing the strength and conductivity of the material [239, 240]. Efficient reduction of graphene oxide while maintaining optimal transport properties is a key issue to address. Graphene oxide is solution processable and easy to handle: this is related to the presence of O atoms attached to the graphene lattice in several oxidizing groups, with a relative abundance controlled by the preparation method chosen [241, 242]. However, although the progressive elimination of oxygen during graphene oxide reaction results in a gradual increase of the electronic mobility, the transport properties of reduced GO are far from being comparable to those of ideal dopant-free graphene, because the sp^2 conjugation is only partially retrieved. The fundamental understanding of the oxidation and reduction mechanism can be understood by accurately monitoring the evolution of relevant core levels during oxygen exposure. Graphene on Ir(111), known to have a high degree of ordering, small amounts of surface defects, which can dramatically affect oxidation/deoxidation processes, and being quasi freestanding, constitutes an excellent benchmark to understand the oxidation of the single layer of graphene.

Atomic oxygen is generally employed to efficiently achieve this task, with O atoms sticking to the basal plane of the graphene sheet with an initially covalent bond through the formation of an epoxy group, as proven for oxidation of graphene on Ir(111) and Pt(111) [234,243]. Vinogradov et al. [243] exposed epitaxial graphene on Ir(111) to a flux

of atomic oxygen and observed that, at the first stage of oxidation, significant changes can be observed in the C 1s spectrum shape and noted that all components detected at oxygen saturation are observed since the beginning of the process. Upon further oxygen adsorption, these new components became more pronounced, at the expense of the signal from the pristine graphene, indicating an increase in the number of carbon atoms involved into the oxidation process. It was observed that graphene oxidation predominantly occurs through the formation of epoxy groups and causes atomic-scale buckling of the graphene lattice, as evidenced by an sp^2-to-sp^3 bond transformation. Annealing of the samples after oxygen exposure was able to recover only partially the original graphene structure, both for the growth on Ir(111) and Pt(111).

Larciprete et al. [234,244] shed light on the interaction of graphene/graphite with atomic oxygen, focusing on the mechanism of reduction of oxidized graphene, addressing specifically the defects formation in the C network during de-oxygenation, a process that can compromise the charge carrier mobility in the reduced material. In particular, they oxidized epitaxial graphene on Ir(111) by controlled amounts of atomic O both at low ($\theta = 0.03$ ML) and high ($\theta = 0.25$ ML) coverage. For the low coverage regime, they observed the appearance of the components O1 (531.1 ev) and C1 (285.8 eV), in the O 1s and C 1s spectra, respectively, due to the formation of epoxy structures, as shown in (Fig. 11c). The appearance of the component C2 (284.6 eV) in the C 1s and of a new component (60.66 eV) in the Ir $4f_{7/2}$ spectrum (not shown) supported the emergence of a C–Ir interaction induced by the adsorption of O atoms on graphene. On the other hand, the sample exposed to a higher O coverage, revealed a much larger number of new components in the C 1s core level (Fig. 11d), with component C3 (285.3 eV) assigned to ethers, and C4 (286.8 eV) and C5 (288.0 eV) attributed to C atoms forming double (quinones) and triple (lactones) bonds with O atoms, respectively. Carbon vacancies are responsible for the C6 component (283.6 eV) and partially responsible for the broadening of the main sp^2 peak. Double C=O bonds were held responsible for producing the O3 component (530.0 eV) in the O 1s spectrum.

Insight into the mechanism of desorption of oxygen from graphene were obtained by collecting core levels during thermal annealing of the samples with different oxygen coverage, as reported in Fig. 11c and (d). For the sample covered with low amount of O, the O desorption activates at 350 K from the epoxy groups only, as shown by the decrease of the O1 and C1 intensities, while the O2 and C2 peaks start to decrease at ca. 400 K. No oxygen adatoms were detected above 520 K, with the C 1s and Ir $4f_{7/2}$ spectra resembling those measured on pristine graphene. The thermal evolution of the C 1s and O 1s spectra for the high coverage sample shows that, similarly to the low coverage case, epoxide reduction is activated at ca. 300 K and is complete below 550 K. A residual quantity of O is still detected at 500 K in the form of ether and semi-quinone. The comparison between the C 1s spectral intensities measured on pristine and reduced graphene shows that 10–15% of C atoms are lost during the desorption ramp. This graphene etching mechanism was also observed in experiments exposing GR/Ir(111) to molecular oxygen [200], which identified a dual path mechanism in the thermal reduction of graphene oxide driven by the oxygen coverage. At low surface density, the O atoms adsorbed as epoxy groups evolve as O_2 leaving the C network unmodified. At higher coverage, the formation of other O-containing species opens competing reaction channels, which consume the C lattice through CO/CO_2 desorption.

Starting from these outcomes, other works have completed the knowledge about the mechanism of O functionalization of GR on Ir(111) by addressing the role of enolate functional groups [245]. Cassidy et al. have shown that a combination of XPS and STM with HR-EELS measurements was able to prove that O atoms covalently bind to the graphene basal plane selectively, at sites dictated by the underlying Ir(111) substrate and have demonstrated that these new bonds are with enolate functional groups [246]. A similar patterning effect, with formation of enolate groups, has been individuated also for GR on Ru(0001) [247].

2.4.3. Nitrogen and boron functionalization

The functionalization of graphene with N constitutes also a very important example of substitutional functionalization. Wei et al. have shown that it is possible to directly grow N-graphene [248], while the works of Usachov et al. [249,250] have shown in details the steps leading to the realization of a N-functionalized graphene layer on Ni (111), casting light on some interesting features of the chemistry of this interface. By thermally dissociating *s*-triazine on Ni(111), they were able to directly grow a layer with a specific C–N ratio. The analysis of the C 1s and N 1s core level acquired at different stages of growth (Fig. 12a) showed that room temperature adsorption of s-triazine molecules produces a plethora of spectral features in the C 1s spectra, indicative of a complicated dissociation process. However, two main spectral features (c1 and c2) are clearly distinguishable [249].

The first N 1s spectra exhibit a dominant feature n1 that is accompanied by a shoulder at higher BE. This can prove that triazine molecules attach with different configurations to the Ni(111) substrate. The effect of temperature on the process is also evident since, when the substrate reaches ca. 250 °C, both C 1s and N 1s photoemission signals exhibit noticeable changes. The intensity of c1 and c2 features is reduced and their energy position is shifted to higher BE. This is accompanied by the appearance of a distinct peak at ca. 283.5 eV. The shoulder n2 at 397.3 eV turned into a well-defined peak, while the intensity of the n1 feature was reduced and subsequently disappeared from the N 1s spectra. This was found to be an indication of s-triazine molecules dissociation on the hot Ni(111), with consequent appearance of molecular fragments. Last, it was observed that a substrate temperature of 500 °C was needed to have the appearance of a c3 component at 285.0 eV in C 1s and a component n3 at 399.0 eV BE in N 1s. This analysis revealed that the formation mechanism can be comparable to the CVD growth of undoped graphene, although the growth rate was found to be lower due to presence of nitrogen atoms. N-graphene has been found to be characterized by the presence of 12 at. % of nitrogen, which was observed mainly in pyridinic form and that is responsible for small charge transfer. However, the authors have shown a way to convert N into graphitic form by using the intercalation of Au under N-graphene, followed by a prolonged annealing, as deduced from the wide modifications undergone by the N 1s core level (Fig. 12c).

In this framework, the same authors have also investigated the role of the graphene-metal interaction in promoting the conversion of N from pyridinic to graphitic form [250]. In particular by applying photoemission spectroscopy and DFT calculations, they showed that the electron doping effect of graphitic N is strongly suppressed by pyridinic N. As the latter is converted into the graphitic configuration, the efficiency of doping rises up to half of electron charge per N atom. They were also able to identify the most important factor that promotes nitrogen conversion from pyridinic to graphitic form, that is the weakness of N-graphene bonding to the substrate. This is evident by the ratio of the intensities of the pyridinic and graphitic components observed for the N 1s core level for N-graphene on different substrates (Fig. 12d). The Au-intercalated GR/Ni(111) was found to be the most effective substrate in promoting the conversion, although this efficiency was not deemed to be a responsibility of the Au reactivity.

Carborane molecules were used to synthesize boron doped graphene on Ni(111) and Co(0001), incorporating B atoms in graphene already during CVD synthesis [103,251]. By combining XPS with LEED and STM, the authors have shown that impurities substitute carbon atoms in the graphene lattice and affect the orientation of graphene domains. In the case of the Ni(111) substrate B-graphene is well-oriented at low boron concentrations (< 5 at. %). At high doping level (> 12 at. %) B-graphene was found to be poorly ordered with no sublattice asymmetry. On the other end, according to the LEED data, B-graphene on the Co(0001) surface was better oriented on long-range ordering for boron concentrations up to 15 at. %; although its honeycomb lattice is strongly distorted on atomic scale, similarly to the B-graphene/Ni(111).

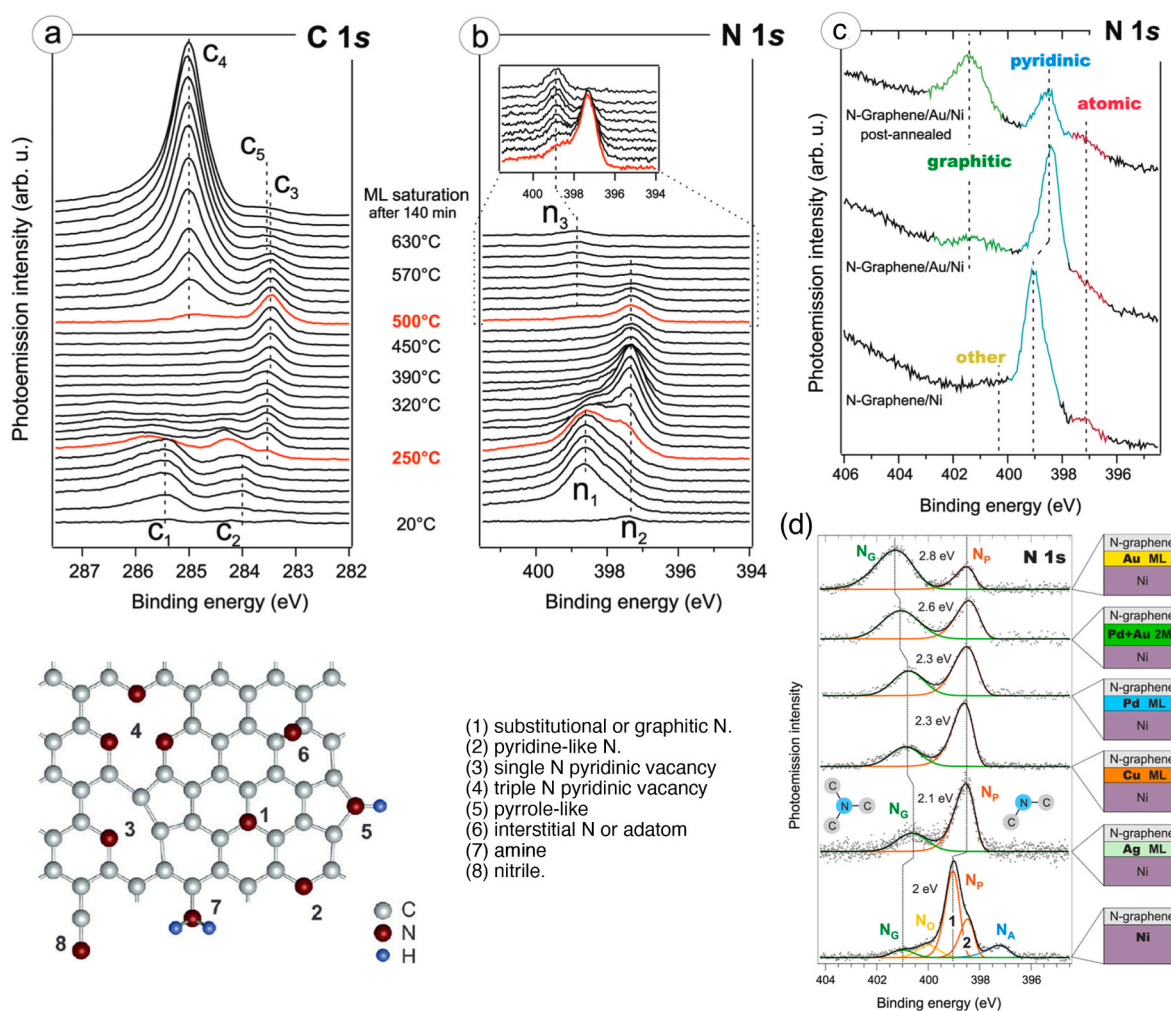Orlando et al. have shown that it is possible to obtain N-doped

Fig. 12. (a) and (b) C 1s and N 1s core level acquired during the growth of N-doped graphene. (c) N 1s core level for N-graphene on bare Ni(111), on Au-intercalated GR/Ni(111) and on annealed Au-intercalated GR/Ni(111). The central panel displays the nomenclature for the different N atoms embedded in graphene lattice. Reprinted with permission from Ref. [249] © 2011 American Chemical Society. (d) N 1s photoemission spectra acquired after intercalation of different metals under N-graphene, followed by prolonged annealing; The peaks are marked as follows: N_P, pyridinic; N_G, graphitic. Reprinted with permission from Ref. [250]. © 2014 American Chemical Society.

epitaxial graphene on Ir(111) by using nitrogen plasma treatment [252]. The acquisition of C 1s and N 1s levels, combined with XPD, lead to the individuation of different types of bonding configurations, namely, graphitic, pyridinic and pyrrolic nitrogen. The authors have shown that he GR–Ir interaction modulates the relative concentration of these nitrogen species, as it promotes the formation of pyrrolic- and pyridinic-N. The increase of the graphitic nitrogen concentration is obtained also by annealing the sample because of the higher thermal stability of this atomic configuration and of the selective conversion of the other nitrogen species. N-doped graphene synthesized in this way has shown remarkable activity in the dissociation of O_2. Scardamaglia et al. [253] have followed this process by monitoring the evolution of the core levels in a XPS experiment complemented with ARPES measurements and DFT calculations. The authors were able to observe oxygen dissociation signaled by the modification of the N 1s core level during exposure to O_2, which at the same time led to the formation of carbon-oxygen single bonds on graphene, along with a band gap opening and a rounding of the Dirac cone.

2.5. Corrugation

The possibility to have ordered long-range moiré-induced corrugation at some graphene/metal interfaces has stimulated the idea that

these interfaces could be the ideal substrate to obtain ordered depositions of arrays of clusters. Ru(0001) and Ir(111) have been mostly employed for this task, since it is possible to grow graphene on them in an epitaxial way, with large domains and well-characterized periodic corrugation, with clusters generally occupying the regions of graphene that are closer to the metal. This approach has been proven successful by the seminal works of N'Diaye et al. [254,255] and extended to other systems [122,255–260].

Beside this direct method, corrugation of the graphene layer can be obtained by directly growing graphene on surfaces with a radically different crystalline symmetry [63,64,106,261,262] or on stepped surfaces [263–267]. Casarin et al. [263] have evidenced some radical differences between graphene grown on Rh(533) and on the flat Rh(111) surface. In particular, the high-resolution C 1s spectrum of GR/Rh(533) indicated a smaller intensity ratio between the strongly- and weakly-bound graphene components (corresponding to different regions of GR close to or more distant from the Rh substrate) than in the case of GR/Rh(111) and a shift to lower BEs. The authors explained this by considering the role of the steps, which weaken the coupling between the C atoms and the metal substrate due to the increased average C-metal distance. They also suggested that the presence of surface steps may be highly beneficial to the growth of GR layers with excellent, tunable structural properties and an improved thermal stability.

Other examples to locally increase the corrugation of graphene at metallic surfaces were reported by realizing graphene nanobubbles confining Ar clusters. Zamborlini et al. [268] conducted a LEEM/PEEM investigation, followed the evolution of sub-ML amounts of argon implanted at the graphene/Ir(100) interface and provided direct evidence of Ar cluster formation at and above room temperature. The larger aggregates displayed a lateral size up to tens of nanometers and height up to several atomic layers. Other works have obtained similar structures, with the formation of nano-blisters at the GR/Ni(111) interface. Späth et al. [269] have shown that Ar can be trapped under graphene by pre-implanting it in the Ni substrate before graphene growth. The Ar then diffuses to the surface during the growth of graphene at elevated temperatures, where graphene acts as a barrier preventing it from desorbing. The authors were able to discriminate between argon atoms within the inner part of the formed bubbles and in contact with graphene, and those argon atoms in contact with the Ni(111) substrate, with the latter showing a lower Ar 2p binding energy. They concluded that the intercalation of argon leads to a decoupling of graphene from the nickel surface, as deduced from the binding energy and the thermal stability of the graphene sheet. Larciprete et al. [270] have also shown a similar process, although they grew graphene first and later implanted Ar ions in it. They then thermally annealed the so-formed samples following in real time with synchrotron-based XPS the formations of the nanoblisters by acquiring the C 1s and Ar 2p core levels. By combining XPS with STM they showed that the Gr nanoblisters, whose shapes are driven by the crystallographic directions of the Ni surface, contain multilayer Ar aggregates compressed at high pressure below the monolayer GR skin. The local strain along the blister profiles makes these nanostructures a benchmark for fundamental and application-oriented investigations and the starting point to explore the reactivity of strained graphene nanostructures and their potential inclusion in newly-designed catalysts.

2.6. Thermal expansion

The possibility to include graphene in electronic devices relies not only on the knowledge of the electronic properties but also on the understanding of its mechanical and thermal features [272–277]. In this sense, the sensitivity of synchrotron-based XPS in detecting the smallest modifications of the core level BE and lineshape was instrumental in understanding the mechanism connected to the thermal expansion of graphene. Pozzo et al. have combined DFT calculations and C 1s spectroscopy on GR/Ir(111) in a synchrotron-based XPS experiment to show the effect of thermal annealing on the graphene lattice. In order to estimate the effects of temperature on GR, the first-neighbor distance d was calculated with DFT and was found to increase with temperature i. e., it shows the usual behavior for a solid, both for free-standing and Ir supported graphene (Fig. 13a). On the other hand, when the lattice parameter a is considered, the emerging picture is quite different for the freestanding and the supported GR case. For freestanding GR a thermal contraction of a was observed for all simulation cell sizes at lower temperatures, while for supported graphene DFT calculations showed that the variation of a with temperature is positive and mainly governed by the Ir slab.

Experimental validation to these results came by acquiring the C 1s spectrum on GR/Ir(111) via fast-XPS (acquisition time 150 ms/spectrum) while the sample was undergoing a temperature ramp from 300 to 1200 K. Each spectrum was fitted with Doniach-Šunjić profiles convoluted with a Gaussian which accounts for phonon, inhomogeneous, and instrumental broadening. The analysis revealed that the single C 1s component moves to higher BEs and broadens with increasing temperature, as seen in Fig. 13c. In order to obtain information about d, the bonding/anti-bonding splitting ΔE in the C 1s core level was measured, since, in a simple tight-binding picture, this is related to the C–C distance [62]. In the observed temperature range ΔE was found to decrease from 44 ± 2 to 32 ± 2 meV, strongly supporting an increase of C–C, with a
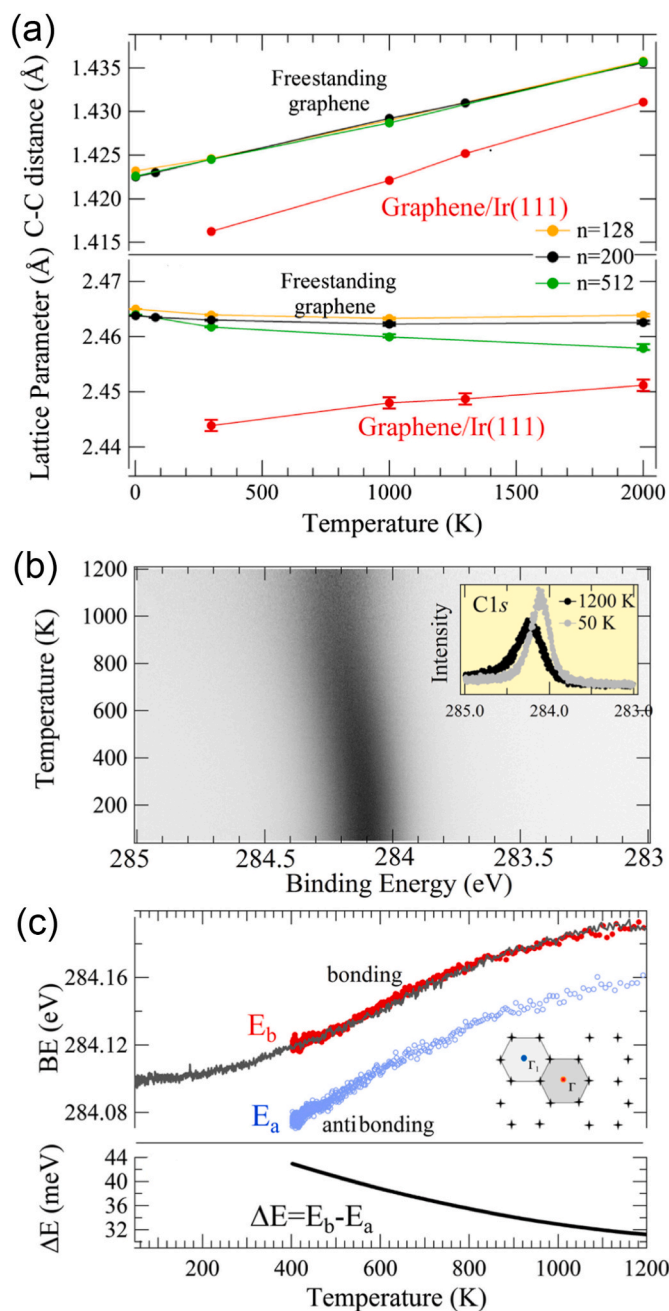
Fig. 13. (a) Calculated temperature dependence of the average C–C distances d and lattice parameter a for supported GR on Ir(111) and freestanding GR. (b) C 1s spectra acquired as a function of the temperature and shown as a 2D intensity plot. Inset: Spectra measured at the highest and the lowest temperature. (c) Temperature dependence of the C 1s BE. The gray curve is obtained from the data set shown in (b). Red [(E_b), filled circles] and blue [(E_a), empty circles] curves correspond to the bonding and anti-bonding states, respectively. (d) BE difference between the bonding and the anti-bonding component (ΔE). Reprinted with permission from Ref. [271] © 2011 by the American Physical Society. (For interpretation of the references to color in this figure legend, the reader is referred to the Web version of this article.)

trend that can be fitted well with an exponential, suggesting a linear thermal expansion of d in the whole temperature range. Further information on the graphene thermodynamic properties can be extracted from the thermal broadening of the XPS spectra, analyzing the evolution of the gaussian broadening using the Hedin-Rosengren theory for the temperature-induced phonon broadening. Such analysis allowed the determination of the Debye temperature for graphene (1495 ± 50 K),

between the values of diamond (2240 K) and graphite (402 K) [278]. These experiments have shown that the C–C nearest-neighbor distance increases with temperature for both supported and free-standing graphene, even when the lattice constant contracts. This work provides an excellent example of the potentiality of combining synchrotron light with core-level photoelectron spectroscopy, elucidating some very elusive properties of 2DMs which normally are not directly accessible with conventional XPS or other techniques.

3. Hexagonal boron nitride

Another important member of the family of 2DMs, both from a fundamental and technology-oriented point of view, is single layer hexagonal boron nitride (hBN). The studies on this 2DM at surfaces have received a considerable attention in the last years, making hBN a very versatile and promising material in view of a possible use in new-generation electronics. hBN is indeed an insulator with a wide gap, formed by B and N atoms arranged in a honeycomb crystalline lattice, with a geometrical configuration very similar to graphene. The studies about this material have been indeed often conducted in parallel with graphene, mostly because of the foreseen potentiality and importance of graphene/hBN heterostructures. Electronics based on graphene needs generally a scalable insulator, such as hBN, to deliver their predicted theoretical potential, which is usually impaired by the presence of defects of the amorphous oxide thin layer onto which graphene is laying [279]. hBN was early identified as one of the best candidate to be included in graphene-based devices, due to its large band-gap and its lack of defects and irregularities. Beside this aspect, hBN has received a considerable attention also because it constitutes an excellent template to adsorb atoms, molecules and clusters in ordered arrays [280].

3.1. Growth on metallic substrates

hBN has been synthesized and characterized on a wide set of substrates. The search for an effective and reproducible bottom-up approach has lead to the investigation of the mechanism of epitaxial growth of hBN, mostly on transition metal substrates, on which it can be grown, similarly to graphene CVD, relying on the reactivity of the metallic surface (kept at a specific temperature) to dissociate precursor molecule containing both B and N, such as borazine or ammonia borane. The results obtained in terms of growth have been recently summarized in some reviews [281–283], which also offered a survey on several aspects of hBN properties at surfaces. Multiple experiments with synchrotron-based high-resolution XPS were realized in this area, and provided essential knowledge about the mechanism of growth of hBN and important information about the adsorption configuration of hBN on the substrates on which it was grown, exploring the electronic properties of these interface. The growth mechanisms in this case can be more intricate than for graphene, since two chemical elements are involved and must be incorporated into the hBN film at a one-to-one ratio. Although the correct stoichiometry of the final layer should be ensured by the use of molecules such as borazine, for which the B:N ratio is 1, the decomposition of the precursor and the pressure used during the growth can play an important role in driving the final crystalline quality of hBN.

The growth of hBN on several metallic surfaces (in general single-crystals) and the electronic structure of these interfaces have been studied in a series of experiments with synchrotron radiation in the last 20 years [284–294]. Substrates other than metallic ones have been also explored. Epitaxial graphene was one of them, in the attempt to individuate a protocol for a direct and scalable growth of hBN-graphene heterostructures [295–297]. Early works by Nagashima et al. [298–300] have suggested that the monolayer of hBN on Ni(111), Pd (111) and Pt(111) is physisorbed, although later works showed that hBN is actually chemisorbed on Ni(111) [284]. On other surfaces, such as Rh (111) or Ru(0001), the interaction with the substrate generated

corrugation in the hBN, with regions closer and pinned to the metallic substrate. Such outcomes have been confirmed by the analysis of the N 1s and B 1s core level high-resolution spectra, since their spectroscopical fingerprint can help to shed some light on the differences of interaction of hBN with the substrate at different regions of the corrugated lattice, in the same way as it was observed for graphene.

Preobrajenski et al. [286] have extensively addressed this issue by means of synchrotron-based XPS and have shown that the morphology of hBN overlayers on lattice-mismatched TM substrates changes gradually as a function of increasing chemical bonding. Peak fit analysis of the N 1s core level reveals two components N1 and N2 separated by about 0.7 eV in the case of hBN grown on Pt(111), Ir(111), Rh(111) and Ru(0001), as shown in Fig. 14a. Interestingly, the intensity ratio of these components changes gradually: for hBN on Pt(111) the spectrum is dominated by the low BE component (N1), which is associated with nitrogen atoms in physisorbed hBN. On the more interacting Ir(111), the component N2 grows, and this happens even more evidently for hBN on Rh, for which the high-energy component becomes comparable with N1. Finally, N2 dominates the spectrum for the most reactive Ru(0001) substrate. Thus, the authors related the component N2 with nitrogen atoms in the chemisorbed hBN sites. It is worth noting that the energy positions of both N1 and N2 are shifting gradually from hBN/Pt towards hBN/Ru. This is due to the fact that weakly bound hBN is electrically decoupled from substrates, and the Fermi level of hBN and the metal is no longer aligned. From this core-level analysis, and with the support of X-ray absorption spectroscopy (XAS) data, the authors concluded that the morphology of hBN overlayers is different on each of these substrates, gradually evolving with increasing interfacial chemical interaction. In particular, the fraction of the chemisorbed hBN areas gradually increases at the cost of the physisorbed hBN ones.

The analysis of the core levels can return information about the thickness of the hBN layer on the surface, as reported in Fig. 14b, which shows that the B1s spectrum changes with the number of hBN layers grown on Ni(111) [284]. A single component (B1, BE = 190.47 eV) was observed for the single layer hBN, while for a double layer structure B1 is sided by another component at higher binding energy (B2, BE = 190.95). A further increase in the hBN thickness continues the observed trends, resulting finally in the single and nearly symmetric B 1s and N 1s lines of the bulk material with (B 1s BE = 191.82 eV and N 1s BE = 399.47 eV). The linewidth analysis of the core levels revealed that, while the bulk material spectra were not altered by any charging effects, remarkable differences were observed for the monolayer form, with an asymmetry parameter $\alpha = 0.13$ for B 1s and $\alpha = 0.06$ for N 1s. Specifically, the value of α measured for B 1s is comparable with that one measured in metals, but it is radically different to the values found in insulators. Such feature indicates the metallicity of the hBN when in single-layer form on Ni. Thus, the electronic properties of the first hBN monolayer on Ni(111) are very different from those of the second and subsequent monolayers.

The mechanism of growth of a single-layer hBN on metals has been explored by Orlando et al. by means of X-ray photoelectron spectroscopy, in order to understand the steps leading to the formation of single-layer hBN on the surface of Ir(111), using borazine as precursor [301, 302]. The evolution of the B 1s and Ir $4f_{7/2}$ core-levels at the different stages of exposure is shown in Fig. 14c. The authors observed that at low temperature (T = 170 K) borazine adsorbs on Ir(111) in its preserved molecular form, with the plane of the ring parallel to the substrate. Subsequent annealing of the borazine-covered surface resulted in a continuous dehydrogenation from ca. 250 up to ca. 1000 K, with a maximum H_2 desorption rate at 330 K (estimated from temperature-programmed desorption experiments), and eventually ends up with the formation of the hBN layer. Above T = 330 K part of the dehydrogenated molecular rings breakup, leading to the formation of molecular fragments and atomic species, as revealed by the detection of atomic boron. Deposition of borazine on the Ir surface kept at high temperature leads to the formation of an extended hBN layer. In addition
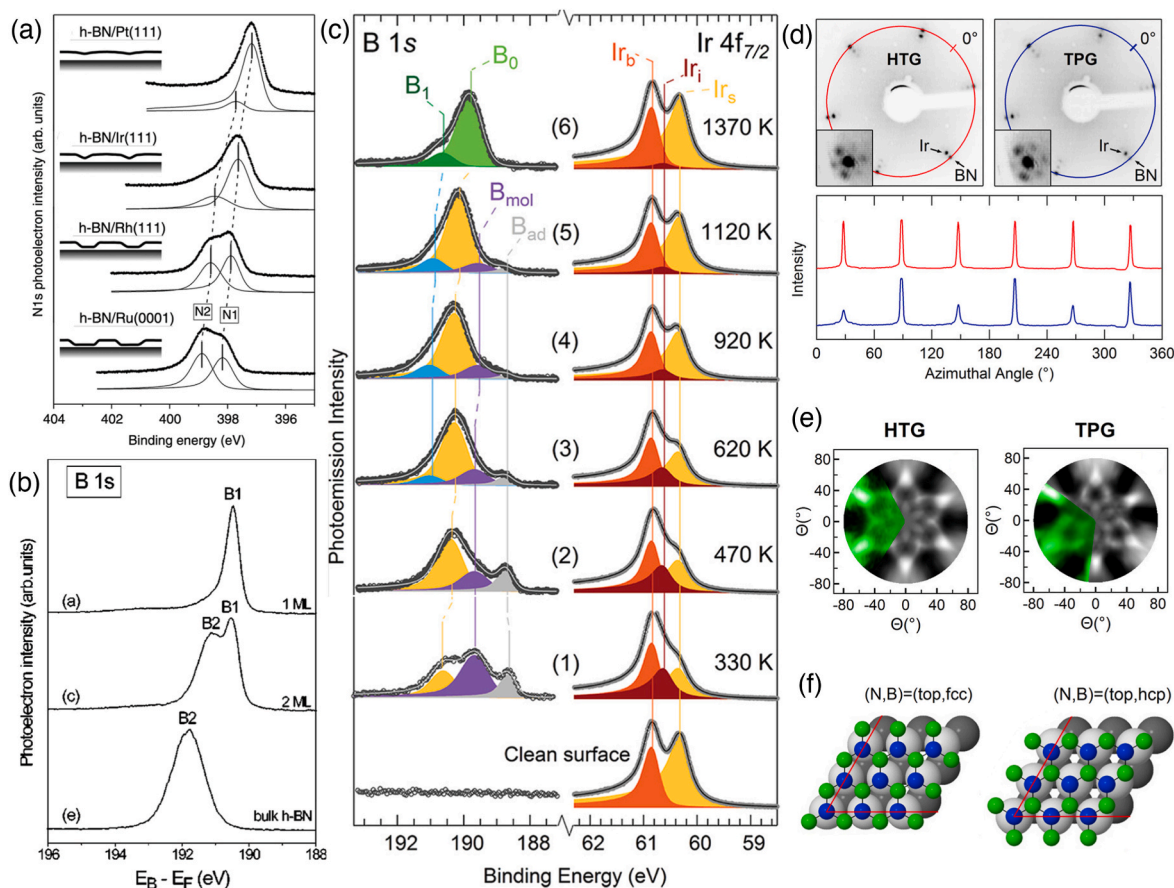
Fig. 14. (a) N 1s core level of hBN single layer on different metallic substrates. Reprinted from Ref. [286] with permission from Elsevier. (b) B 1s photoelectron lines for hBN/Ni(111) excited with $hv = 320$ eV. B1 and B2 stand for the boron chemical species in the first monolayer (B1) and all other layers (B2). Reproduced with permission from Ref. [284] © 2004 American Physical Society. (c) High-energy resolution B 1s and Ir $4f_{7/2}$ core level spectra for the clean surface (bottom) and $B_3N_3H_6$ saturated (25 L, T = 330 K) Ir surface (1) and after fast annealing to the listed temperatures. Reproduced with permission from Ref. [301] © 2012 American Chemical Society. (d) LEED patterns measured at 83 eV for hBN synthesized according to HTG and TPG procedures Insets: zoom-in of the principal spots measured at 55 eV. In the bottom panel, line profile analysis along the colored rings containing the BN spots. (e) XPD patterns stemming from B 1s acquired on hBN sample grown with HTG and TPG methods, with $hv = 305$ eV. (f) Two possible adsorption configurations for h-BN on Ir(111). Reprinted with permission from Ref. [302] © 2014 American Chemical Society.

to these details on the mechanism of formation of hBN, it was shown that a single-domain hBN monolayer can be synthesized by a cyclic dose of high-purity borazine (using the so-called temperature-programmed growth, TPG) onto the metal substrate at room temperature followed by annealing at T = 1270 K. The single crystalline orientation was inferred by comparing LEED diffraction pattern, featuring a 3-fold symmetry expected for the hBN crystalline lattice with a single orientation (Fig. 14d), and from X-ray photoelectron diffraction (XPD) experiments (Fig. 14e). In contrast, high-temperature borazine deposition (labeled high-temperature growth, HTG, and performed keeping the metallic substrate at 1070 K) resulted in a hBN monolayer constituted by domains with opposite (mirror) orientation and thus characterized by an overall 6-fold symmetric diffraction pattern. The compelling evidence of the single-layer formation was achieved through XPD experiments. The B 1s derived XPD patterns are reported in Fig. 14e. By comparing the experimental data (colored sector) with XPD simulated patterns obtained via multiple-scattering calculations [303], it was possible to identify the best crystalline structure matching the experimental XPD outcomes via an R-factor analysis [17]. This analysis revealed that, although the crystalline symmetry of hBN layers is identical to that of the Ir(111) substrate, 180° misoriented h-BN domains are formed by the HTG method, corresponding to *fcc* and *hcp* configurations, which are shown in the scheme in Fig. 14f. On the other hand, the TPG preparation method was found to produce only the *fcc* phase. The authors

individuated the thermal energy and the binding energy difference between *fcc* and *hcp* hBN seeds as crucial factors controlling the alignment of the growing hBN clusters during the first stage of the growth.

3.2. Functionalization

After some early studies provided a comprehensive knowledge about the growth of hBN on metallic surfaces, it was anticipated that the regular superstructures associated with the moiré of the hBN on the metal surface could constitute an excellent template to achieve the ordered adsorption of atoms, molecules and clusters. The possibility to have an ordered substrate which does not contain carbon or oxygen has made hBN an ideal platform for the production of nanocatalysts, nanomagnets, and functionalized surfaces rich in C and O. The interaction of various atomic species with single-layer hBN thus became a relevant topic, efficiently investigated by means of synchrotron-based XPS, with the final aim to pinpoint modifications induced in the nanomesh by the adsorbed species and, possibly, to modify in a controlled manner the electronic structure of hBN [281]. The regular nature of the corrugation of many hBN/metal interfaces makes them ideal candidate substrates to deposit ordered arrays of clusters [306–309]. The chemical and electronic nature of hBN could lead to think that it features a resistance to functionalization. Nevertheless, it was proven that functionalization is achievable and consequent electronic structure

modifications could be obtained for hBN as well. Several XPS experiments have shown that this task could be accomplished by dosing non-metallic [304,305,310–312] and metallic [313–316] atoms.

Späth et al. [304] have studied the interaction of H with hBN on Ni (111). The adsorption of atomic H leads to significant alteration in the B 1s and N 1s core levels (Fig. 15a). For low exposures of 1 and 90 L, the B 1s peak of hBN at 190.5 eV broadens and shifts towards lower BE, while a more distinct effect is visible for the N 1s core level. Indeed, in addition to a decrease and slight broadening of the N1s peak of hBN at 398.5 eV, a pronounced shoulder emerges at 397.9 eV. Higher exposure to atomic H lead to an even larger broadening of B 1s and a further down shift of the N 1s with the appearance of a peak at BE = 397.7 eV. More information about the interaction of H and its thermal stability on hBN were obtained by measuring the evolution of the N1s core level of hBN with different levels of hydrogenation upon thermal annealing. For the sample exposed to 1 L of H, the N 1s remained unaltered up to ca. 600 K. An intermediate case was found for the sample exposed to 140 L of H, with both de-intercalation (390 K) and dehydrogenation (550 K) being observed. Last, for the sample exposed to 600 L only de-intercalation (390 K) took place, as indicated by the 1.0 eV shift towards higher BE of the N 1s peak. By combining these results with the outcomes of XAS and TPD, the authors have thus individuated two competing regimes of interaction of hydrogen with hBN. The first is a chemical bond formation for low exposures of H, which they describe as hydrogenation of hBN, while the other regime is intercalation of atomic hydrogen, which lifts the interaction of hBN with the substrate, resulting in new features in both XAS and photoemission spectra. However, in both cases, the interaction with hydrogen decreases the n-doping effect of hBN, which is compatible with the observed shift of the core levels. Similar results have been obtained by Wei et al. for hBN on Pt(111) [312]. By using near ambient pressure XPS and exposing the sample to 0.1 Torr H_2, they found that hydrogen intercalation occurs and that the intercalated hydrogen desorbs almost completely at ca. 470 K, while only partial hydrogen desorption takes place for the bare Pt(111) under the same experimental conditions. This indicates that the confinement effect of the hBN cover weakens the hydrogen-Pt interaction. This process was studied also for the hBN/Rh(111) system [310].

The effect of atomic oxygen adsorption on the structure and electronic properties of monolayer hBN on Ir(111) has been studied by Simonov et al. by combining XPS and NEXAFS [305]. The oxidation occurs mainly by embedding in the hBN lattice O atoms that replace the N atoms. This mechanism can be understood by observing the modification undergone by the O 1s core level (Fig. 15c), with a first component (BE = 531.4 eV) assigned to O substituting N in the hBN lattice, and a second one (BE = 530.1 eV) assigned to O intercalated between hBN and Ir substrate. The authors showed that in this process B atoms can occur in four chemically non-equivalent environments, corresponding to the parent BN_3 unit and three oxygen-substituted $BN_{3-x}O_x$ (with $x = 1,2,$ 3) units. These four different environments are responsible for the four $\pi*$ resonances in the B K-edge absorption spectra. It has been shown that embedding of O atoms leads to a significant deformation of the hBN overlayer. Annealing of the oxygen-saturated hBN monolayer could not recover the pristine configuration but leads to the formation of B_2O_3-like structures and an almost total destruction of the hBN layer.

The deposition of Au atoms on hBN/Ni(111) was found to produce an intercalated Au layer decoupling hBN from the substrate [317], thus driving the formation of a layer of quasi-freestanding hBN. Similar results were obtained also for hBN on Ru(0001) [318]. Such alteration was clearly visible in the BE shift towards higher BE of 0.7 and 1.1 eV for the B1s and N1s core levels, respectively. Such modification in the core level was indicative of an altered valence band structure, as it was observed from ARPES measurements. This mechanism is very similar to the decoupling of a graphene layer on Ni(111) described earlier [94]. The interaction of Au clusters and the formation of an Au intercalated layer were also studied by Ng et al. for hBN on Rh(111) and compared with the case of the flatter hBN/Pt(111) [319]. The authors showed that, while on clean Rh(111) substrate Au starts to grow two-dimensionally, in the presence of hBN the Au islands are formed from the very beginning. In the case of flat hBN monolayer on Pt(111) the Au islands are essentially three-dimensional and irregular in size. In contrast, on the
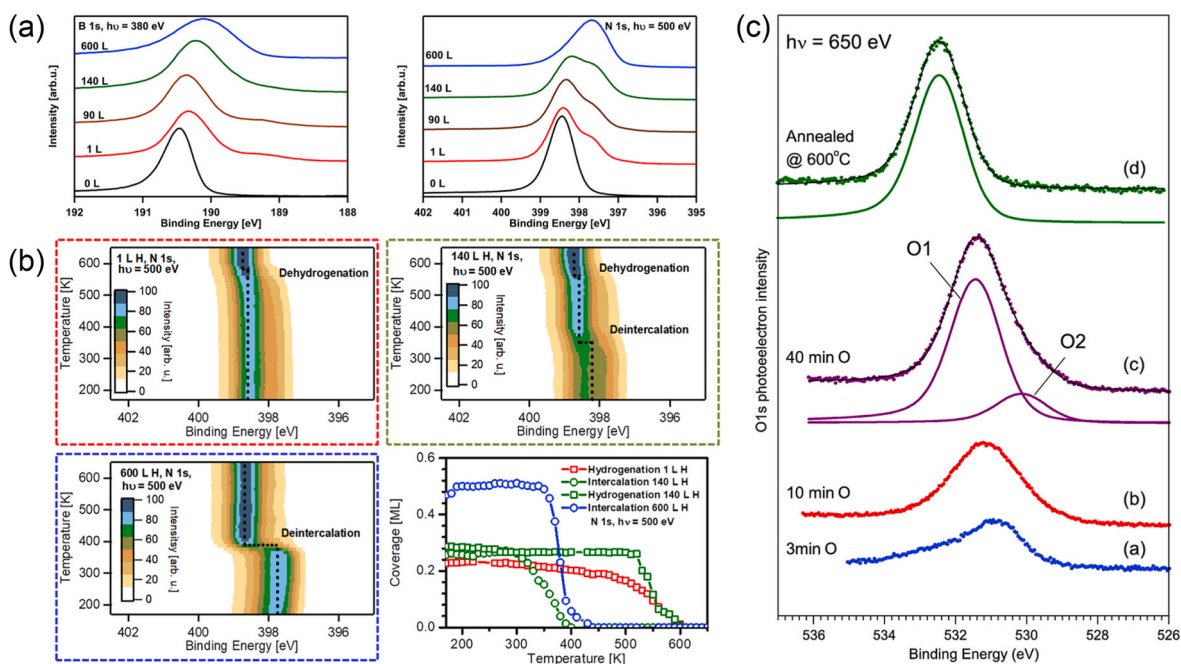

Fig. 15. (a) B 1s and N 1s core level of hBN on Ni(111) exposed to atomic H at different coverages (reported next to each spectrum). (b) N 1s core level acquired during thermal ramps of H-functionalized hBN on Ni(111) with different H coverages. Reproduced with permission from Ref. [304] © 2017 IOP Publishing Ltd. (c) O 1s core level acquired on hBN on Ni(111) for different O exposures and (green spectrum) after annealing at 600 °C. O1 and O2 are the two components resulting from the spectral decomposition. Reproduced with permission from Ref. [305]. © 2010 Elsevier. (For interpretation of the references to color in this figure legend, the reader is referred to the Web version of this article.)

hBN nanomesh on Rh gold grows initially as regular islands (predominantly 2D), probably filling the pores of the nanomesh. By monitoring via XPS and XAS the evolution of these islands upon annealing, the authors were able to find that the Au atoms diffuse through the hBN layer and adsorb on the Rh substrate and/or desorb from the surface, while the hBN nanomesh remains intact.

The quasi-freestanding hBN obtained via Au intercalation of hBN/Ni (111) was successfully functionalized with alkali-metal atoms such as Li and K by Fedorov et al. [314]. In this way the authors were able to considerably alter the electronic structure of hBN monolayers, as indicated by the observed shift of the B 1s and N 1s core levels towards lower BE. Despite being a process similar to that one observed for graphene/graphite, the authors claim that these effects are not due to charge transfer but rather to interfacial electric fields that yield potential differences between the substrate and hBN. The different shift for the N 1s and B 1s core levels was ascribed to a combination of initial- and final-state effects originating from the charge reorganization at the hBN plane due to the dopant deposition.

The work by Verbitskiy et al. reports an interesting bottom-up approach to synthesize atomically precise hBN–Ge interfaces with GeB_3N_3 stoichiometry [315]. Ge intercalation on hBN/Ni(111) resulted in well-defined interfaces between the 2D layer and Ge, with reconstruction observed after intercalation. Using XPS and measuring the Ge 3 d at the various steps of the process the authors were able to follow the evolution of Ge intercalation, as shown in Fig. 16 The authors have

shown that this process proceeds very similarly for both GR/Ni(111) and hBN/Ni(111) interfaces, conducting the two experiments in parallel. As-deposited Ge shows a broad and weakly resolved Ge 3 d doublet corresponding to Ge clusters adsorbed on the hBN surface,. During thermal annealing, the Ge atoms begin to intercalate under the hBN layer and the Ge 3 d line splits into two doublets corresponding to bulk and surface components, separated by 0.4 eV. Annealing the samples to 720 K leads to the formation of a fully Ge-intercalated hBN. As a consequence of the formation of this layer, the N 1s core levels were shifted by −0.75 eV and B 1s by −0.3 eV towards lower BE. Further annealing (820 K) leads to the disappearance of the low-energy GeS related component and is accompanied by shifting of the hBN core levels back to the initial higher binding energy. The authors have shown, combining XPS with ARPES and NEXAFS, that this annealing at 820 K drives the formation of a Ni_2Ge alloy supporting the hBN, which looses its quasi-free standing character.

4. Transition-metal dichalcogenides

As we have seen in the previous sections, the research conducted on graphene and hBN has developed a wide series of strategies to synthesize and functionalize these two important compounds on surfaces, setting the pace and a roadmap for further developments of other 2DMs. The research effort on single-layer transition metal dichalcogendies (TMDCs) has moved from such a wealth of knowledge, with the purpose
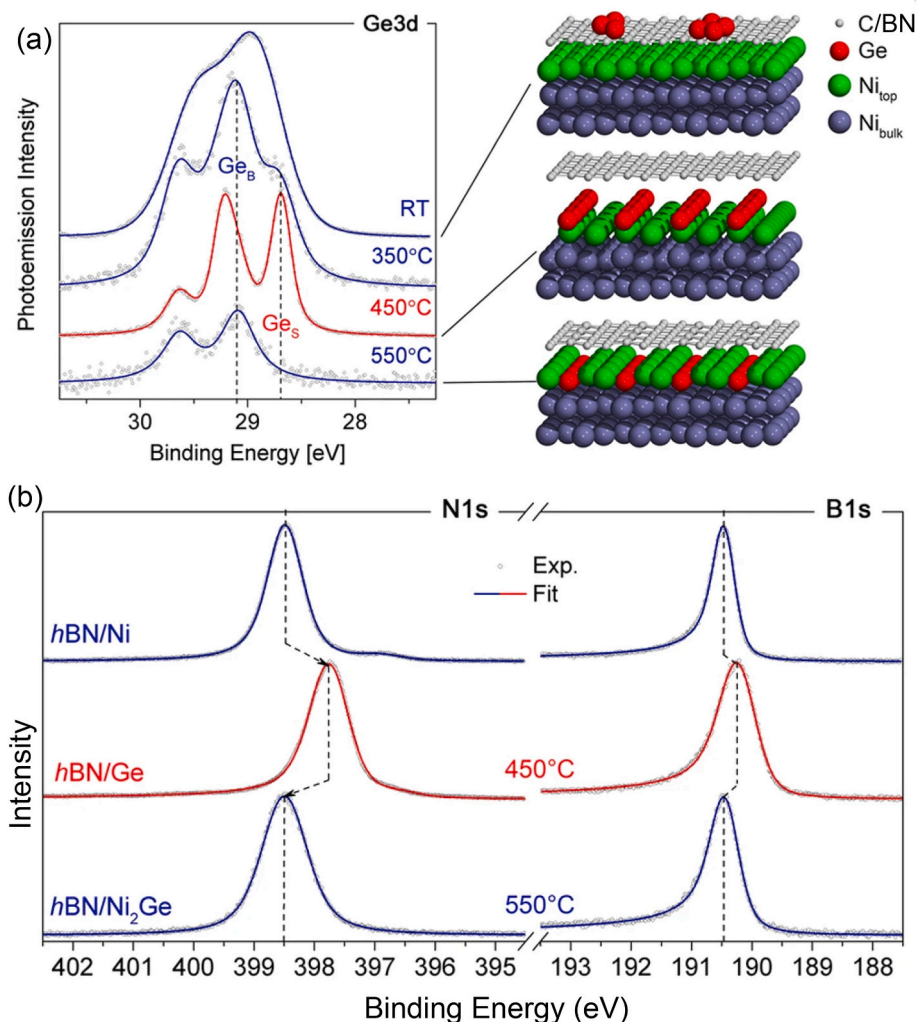

Fig. 16. (a) Evolution of Ge 3 d core-level spectrum during annealing after Ge deposition, with structural model showing the corresponding steps of Ge intercalation. (b) B1s and N1s core-level photoemission spectra before and after Ge intercalation. Reproduced from Ref. [315]. © 2015, The Authors.

to explore the properties of this class of materials in reason of the broad number of potential applications in electronics, optoelectronics and catalysis [320–325]. TMDCs constitute a wide family of compounds formed by a transition metal atom (e.g., Mo, W, Ta, V, Re, Pt) and a chalcogen atom (S, Se or Te). They exist in several structural phases resulting from different coordination spheres of the transition metal atoms. The two more common structural geometries are characterized by either trigonal prismatic (2H) or octahedral (1T) coordination of metal atoms [326,327]. Similarly to graphene, also for these family of materials the bulk parent compound has properties which can be radically different from those of the single layer counterpart. One of most striking examples of these modifications is the transition from indirect bandgap to direct bandgap semiconductor that MoS_2 undergoes when downscaling it from the bulk to the single layer form, with the emergence of a strong photoluminescence observed only for the monolayer [328].

The contributions given from a surface science perspective to the knowledge about these materials are certainly very broad, as shown in a recent review by Lasek et al. [329], which offers a wide and comprehensive overview about the investigations on electronic and structural properties of TMDCs at surfaces. For the scopes of our review, we will provide some remarkable examples underlining how core-level photoelectron spectroscopy was able to address some elusive issues concerning the growth and characterization of TMDCs at surfaces.

4.1. Growth mechanism

SL TMDCs are a class of compounds that can be obtained via mechanic exfoliation, owing to the van der Waals nature of the forces between the various layers of the bulk materials. However, since such approach is certainly neither scalable nor suitable for technological applications, considerable efforts have been devoted to the understanding of the mechanism of direct growth of TMDCs at surfaces and to clarify the role played by the chosen substrate in determining the features of the final layer. Hence the growth through bottom-up protocols

such as physical vapor deposition (PVD), molecular beam epitaxy (MBE) and chemical vapor deposition [330,331] have gained more space with respect to the mechanical exfoliation. A wide set of the studies aiming to understand fundamental aspects of TMDCs were carried out by growing them directly on non-metallic substrates (e.g. graphene, hBN, but also sapphire, silicon oxide) [330] and on noble metal single crystals, with a preponderance of studies using the Au(111) surface. While the first set of substrates was chosen in view of their potentiality in assembling van der Waals heterostructures, Au(111) is often the best substrate since it is generally inert to the chalcogenide precursor molecules used in the synthesis process. This choice was successful and allowed the preparation of a large set of SL TMDCs directly on surfaces [332–348].

For the most relevant and studied of the TMDCs, i.e. MoS_2, core-level photoemission was instrumental to understand the mechanism of growth of the single layer on several ordered substrates, and highlighted the importance of the TMDC-substrate interaction and its effect on the properties of the final layer. The deposition of Mo atoms in a H_2S atmosphere in UHV at RT was proven to be a viable way to grow single layer MoS_2 on Au(111). It was observed that uniform MoS_2 single layers could be achieved by a cycle-based approach [340,342,349–351], with a preliminary deposition of Mo in a H_2S atmosphere in UHV, followed by a thermal annealing always in sulfur-rich atmosphere. The relevant core level measured showed a wealth of information about the electronic features of the grown systems.

Sorensen et al. [349] and Bruix et al. [350] were among the first to measure the core levels of the MoS_2 layers on Au(111) and observed that the Mo 3d and S 2p BE positions were lower than those observed for bulk MoS_2(0001) crystals, hinting at some interaction effects due to the Au substrate (Fig. 17a and b). Bruix et al. [350] also explored the activity of the edges of the MoS_2 islands grown in situ on Au(111) and were able to find the contributions given by the different atoms in a MoS_2 nanoisland to the spectral lineshape of Mo 3d and S 2p core levels (Fig. 17 c-f). Combining spectra acquired on the partially-sulfided Mo–S compounds with DFT calculations of the core levels (Fig. 17c and e) the authors were able to show that the Mo $3d_{5/2}$ core level has several core-level shifts
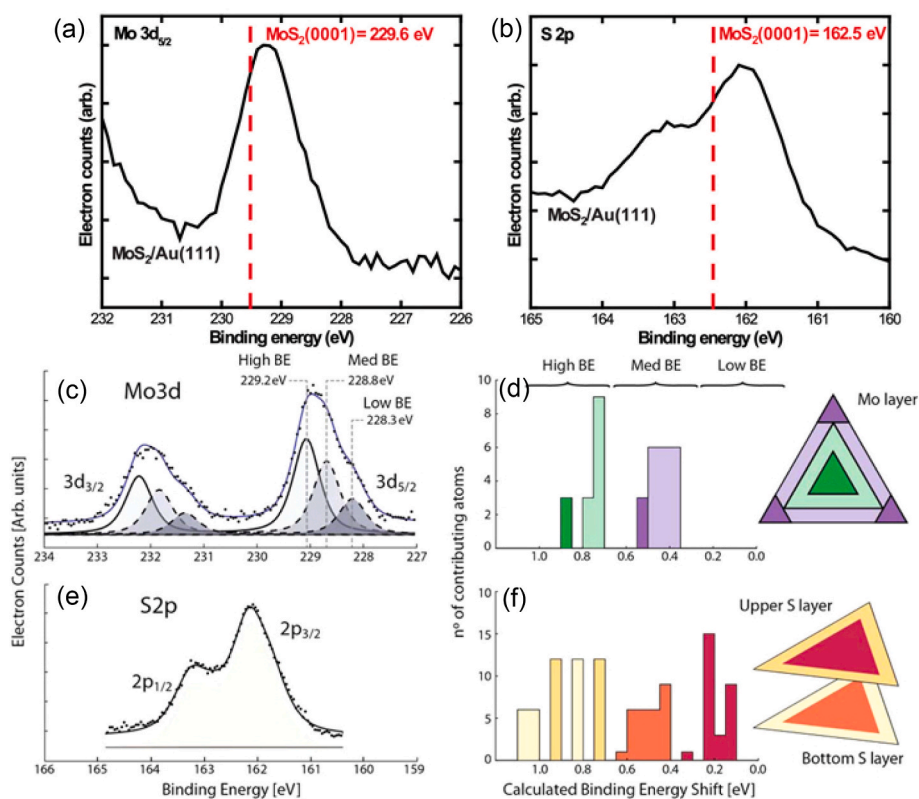

Fig. 17. (a) Mo $3d_{5/2}$ (photon energy 340 eV) and (b) S 2p (photon energy 220 eV) core level spectra of single layer MoS_2 islands on Au (111). The red lines indicate in each case the BE position measured on MoS_2(0001) single crystal. Reproduced with permission from Ref. [349] © 2014 American Chemical Society. (c) Mo 3d and (e) S 2p XPS spectra recorded at RT on Au(111) supported MoS_2 nanoparticles. The corresponding DFT-calculated BE shifts are shown in (d) for Mo 3d and in (f) for S 2p spectra. Reprinted with permission from Ref. [350]. © 2015 American Chemical Society. (For interpretation of the references to color in this figure legend, the reader is referred to the Web version of this article.)

that belong to Mo atoms located in different positions of the MoS_2 triangular islands. In addition, it was observed that the interaction between MoS_2 and the Au substrate splits each of the peaks of the S 2p doublet into two components, one at higher BE, related to the bottom S layer atoms in contact with Au(111), and a lower BE peak, originating from the upper S layer.

The shift toward larger BE for those S atoms in contact with Au was interpreted as due to the formation of S–Au bonds. Moreover, monitoring the evolution of Mo 3d during the exposure of these islands to high-pressure H_2 provided some important information about of the transitions involved in desorption of S and adsorption of H. Remarkably, the edge reduction process, with the S coverage going from 100% to 50%, leads to a shift toward higher BE of the Mo 3d core level, a feature assigned to variations in the metallic character of the Mo edge. Information about the activity of the MoS_2 edges could also be obtained on samples grown ex-situ, identifying the XPS fingerprint of the structural defects in CVD grown MoS_2 and demonstrating that when thermal annealing causes sulfur to desorb from the basal plane of MoS_2 vacancies with more than one missing sulfur atom are created [352]. It was also proven that MoS_2 can be efficiently grown by sulfidation of MoO_3 on surfaces, with an approach used often for CVD growth of TMDCs [330] Using well-defined oxidation states of Mo-oxide precursors, Salazar et al. [351] combined synchrotron-based XPS and STM to determine the role of morphology and oxidation state of the Mo oxide precursor in the formation of MoS_2 single-layer structures on Au(111).

Bana et al. [333] pointed out that a very important parameter governing the growth of SL MoS_2 on surfaces, is the growth rate, which may affect critically the final crystalline structure. By following the growth in real time by means of fast-XPS, the authors were able to grow single layer MoS_2 directly on the Au(111) at high temperature, tuning the Mo and S deposition rate to achieve only the desired species. Exceptionally sharp Mo 3d core levels with a single component were observed and assigned to MoS_2, in agreement with the results of Sorensen [349]. Also in this case, a clearly distinguishable contribution from bottom and top S atoms in the S 2p core level was observed. The single layer grown with this protocol showed very high degree of long-range ordering, as testified by STM images acquired on the sample (Fig. 18b), with MoS_2 covering the atomic terraces and steps of the surface. The average domains size was estimated to be of the order of 100 nm estimated using spot-profile-analysis (SPA)-LEED. Moreover, in the same works, the authors explored the structural features of the grown layer by means of photoelectron diffraction from the Mo 3d and S 2p core levels. The results confirmed that MoS_2 on Au(111) assumes the 1H polytype. It was possible to determine the adsorption configuration of the single layer and, most notably, to prove that the layer had a single crystalline orientation. The latter is a feature extremely desirable for the exploitation of the valley and spin-orbit degrees of freedom in TMDCs, which relies on the absence of mirror domains and thus the lack of inversion symmetry in the Brillouin zone [353]. Such feature resulted in a out-of plane spin polarization of the electronic states in the valence band of 86 $\pm$ 14%, opposite for states at the K and -K points of the Brillouin zone.

Epitaxially grown SL WS_2 on Au(111), first realized with a cycle-growth protocol [336,338], was also obtained in a single-layer with a single crystalline orientation, following the direct growth approach developed for MoS_2 [335]. Once more, the very sharp W 4f and S 2p core levels were indicative of the presence of WS_2 only on the Au substrate
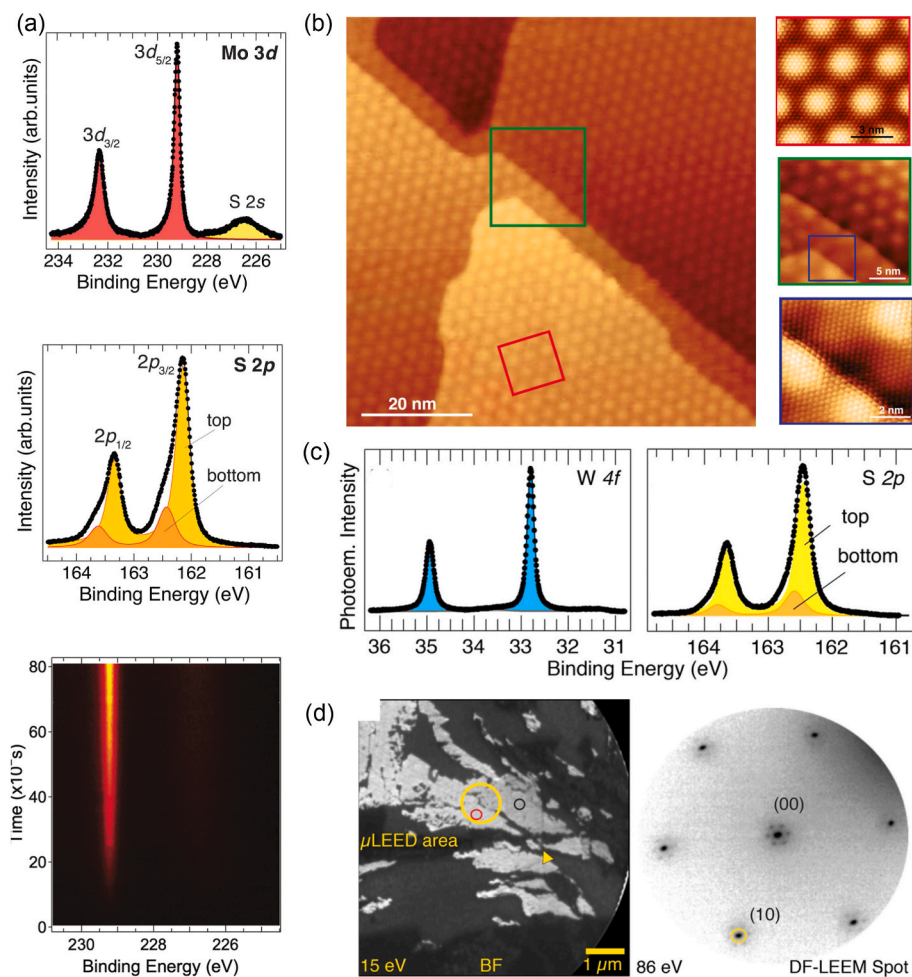

Fig. 18. (a) Mo 3d and S 2p core levels acquired on single-layer MoS_2 on Au(111). At the bottom, evolution of the Mo $3d_{5/2}$ component measured during the growth of SL MoS_2 on Au. (b) STM images acquired ad different magnification levels on SL MoS_2 on Au (111), showing the characteristic moiré pattern. Reprinted and adapted with permission from Ref. [333]. © 2018 IOP Publishing LTD. (c) W 4f and S 2p core levels for SL WS_2 on Au(111). (d) LEEM image acquired on the sample with μLEED measured in correspondence of the yellow circle. Reprinted with permission from Ref. [335] © 2019 by the American Physical Society. (For interpretation of the references to color in this figure legend, the reader is referred to the Web version of this article.)

(Fig. 18-c), for which it was again possible to discriminate top and bottom S atoms in the TMDC sandwiched structure. These observations were combined with XPD measurements and µ-LEED measurements (Fig. 18-d), indicating the formation of large, singly-oriented crystalline domains. The subsequent investigations of the spin structure of valence and conduction bands (via angle-resolved photoemission and inverse photoemission) confirmed the (expected) out-of-plane spin polarization of electronic states in the vicinity of the Fermi level, with spin-dependent energy splitting [334,339].

The acquisition of high-resolution core-level spectra was also crucial in understanding the growth mechanism and features of MoS_2 on other noble metal faces such as Ag(111) [354] and Ag(110) [355]. In the case of the growth on Ag(110), the deposition process had additional parameters to consider, such as the stronger TMDC-substrate interaction with respect to the Au(111) case and the possible chemical reactivity of the metallic substrate with the S-carrying precursor (H_2S), which could lead to the formation of Ag–S bonds. Unlike the case of Au(111) it was not possible to grow a singly-oriented MoS_2 layer, despite the stronger interaction of MoS_2 with the substrate. Also, a consistently different two-step growth had to be adopted to prevent the formation of randomly-oriented MoS_2 crystalline domains. However also in this case, even if the crystalline symmetry of the MoS_2 and the Ag(110) is completely different, MoS_2 single layers can be grown displaying only two mirror orientations. These examples indicate that the growth of TMDCs is governed by variables which cannot be easily predicted but can be specific of each couple TMDC-substrate considered.

In this framework, important examples of this variability can be found when attempting a direct growth of ordered MoS_2 and WS_2 layers on van der Waals substrates, which is a crucial requirement in view of building graphene-TMDCs heterostructures with a scalable, bottom-up approach. As highlighted earlier, the growth on van der Waals substrates has the drawback to yield TMDCs layers which are generally having a large azimuthal disorder, as proven by the experiments to grow MoS_2 on sapphire [356,357], graphene [342,358,359] and silicon oxide [360]. The direct growth of TMDCs on graphene is certainly in the spotlight because of interests in exploiting the electronic and catalytic effects of this interface. Such heterostructure has been prepared successfully, with different degrees of ordering in the TMDC layer. Hall and co-authors [361] have highlighted the importance of the substrate temperature and of the H_2S pressure in the different stages of growth of MoS_2, WS_2 and TaS_2 on epitaxial graphene on Ir(111), identifying the best conditions to obtain ordered layers limiting the presence of randomly-oriented crystalline domains. Moreover, Loi et al. have more specifically investigated the growth of MoS_2 on epitaxial graphene through synchrotron-based XPS and have confirmed the primary role played by the substrate temperature during the growth in driving the formation of MoS_2 and investigated the thermal stability of the interface [362]. They have also highlighted that during the growth the temperature promotes efficient sulfur intercalation under graphene, with the subsequent dissolution of sulfur in the Ir bulk. Specifically, the S intercalation under graphene was found to be a process in direct competition with the MoS_2 formation, thus potentially disrupting the formation of an ordered interface.

4.2. Stoichiometry and structural modifications

As shown by the experiments investigating the growth mechanism of the widely-investigated MoS_2 and WS_2, the preparation of these materials on surfaces may be intricate and not entirely straightforward, with a considerable number of variables governing the growth and affecting deeply the features of the final layer.

The case of the growth of VS_2 on Au(111) constitutes a remarkable example of this complexity [332]. This TMDC is quite challenging to obtain experimentally since it has the quite unusual characteristics of having no thermodynamically stable bulk polymorph, with a 1 T structure that tends towards S-deficient structures and V intercalation

between the sulfur layers [364]. Combining high-resolution core-level spectra with photoelectron diffraction, STM and LEED measurements was crucial to unravel the novel crystalline phases formed by VS_2 epitaxially grown on Au(111), which formed an impressive series of crystalline (1 T) phases. Each one of these three phases showed clear differences both for the S 2p and V 3p core levels, as shown in Fig. 19 (a)-(f). In the S 2p spectra, the green peaks originate from S atoms at the top of the layer, orange and red from S atoms at the bottom of the SL and the blue peaks are unordered sulphide species. One of the phases (phase I) is of the type 1 T-VS_2 and has a bulk analogue, even though the stoichiometric bulk VS_2 is metastable. Such compound could be extremely interesting to probe in terms of magnetic properties. Heating the VS_2 layer in vacuum showed the formation of a S-depleted structure with an increased in-plane lattice constant (phase I′). Last, a new other 2D form of $V_{1+x}S_2$, called 'phase II', is in many ways even more interesting, as it does not have a bulk analogue, thus paving the way to further investigations on its properties. These results were capital to determine the correct crystalline structure of this compound for each of the different phases observed (and sketched in Fig. 19g–i). The colored spheres in the upper-right-hand corners of the data panels indicate the atoms corresponding to the XPS components with same color. It is worth noting in these schematics the blue and red spheres in panel (i), which indicate down-modulated atoms and up-modulated top-S atoms, respectively.

Other examples that show how the complicated stoichiometry and the effects of the growth parameters on it can be accurately sorted out by XPS are offered by the studies about the mechanism of growth of other TMDCs such as selenides [363,365–368]. Bonilla et al. have studied for VSe_2 on MoS_2 the effects of the de-selenization induced by thermal annealing in vacuum and linked the changes in stochiometry to modifications in the structural configuration [363]. Such changes are signaled by the radically-different core-level shapes observed for Se 3d at various photon energies and at different stages of the annealing (Fig. 19j-l). The as-grown sample clearly shows the spin–orbit splitting of 0.9 eV and can be fit with a single doublet, with the Se $3d_{5/2}$ at BE = 53.4 eV (Se1, red). The Se 3d core level exhibits two distinct components Se1 and Se2 for an annealed vanadium selenide sample, while no appreciable differences were observed for the V 2p spectrum. Such large modification in the Se 3d were attributed to a loss of selenium in vacuum and a conversion of single layer TMDCs into bilayer materials, due to the intercalation of the metallic atoms that lost a Se atom in between two layers of the TMDCs, as shown in the schematic on the right-hand side of the panel. Such behavior was observed both for VSe_2 and $TiSe_2$.

Similar investigations focused on the growth and electronic structure of tellurides, another sub-family of the TMDCs group, which usually is synthesized on surfaces via MBE in UHV [365,369–374]. For these materials, effects and behavior similar to those observed for VS_2 and VSe_2 were reported and throughly investigated by means of high-resolution XPS. Lasek et al. [375] have studied the effect of temperature annealing on the growth of Ti, Cr, V tellurides on HOPG or MoS_2 single crystals. They observed that such annealing leads to the coexistence of telluride layers with adventitious, but periodically-ordered, metallic layers, which are formed by the transition-metal atoms of the grown TMDC and covalently bound to the TMDC layer. Moreover, these metallic layers show a crystalline structure very similar to TMDC itself, a feature that can easily lead to misinterpretation of ultra-thin films grown by MBE. However, the authors showed that these few-layer intercalation compounds, terminated by TMDC layers, are essentially constituting a new van der Waals material and can be useful building-blocks for MBE-grown van der Waals heterostructures. Such mechanism was observed also by means of STM, for other TMDCs, namely $MoSe_2$ and $MoTe_2$ [376]. Other important insight into the intricate stoichiometry in the formation of Pt tellurides [377] have been obtained, pointing out, also for these compounds, the role played by post-growth annealing in vacuum, with the consequent loss of chalcogen atoms that drives the formation of new crystalline
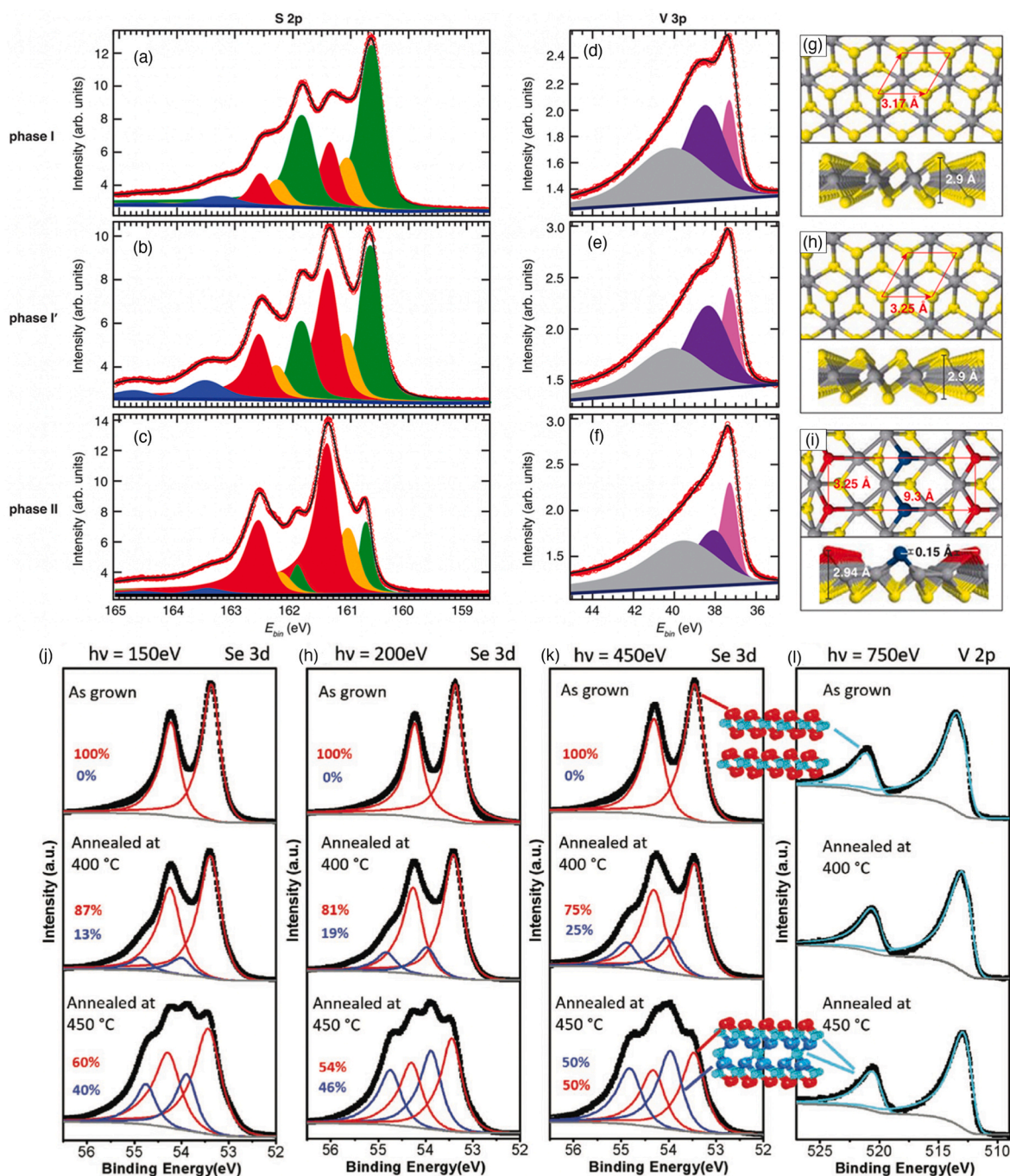
Fig. 19. XPS spectra of the three phases of single layer $V_{1+x}S_2$. (a)–(c) XPS spectra for S 2p core-level states ($h\nu = 260$ eV). (d)–(f) XPS spectra for the V 3p state. The schematics on the right hand side—(g), (h), (i)– report the structures used for the interpretation of the XPD data. Reprinted with permission from Ref. [332], © 2018 IOP Publishing Ltd. (j)–(l) High-resolution XPS for Se 3d and V 2p core levels for different annealing temperatures. The blue and red numbers in the Se 3d spectra represent the percentage of the Se1 and Se2 components with respect to the total spectral weight. Reproduced with permission from Ref. [363] © 2020 WILEY-VCH Verlag GmbH & Co. KGaA, Weinheim. (For interpretation of the references to color in this figure legend, the reader is referred to the Web version of this article.)

arrangements with a different stoichiometry with respect to the as-deposited compounds.

4.3. Functionalization and Janus TMDCs

The possibility to remove chalcogen atoms from the top layer of the TMDC sandwich stimulated the researchers to try to understand the functionalization of TMDCs on surfaces. XPS has played an important role in the preparation and characterization of the so-called Janus TMDCs, i.e. TMDC layers with different surface atoms on the two sides of

the TMDC sandwich. These materials have been extensively studied from a theoretical point of view due to the unique properties induced by symmetry breaking, and promising applications in energy conversion. However, despite the large amount of theoretical studies conducted, only few experimental works, and only very recently, have reported reliable methods to prepare Janus SL on surfaces [378,379].

The synthesis of a SL MoSSe was reported by Lu et al. [380], who grew, in the first place, single crystalline MoS_2 monolayers on c-plane sapphire substrates using CVD. Subsequently the top-layer sulfur atoms were stripped off and replaced with hydrogen atoms using a remote

hydrogen plasma. Last they exposed the sample to Se to substitute H and form the MoSSe structure. In this context, the authors used synchrotron-based energy-dependent XPS to probe the asymmetric structure of the MoSSe monolayers, by changing the incoming photon energy from 250 to 1150 eV. The core level doublets from S 2p and Se 3p levels for a MoSSe monolayer appeared at around (162.4; 163.6) eV and (161.3; 167.1) eV, respectively. To verify the Janus structure, the authors compared these results with several MoS$_x$Se$_y$ monolayer samples with a randomized S and Se distribution, that is without a precise stoichiometry, revealing considerable differences. The authors argued that the percentage of Se derived from the XPS peak intensity and corrected by a relative sensitivity factor, should be independent on the emission angle if the sample is vertically homogeneous in composition. On the contrary, the intensity measured was strongly dependent from the emission angle, indicating an inhomogeneous composition in the vertical direction, i.e. perpendicular to the TMDC layer.

Zhang and co-authors [381] have synthesized a Janus MoSSe via a controlled sulfurization process of MoSe$_2$. The authors have conducted a comprehensive characterization of the system, using both Raman mapping and time-of-flight secondary-ion mass spectroscopy (TOF-SIMS) element mapping, combined with XPS profile analysis, showing that the monolayer is uniformly sulfurized and the asymmetric structure distributes all over the Janus monolayer. Sant et al. [382] have epitaxially grown a SPtSe layer using a single-layer of PtSe$_2$ on Pt(111) as starting point with exposure to H$_2$S atmosphere, revealing through grazing incidence synchrotron X-ray diffraction the steps of formation of the Janus compound. The authors have cast light on the layer-by-layer chemical composition, using angle-resolved X-ray photoelectron spectroscopy and they have proved that the replacement of the Se atoms by S atoms occurs selectively only in the topmost layer of chalcogen atoms.

Although the formation of Janus TMDCs can be considered as a sort of functionalization, more specific attempts have been carried out trying to functionalize TMDCs at surfaces, following the methodologies already individuated by investigations on graphene and hBN. Examples of the application of this strategy have been reported for some TMDCs, with examples of intercalation [383–385], doping with metals [386], and molecular functionalization [387–389]. Adsorption of single atoms, for example, has been investigated for the case of Co atoms on 1T-MoS$_2$ [390]. Qi et al. have proven that the transformation from 2H to distorted-1T, induced by strain from lattice mismatch and formation of Co–S covalent bond between Co and MoS$_2$ during the assembly, is essential to form the highly active single-atom array catalyst, with a Pt-like activity toward the hydrogen evolution reaction and high long-term stability. These results are very promising and we believe a comprehensive investigation of the properties of functionalized TMDCs will be certainly pursued in the next years, with high-resolution XPS playing a central role in elucidating the mechanism of functionalization and guiding scientists towards a comprehensive understanding of the formation mechanism of TMDCs.

5. Borophene

Borophene, the 2D allotrope of boron, constitutes one of the last individuated and most promising 2DMs with very suprising properties, such as highly anisotropic electronic structure, ultrahigh thermal conductance, mechanical compliance, phonon-mediated superconductivity and optical transparency [391–393]. Boron, similarly to carbon, is able to form fullerenes and nanotubes [394,395], although, as seen for Si and Ge, this is not automatically ensuring the possibility of having a 2D stable structure. Theoretical calculations however, have predicted the existence of a 2D boron allotrope. Nevertheless, unlike graphene and hBN, which can be prepared both in supported and in free-standing form, borophene can be stabilized only on a substrate, although some works have been recently shown the possibility to prepare unsupported borophene [396]. Although theoretical efforts have guided the experimentalists, borophene sheets have been synthesized experimentally only

on a few substrates, with the first successful attempt reported in 2015 [397]. Nevertheless, extensive literature describes the formation of planar B clusters on surfaces [398].

Moreover, despite the simpler chemical nature if compared, e.g., to many TMDCs, the geometrical configuration assumed by borophene can change radically depending on the growth conditions and on the surface on which it is synthesized, a significant difference with graphene and hBN, which show instead unique and distinctive crystalline configurations with a well-defined crystalline symmetry. This reflects the wealth and complexity of the possible crystalline structures that boron can assume in the bulk form, with many different polymorfs predicted, but only four have been successfully synthesized [399,400]. To a simplified extent, borophene can be seen as a triangular lattice of B atoms with either buckling or periodic vacancies in different motifs and concentrations, with buckling being less energetically favorable than vacancies. Penev et al. have provided a comprehensive overview of this polymorphism and structural anisotropy, evaluating from a theoretical point of view the structural stability of the various layers [401].

To date, borophene structures have been succesfully grown on Ag (111) [397,404,405], Ag(110) [406], Au(111) [407], Cu(111) [408], Ir (111) [403,409,410] and Al(111) [411,412]. Despite this set of studies, a systematic investigation of the core levels of these different interfaces is still lacking, with the majority of the works reported focusing on determining the structural configuration assumed by borophene, mainly by STM and LEED experiments. However, it has been shown that a wealth of details on the structure and conformation assumed by borophene on surfaces can be obtained through high-resolution XPS.

5.1. MBE growth of borophene

From an experimental point of view, the strategy generally adopted to grow borophene is based on MBE evaporation of B onto a metallic substrate, generally a single crystal, kept at a specific temperature, although this method may produce borophene layers with some polymorphy. In this respect, the conditions of growth and the chosen substrate can significantly impact on the final borophene crystalline structure. As reported by Feng [404] and Mannix [397,413], the MBE growth on Ag(111) generates two radically different crystalline arrangements depending on the substrate temperature during the growth. STM experiments [404] have shown that with substrate temperature below 400 °C the β_{12} was formed, while above that temperature the formation of χ_3 structure was favored. These two structures (shown in Fig. 20a) are radically different in terms of crystalline arrangement, electronic structure, B vacancies and non-equivalent B atoms. The β_{12} has a 2:2:1 ratio of 4-fold, 5-fold, and 6-fold coordinated B atoms while the χ_3 shows a 1:1 ratio of 4-fold and 5-fold coordinated B atoms. Differences in the coordination numbers of the non equivalent B atoms in the borophene lattice on Ag(111) can be resolved by means of synchrotron-based high-resolution XPS. Campbell et al. [402] have shown that non equivalent B atoms, i.e. atoms with a specific coordination number in the borophene layer, yield significantly different core level shifts in the B 1s spectrum. In Fig. 20 we show the B 1s core level measured on the layers grown below and above the critical temperature of 400 °C, thus showcasing the spectral signature of the two different crystalline structures. For the β_{12} (R) phase, the three different spectral components (in blue) are symptomatic of three different non-equivalent boron atoms, with BE assigned to the peak decreasing with the coordination number. Likewise, for the layer grown above the critical temperature only two components were observed, which reflects the presence of only 5-fold and 4-fold coordinated B atoms in the χ_3 (D) phase. Interestingly, the authors were not able to synthesize borophene layers with a single phase, but rather had a mixture of the two, with the temperature of growth that seemed to play a crucial role in determining the relative abundances of the two phases. Kiraly et al. [407] have shown that, unlike growth on Ag substrates, boron diffuses into Au at elevated temperatures and segregates to the surface to form borophene
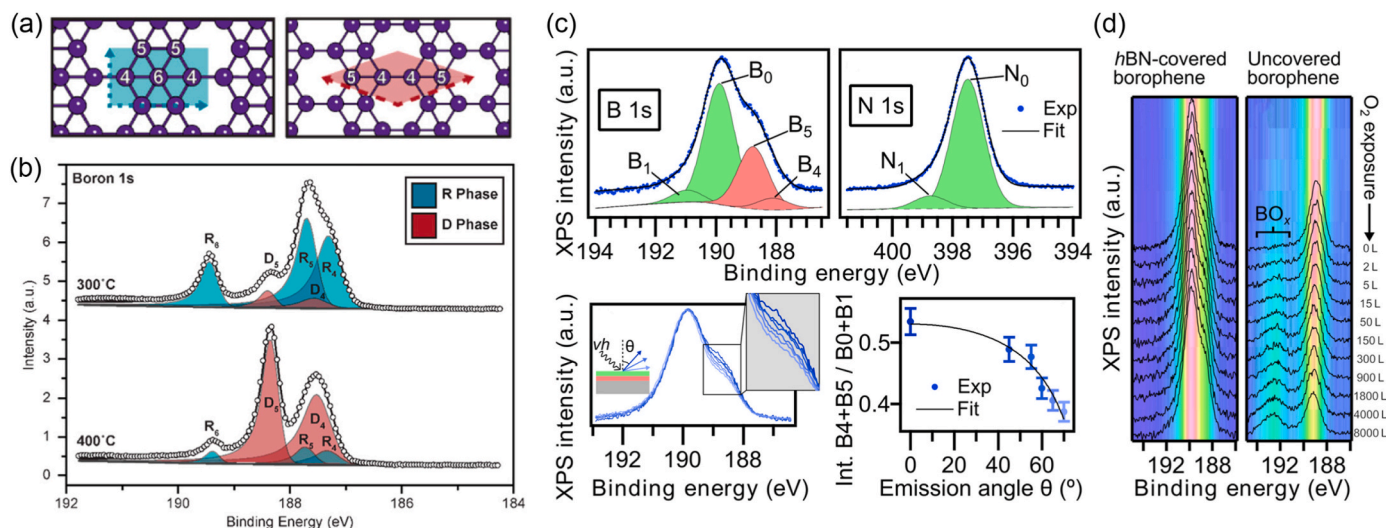
Fig. 20. (a) Schematic of the β_{12} and χ_3 borophene structures formed on Ag(111) and (b) the corresponding B 1s core levels. Reprinted with permission from Ref. [402] © 2108 American Chemical Society. (c) B and N 1s XPS spectra. (d) B 1s peak measured at different photoelectron emission angles $\theta = 0°$, 45°, 55°, 60°, 65°, and 70° (lines from dark to light blue), with angular dependence of the relative intensity of borophene B 1s components and Beer-Lambert law fit. (e) Series of B 1s spectra measured on hBN-covered borophene after incremental O_2 exposure. From [403] © The Authors, some rights reserved; exclusive licensee AAAS. Distributed under a CC BY-NC 4.0 license. Reprinted with permission from AAAS. (For interpretation of the references to color in this figure legend, the reader is referred to the Web version of this article.)

islands as the substrate cools. Moreover, the formation of borophene induces modifications of surface reconstruction of the Au(111) substrate, resulting in a trigonal network that templates growth at low coverage. On Au(111) borophene has a metallic character.

5.2. Growth from molecular precursors

Beside using MBE evaporation of B, it has been recently proven that exploiting B-rich molecules can lead to the formation of a borophene layer without the polymorphs variability observed using growth via MBE. Omambac et al. [410] have shown through x-ray photoelectron spectroscopy that dosing borazine at 1100 °C on Ir(111) yields a boron-rich surface without traces of nitrogen, the first step towards the formation of a borophene layer. At high temperatures, the borazine thermally decomposes, nitrogen desorbs, and boron diffuses into the substrate. By means of time-of-flight secondary ion-mass spectrometry, the authors showed that the subsurface boron segregates back to the surface, forming borophene. Cuxart et al. [403] have shown the possibility to grow layers of metallic borophene on Cu(111) and Ir(111) single crystals, by exposing the surface to diborane and borazine. In addition to this result, the authors were able to form atomically precise lateral borophene-hBN interfaces or vertical van der Waals heterostructures on the Ir(111) surface. The latter play a very important role in protecting the borophene layer from oxidation, one of the major drawbacks in attempting to include borophene in devices. The XPS B 1s spectrum of the vertical heterostructure (Fig. 20c) has a highly asymmetric peak shape that can be decomposed in contributions from borophene (B4 and B5) and hBN (B0 and B1). The dominant intensity of the hBN low-energy component B0 over B1 (ratio 10:1), is typical of weakly interacting hBN layers with low degree of corrugation. This is consistent with the rotational domains and flat hBN observed by STM and LEED. The N 1s spectrum shows accordingly two main components N0 over N1, with the same intensity ratio of 10:1. To verify the alignment of the vertical heterostructure, angle-dependent XPS of B 1s was carried out, reported in the bottom panels of Fig. 20c. The spectra were fitted to extract the intensity of the various components vs the emission angles at which they were acquired. Borophene components (normalized by those of hBN) were observed to decrease while θ increases. This is attributed to the attenuation effect of the hBN cover, as the intensity drop is well

described by the Beer-Lambert law, and the same effect is not observed in the case of the lateral heterostructure. The protective effect of the vertical structure on the borophene layer can be seen by comparing the spectra of the vertical heterostructure vs. the uncovered borophene (Fig. 20d). In the latter, the B 1s core level is drastically altered by O_2 exposure, with the appearance of a component at higher BE, assigned to oxidized boron, while the hBN covered borophene remains identical.

Preobrajensky et al. [412] have studied the borophene-Al(111) interface by means of a combination of core-level synchrotron-based spectroscopies, STM, LEED, and large-scale DFT calculations. The authors showed that, unlike graphene on lattice-mismatched metal surfaces, honeycomb boron grows not as a quasi-freestanding monolayer and does not carpet the Al(111) surface, but rather induces reconstruction of the top metal layer. Borophene on this metallic substrate is bound and lattice-matched to the top Al layer, forming a stoichiometric one-layer AlB_2, which is instead lattice-matched. This difference is due to strong chemical bonding between the boron layer and the supporting Al layer. With increasing B coverage, thicker AlB_2 films were formed, with intercalation of B atoms under the already formed AlB_2 layers and embedding into the bulk of an Al crystal. The intrinsic complexity of the multiple borophene structures, which derives from the very rich stoichiometry of bulk B [399], and their dependency on the substrate on which it grows are certainly making more complicated to directly synthesize this material on more substrates, including insulating ones, or finding a feasible way to lift and transfer it to other substrates. Moreover, many features about the functionalized form of borophene and of its properties such as doping and defects are not well-understood. XPS with synchrotron light will be able to address these issues, following the strategies implemented for many other 2DMs [414].

6. Summary and outlook

In this review, we have showcased several studies with the purpose of highlighting the importance of synchrotron-based high-resolution XPS in the investigation of 2DMs and showed the invaluable contribution given by this technique in unveiling and understanding many features of this class of materials. The publications that we have selected represent the potentialities of XPS performed with synchrotron radiation to elucidate complicated and intricate aspects relative to the growth

mechanism and to the specific features of pristine and functionalized 2DMs at surface. In this sense, an important contribution to this success was given by the possibility to acquire fast-XPS spectra with synchrotron radiation, owing to the high photon brilliance available at synchrotrons and to the development of electron detectors with increased efficiency and reduced acquisition times. Specifically, we believe that the knowledge about the properties of graphene- and hBN-based interfaces has reached a considerable maturity point. As we have shown in Section 2 and 3, countless possibilities due to different substrates for synthesis and due to vast choice of functionalizing species have shown a clear way to fine-tune and control the properties of the pristine graphene and hBN on surfaces. These outcomes, together with the investigations carried out by means of ARPES and STM, have given to the scientific community a comprehensive overview on the properties of these materials, which will constitute pillar knowledge for their implementation in technological applications.

Such a vast research effort on graphene and hBN has set a course to develop investigation methodologies and strategies to fully characterize the vast family of TMDCs. We have shown in section 4 that a large set of TMDCs has been synthesized on surfaces to date and their properties have been studied and compared with their bulk parent compounds, revealing significant differences. However, the higher degree of complexity of these materials, due to the more complicated stoichiometry and crystalline structure, requires extra care in devising effective synthesis strategies, which have to take into account the effects of several growth parameters on the final layer. The capability of XPS of individuating the differences in stoichiometry and oxidation state in a compound is thus central to address the issue of controlled growth, and can lead to the ultimate goal of controlling the properties of TMDCs adjusting the growth conditions. In this sense, there are still many possibilities open, especially when referring to the functionalization of TMDCs, with a vast set of properties to be investigated and elucidated in details. On the other hand, the knowledge about the growth of borophene is still at the early stages, as it is complicated by the possible different polymorphs that can be produced in the MBE growth, as shown in Section 5, although the individuation of apt molecular precursors to achieve the borophene layer on some metallic surfaces has address efficiently this issue.

Besides the materials mentioned specifically herein, we believe there is still plenty of room for the development and isolation of other new 2DMs. As an example, we quote the recent paper by Mounet et al. [415], in which the authors have built a database of exfoliable compounds by systematically analyzing and screening the experimental structures extracted from structural databases, developing a geometrical algorithm to select potentially layered materials, from which 2DMs can be easily synthesized. In this way, the authors have formed a subset of easily (1, 036) or potentially (789) easily exfoliable compounds, highlighting how the fraction of 2DMs explored so far is considerably small with respect to the possibilities given in nature. The authors state that materials with reduced symmetry or involving more than two atomic species but still with relatively simple structures are certainly of interest and they suggest that the identification of the most common prototypes could also allow to further expand the list of 2D materials by chemical substitutions and alternative site decorations. In this respect, XPS will play an essential role in individuating the best ways to synthesize these new materials. At the present stage, an important part of the efforts in this field are concerning the study of 2D metallic oxides [416–419] and of MXenes [420,421], which constitute two important families of materials and whose importance will rise due to their wide spectrum of properties and possible applications. A very important task for the scientific community in the next years is certainly the realization and investigation of the properties of heterostructures and hybrid materials based on pristine and functionalized 2DMs, and the possibility to combine these architectures with single atoms, atomic clusters and nanoparticles, with the aim to produced tailor-made nanoarchitectures designed for a specific task or process. Beside standard, in vacuo XPS, it is important to mention the recent developments of near-ambient pressure (NAP) XPS. This technique allows the acquisition of spectra in near-ambient pressure conditions i.e. few tens of mbar pressure. In this way XPS can be performed in conditions comparable to those of typical catalytic reactors in the chemical industry, to access directly the dynamics of many relevant reactions [422–426]. We believe that this technique can provide another significant boost to the knowledge about 2DMs and especially about their possible inclusion in applications oriented towards chemistry technology.

In summary, we strongly believe that the output of core-level photoelectron spectroscopy experiments with synchrotron radiation will be able to continue to stimulate the research efforts of the vast scientific community interested in 2DMs, offering guidance in scouting and synthesize new combinations of materials with outstanding properties and to ease the realization and characterization of them.

Declaration of competing interest

The authors declare that they have no known competing financial interests or personal relationships that could have appeared to influence the work reported in this paper.

Acknowledgments

References

[1] K. Siegbahn, Electron spectroscopy for atoms, molecules, and condensed matter, Rev. Mod. Phys. 54 (1982) 709–728, https://doi.org/10.1103/RevModPhys.54.709.

[2] W. Egelhoff, Core-level binding-energy shifts at surfaces and in solids, Surf. Sci. Rep. 6 (1987) 253–415, https://doi.org/10.1016/0167-5729(87)90007-0.

[3] S. Hüfner, Photoelectron Spectroscopy, third ed., Springer Berlin, Heidelberg, 2003 https://doi.org/10.1007/978-3-662-09280-4.

[4] K. Siegbahn, Electron spectroscopy for chemical analysis (ESCA), Philos. Trans. R. Soc. A 268 (1970) 3357.

[5] C.S. Fadley, Atomic-level characterization of materials with core- and valence-level photoemission: basic phenomena and future directions, Surf. Interface Anal. 40 (2008) 1579–1605, https://doi.org/10.1002/sia.2902.

[6] F. Reinert, S. Hüfner, Photoemission spectroscopy—from early days to recent applications, New J. Phys. 7 (2005) 97, https://doi.org/10.1088/1367-2630/7/1/097.

[7] P.S. Bagus, E.S. Ilton, C.J. Nelin, The interpretation of XPS spectra: insights into materials properties, Surf. Sci. Rep. 68 (2013) 273–304, https://doi.org/10.1016/j.surfrep.2013.03.001.

[8] S. Hüfner, Very High Resolution Photoelectron Spectroscopy, Springer Berlin, Heidelberg, 2007, https://doi.org/10.1007/3-540-68133-7.

[9] G. Greczynski, L. Hultman, X-ray photoelectron spectroscopy: towards reliable binding energy referencing, Prog. Mater. Sci. 107 (2019), 100591, https://doi.org/10.1016/j.pmatsci.2019.100591.

[10] S. Lizzit, A. Baraldi, A. Groso, K. Reuter, M.V. Ganduglia-Pirovano, C. Stampfl, M. Scheffler, M. Stichler, C. Keller, W. Wurth, D. Menzel, Surface core-level shifts of clean and oxygen-covered Ru(0001), Phys. Rev. B 63 (20) (2001), 205419, https://doi.org/10.1103/physrevb.63.205419.

[11] L. Köhler, G. Kresse, Density functional study of CO on Rh(111), Phys. Rev. B 70 (16) (2004), 165405, https://doi.org/10.1103/physrevb.70.165405.

[12] L. Bianchettin, A. Baraldi, S.d. Gironcoli, E. Vesselli, S. Lizzit, L. Petaccia, G. Comelli, R. Rosei, Core level shifts of undercoordinated Pt atoms, J. Chem. Phys. 128 (11) (2008), 114706, https://doi.org/10.1063/1.2841468.

[13] A. Baraldi, Structure and chemical reactivity of transition metal surfaces as probed by synchrotron radiation core level photoelectron spectroscopy, J. Phys. Condens. Matter 20 (2008), 093001, https://doi.org/10.1088/0953-8984/20/9/093001.

[14] A. Baraldi, L. Bianchettin, E. Vesselli, S. de Gironcoli, S. Lizzit, L. Petaccia, G. Zampieri, G. Comelli, R. Rosei, Highly under-coordinated atoms at rh surfaces: interplay of strain and coordination effects on core level shift, New J. Phys. 9 (5) (2007) 143, https://doi.org/10.1088/1367-2630/9/5/143.

[15] C. Papp, H.-P. Steinrück, In situ high-resolution X-ray photoelectron spectroscopy – fundamental insights in surface reactions, Surf. Sci. Rep. 68 (2013) 446 487, https://doi.org/10.1016/j.surfrep.2013.10.003.

[16] A. Baraldi, G. Comelli, S. Lizzit, M. Kiskinova, G. Paolucci, Real-time X-ray photoelectron spectroscopy of surface reactions, Surf. Sci. Rep. 49 (2003) 169–224, https://doi.org/10.1016/s0167-5729(03)00013-x.

[17] D. Woodruff, Adsorbate structure determination using photoelectron diffraction: methods and applications, Surf. Sci. Rep. 62 (2007) 1–38, https://doi.org/10.1016/j.surfrep.2006.10.001.

[18] D.P. Woodruff, Surface structural information from photoelectron diffraction, J. Electron. Spectrosc. Relat. Phenom. 178–179 (2010) 186 194, https://doi.org/10.1016/j.elspec.2009.06.008.

[19] M.V. Kuznetsov, I.I. Ogorodnikov, D.Y. Usachov, C. Laubschat, D.V. Vyalikh, F. Matsui, L.V. Yashina, Photoelectron diffraction and holography studies of 2D materials and interfaces, J. Phys. Soc. Jpn. 87 (2018), 061005, https://doi.org/10.7566/jpsj.87.061005.

[20] D.N. Basov, M.M. Fogler, A. Lanzara, F. Wang, Y. Zhang, Colloquium: graphene spectroscopy, Rev. Mod. Phys. 86 (2014) 959–994, https://doi.org/10.1103/RevModPhys.86.959.

[21] S.-K. Mo, Angle-resolved photoemission spectroscopy for the study of two-dimensional materials, Nano Converg 4 (1) (2017) 6, https://doi.org/10.1186/s40580-017-0100-7.

[22] J.A. Sobota, Y. He, Z.-X. Shen, Angle-resolved photoemission studies of quantum materials, Rev. Mod. Phys. 93 (2) (2021), 025006, https://doi.org/10.1103/revmodphys.93.025006.

[23] J. Zhong, H. Zhang, X. Sun, S.-T. Lee, Synchrotron soft x-ray absorption spectroscopy study of carbon and silicon nanostructures for energy applications, Adv. Mater. 26 (46) (2014) 7786–7806, https://doi.org/10.1002/adma.201304507.

[24] L. Mino, G. Agostini, E. Borfecchia, D. Gianolio, A. Piovano, E. Gallo, C. Lamberti, Low-dimensional systems investigated by x-ray absorption spectroscopy: a selection of 2d, 1d and 0d cases, J. Phys. D Appl. Phys. 46 (42) (2013), 423001, https://doi.org/10.1088/0022-3727/46/42/423001.

[25] K. Novoselov, A. Geim, S. Morozov, D. Jiang, Y. Zhang, S. Dubonos, I. Grigorieva, A. Firsov, Electric field in atomically thin carbon films, Science 306 (2004) 666–669, https://doi.org/10.1126/science.1102896.

[26] S. Hagstrom, H.B. Lyon, G.A. Somorjai, Surface structures on the clean platinum (100) surface, Phys. Rev. Lett. 15 (1965) 491–493, https://doi.org/10.1103/physrevlett.15.491.

[27] H.B. Lyon, G.A. Somorjai, Low-energy electron-diffraction study of the clean (100), (111), and (110) faces of platinum, J. Chem. Phys. 46 (1967) 2539–2550, https://doi.org/10.1063/1.1841082.

[28] H. Ohtani, C.-T. Kao, M.V. Hove, G. Somorjai, A tabulation and classification of the structures of clean solid surfaces and of adsorbed atomic and molecular monolayers as determined from low energy electron diffraction patterns, Prog. Surf. Sci. 23 (1986) 155–316, https://doi.org/10.1016/0079-6816(86)90015-8.

[29] B. Nieuwenhuys, G. Somorjai, Dehydrogenation of cyclohexane and dehydrocyclization of n-heptane over single crystal surfaces of iridium, J. Catal. 46 (1977) 259–265, https://doi.org/10.1016/0021-9517(77)90208-1.

[30] R. Rosei, S. Modesti, F. Sette, C. Quaresima, A. Savoia, P. Perfetti, Electronic structure of carbidic and graphitic carbon on Ni(111), Phys. Rev. B 29 (1984) 3416–3422, https://doi.org/10.1103/physrevb.29.3416.

[31] A.Y. Tontegode, Carbon on transition metal surfaces, Prog. Surf. Sci. 38 (1991), 201429, https://doi.org/10.1016/0079-6816(91)90002-l.

[32] A. Morgan, G. Somorjai, Low energy electron diffraction studies of gas adsorption on the platinum (100) single crystal surface, Surf. Sci. 12 (1968) 405–425, https://doi.org/10.1016/0039-6028(68)90089-7.

[33] A. Nagashima, K. Nuka, K. Satoh, H. Itoh, T. Ichinokawa, C. Oshima, S. Otani, Electronic structure of monolayer graphite on some transition metal carbide surfaces, Surf. Sci. 287 (2002) 609–613, https://doi.org/10.1016/0039-6028(93)91037-P.

[34] M. Batzill, The surface science of graphene: metal interfaces, CVD synthesis, nanoribbons, chemical modifications, and defects, Surf. Sci. Rep. 67 (2012), 83115, https://doi.org/10.1016/j.surfrep.2011.12.001.

[35] J. Wintterlin, M.-L. Bocquet, Graphene on metal surfaces, Surf. Sci. 603 (2009) 1841–1852, https://doi.org/10.1016/j.susc.2008.08.037.

[36] C.-M. Seah, S.-P. Chai, A.R. Mohamed, Mechanisms of graphene growth by chemical vapour deposition on transition metals, Carbon 70 (2014) 1–21, https://doi.org/10.1016/j.carbon.2013.12.073.

[37] M. Yang, Y. Liu, T. Fan, D. Zhang, Metal-graphene interfaces in epitaxial and bulk systems: a review, Prog. Mater. Sci. 110 (2020), 100652, https://doi.org/10.1016/j.pmatsci.2020.100652.

[38] C.-M. Sung, M.-F. Tai, Reactivities of transition metals with carbon: implications to the mechanism of diamond synthesis under high pressure, Int. J. Refract. Metals Hard Mater. 15 (1997) 237–256, https://doi.org/10.1016/s0263-4368(97)00003-6.

[39] A. Dahal, M. Batzill, Graphene–nickel interfaces: a review, Nanoscale 6 (2014) 2548–2562, https://doi.org/10.1039/c3nr05279f.

[40] A. Preobrajenski, M. Ng, A. Vinogradov, N. Mårtensson, Controlling graphene corrugation on lattice-mismatched substrates, Phys. Rev. B 78 (2008), 073401, https://doi.org/10.1103/physrevb.78.073401.

[41] A. Dahal, R. Addou, H. Coy-Diaz, J. Lallo, M. Batzill, Charge doping of graphene in metal/graphene/dielectric sandwich structures evaluated by C-1s core level photoemission spectroscopy, Apl. Mater. 1 (2013), 042107, https://doi.org/10.1063/1.4824038.

[42] G. Otero, C. González, A.L. Pinardi, P. Merino, S. Gardonio, S. Lizzit, M. Blanco-Rey, K. Van de Ruit, C.F.J. Flipse, J. Méndez, P.L. de Andrés, J.A. Martín-Gago, Ordered vacancy network induced by the growth of epitaxial graphene on Pt (111), Phys. Rev. Lett. 105 (2010), 216102, https://doi.org/10.1103/physrevlett.105.216102.

[43] M. Gao, Y. Pan, L. Huang, H. Hu, L.Z. Zhang, H.M. Guo, S.X. Du, H.-J. Gao, Epitaxial growth and structural property of graphene on Pt(111), Appl. Phys. Lett. 98 (2011), 033101, https://doi.org/10.1063/1.3543624.

[44] J.-H. Gao, K. Sagisaka, M. Kitahara, M.-S. Xu, S. Miyamoto, D. Fujita, Graphene growth on a Pt(111) substrate by surface segregation and precipitation, Nanotechnology 23 (2012), 055704, https://doi.org/10.1088/0957-4484/23/5/055704.

[45] O. Endo, F. Matsui, W.-J. Chun, M. Nakamura, K. Amemiya, H. Ozaki, Nanographene growth from benzene on Pt(111), Surf. Sci. 711 (2021), 121874, https://doi.org/10.1016/j.susc.2021.121874.

[46] T. Fujita, W. Kobayashi, C. Oshima, Novel structures of carbon layers on a Pt(111) surface, Surf. Interface Anal. 37 (2005) 120–123, https://doi.org/10.1002/sia.1945.

[47] J. Sun, Y. Nam, N. Lindvall, M.T. Cole, K.B.K. Teo, Y. Woo Park, A. Yurgens, Growth mechanism of graphene on platinum: surface catalysis and carbon segregation, Appl. Phys. Lett. 104 (2014), 152107, https://doi.org/10.1063/1.4871978.

[48] P. Merino, M. Švec, A.L. Pinardi, G. Otero, J.A. Martín-Gago, Strain-driven moiré superstructures of epitaxial graphene on transition metal surfaces, ACS Nano 5 (2011) 5627–5634, https://doi.org/10.1021/nn201200j.

[49] S. Lizzit, A. Baraldi, High-resolution fast X-ray photoelectron spectroscopy study of ethylene interaction with Ir(111): from chemisorption to dissociation and graphene formation, Catal. Today 154 (2010) 6874, https://doi.org/10.1016/j.cattod.2010.05.028.

[50] H. Tetlow, J.P.d. Boer, I.J. Ford, D.D. Vvedensky, D. Curcio, L. Omiciuolo, S. Lizzit, A. Baraldi, L. Kantorovich, Ethylene decomposition on Ir(111): initial path to graphene formation, Phys. Chem. Chem. Phys. 18 (2016) 27897–27909, https://doi.org/10.1039/c6cp03638d.

[51] F. Presel, H. Tetlow, L. Bignardi, P. Lacovig, C.A. Tache, S. Lizzit, L. Kantorovich, A. Baraldi, Graphene growth by molecular beam epitaxy: an interplay between desorption, diffusion and intercalation of elemental C species on islands, Nanoscale 10 (2018) 7396–7406, https://doi.org/10.1039/c8nr00615f.

[52] D. Curcio, E. Sierda, M. Pozzo, L. Bignardi, L. Sbuelz, P. Lacovig, S. Lizzit, D. Alfè, A. Baraldi, Unusual reversibility in molecular break-up of PAHs: the case of pentacene dehydrogenation on Ir(111), Chem. Sci. 12 (2020) 170–178, https://doi.org/10.1039/d0sc03734f.

[53] J. Coraux, A.T.N. Diaye, C. Busse, T. Michely, Structural coherency of graphene on Ir(111), Nano Lett. 8 (2008), 565570, https://doi.org/10.1021/nl0728874.

[54] P. Lacovig, M. Pozzo, D. Alfè, P. Vilmercati, A. Baraldi, S. Lizzit, Growth of dome-shaped carbon nanoislands on Ir(111): the intermediate between carbidic clusters and quasi-free-standing graphene, Phys. Rev. Lett. 103 (2009), 166101, https://doi.org/10.1103/physrevlett.103.166101.

[55] J. Coraux, A.T. N'Diaye, M. Engler, C. Busse, D. Wall, N. Buckanie, F.-J.M. z. Heringdorf, R.v. Gastel, B. Poelsema, T. Michely, Growth of graphene on Ir (111), New J. Phys. 11 (2009) 3006, https://doi.org/10.1088/1367-2630/11/3/039801.

[56] E. Loginova, N.C. Bartelt, P.J. Feibelman, K.F. McCarty, Evidence for graphene growth by C cluster attachment, New J. Phys. 10 (2008), 093026, https://doi.org/10.1088/1367-2630/10/9/093026.

[57] H. Hattab, A.T. N'Diaye, D. Wall, G. Jnawali, J. Coraux, C. Busse, R. van Gastel, B. Poelsema, T. Michely, F.-J. Meyer zu Heringdorf, M. Horn-von Hoegen, Growth temperature dependent graphene alignment on ir(111), Appl. Phys. Lett. 98 (14) (2011), 141903, https://doi.org/10.1063/1.3548546.

[58] A.T. N'Diaye, J. Coraux, T.N. Plasa, C. Busse, T. Michely, Structure of epitaxial graphene on Ir(111), New J. Phys. 10 (2008), 043033, https://doi.org/10.1088/1367-2630/10/4/043033.

[59] I. Pletikosić, M. Kralj, P. Pervan, R. Brako, J. Coraux, A.T. N'Diaye, C. Busse, T. Michely, Dirac cones and minigaps for graphene on Ir(111), Phys. Rev. Lett. 102 (2009), 056808, https://doi.org/10.1103/physrevlett.102.056808.

[60] E. Starodub, A. Bostwick, L. Moreschini, S. Nie, F.E. Gabaly, K.F. McCarty, E. Rotenberg, In-plane orientation effects on the electronic structure, stability, and Raman scattering of monolayer graphene on Ir(111), Phys. Rev. B 83 (2011), 125428, https://doi.org/10.1103/physrevb.83.125428.

[61] M. Kralj, I. Pletikosić, M. Petrović, P. Pervan, M. Milun, A.T. N'Diaye, C. Busse, T. Michely, J. Fujii, I. Vobornik, Graphene on Ir(111) characterized by angle-resolved photoemission, Phys. Rev. B 84 (2011), 075427, https://doi.org/10.1103/physrevb.84.075427.

[62] S. Lizzit, G. Zampieri, L. Petaccia, R. Larciprete, P. Lacovig, E.D.L. Rienks, G. Bihlmayer, A. Baraldi, P. Hofmann, Band dispersion in the deep 1s core level of graphene, Nat. Phys. 6 (2010), 345349, https://doi.org/10.1038/nphys1615.

[63] A. Locatelli, G. Zamborlini, T.O. Menteş, Growth of single and multi-layer graphene on Ir(100), Carbon 74 (2014) 237–248, https://doi.org/10.1016/j.carbon.2014.03.028.

[64] S. Kraus, F. Huttmann, J. Fischer, T. Knispel, K. Bischof, A. Herman, M. Bianchi, R.-M. Stan, A.J. Holt, V. Caciuc, S. Tsukamoto, H. Wende, P. Hofmann, N. Atodiresei, T. Michely, Single-crystal graphene on Ir(110), Phys. Rev. B 105 (2022), 165405, https://doi.org/10.1103/physrevb.105.165405.

[65] L. Gao, J.R. Guest, N.P. Guisinger, Epitaxial graphene on Cu(111), Nano Lett. 10 (2010) 3512–3516, https://doi.org/10.1021/nl1016706.

[66] A.L. Walter, S. Nie, A. Bostwick, K.S. Kim, L. Moreschini, Y.J. Chang, D. Innocenti, K. Horn, K.F. McCarty, E. Rotenberg, Electronic structure of graphene on single-

crystal copper substrates, Phys. Rev. B 84 (2011), 195443, https://doi.org/10.1103/physrevb.84.195443.

[67] S. Gottardi, K. Müller, L. Bignardi, J.C. Moreno-López, T.A. Pham, O. Ivashenko, M. Yablonskikh, A. Barinov, J. Björk, P. Rudolf, M. Stöhr, Comparing graphene growth on Cu(111) versus oxidized Cu(111), Nano Lett. 15 (2015) 917–922, https://doi.org/10.1021/nl5036463.

[68] X. Li, W. Cai, J. An, S. Kim, J. Nah, D. Yang, R. Piner, A. Velamakanni, I. Jung, E. Tutuc, S.K. Banerjee, L. Colombo, R.S. Ruoff, Large-area synthesis of high-quality and uniform graphene films on copper foils, Science 324 (2009) 1312–1314, https://doi.org/10.1126/science.1171245.

[69] S. Chen, L. Brown, M. Levendorf, W. Cai, S.-Y. Ju, J. Edgeworth, X. Li, C. W. Magnuson, A. Velamakanni, R.D. Piner, J. Kang, J. Park, R.S. Ruoff, Oxidation resistance of graphene-coated Cu and Cu/Ni alloy, ACS Nano 5 (2011) 1321–1327, https://doi.org/10.1021/nn103028d.

[70] J.W. Suk, A. Kitt, C.W. Magnuson, Y. Hao, S. Ahmed, J. An, A.K. Swan, B. B. Goldberg, R.S. Ruoff, Transfer of CVD-grown monolayer graphene onto arbitrary substrates, ACS Nano 5 (2011) 6916–6924, https://doi.org/10.1021/nn201207c.

[71] C. Mattevi, H. Kim, M. Chhowalla, A review of chemical vapour deposition of graphene on copper, J. Mat. Chem. 21 (2011) 3324–3334, https://doi.org/10.1039/c0jm02126a.

[72] X. Li, L. Colombo, R.S. Ruoff, Synthesis of graphene films on copper foils by chemical vapor deposition, Adv. Mater. 28 (2016) 6247–6252, https://doi.org/10.1002/adma.201504760.

[73] B.-W. Li, D. Luo, L. Zhu, X. Zhang, S. Jin, M. Huang, F. Ding, R.S. Ruoff, Orientation-dependent strain relaxation and chemical functionalization of graphene on a Cu(111) foil, Adv. Mater. 30 (2018), 1706504, https://doi.org/10.1002/adma.201706504.

[74] P. Sutter, M.S. Hybertsen, J.T. Sadowski, E. Sutter, Electronic structure of few-layer epitaxial graphene on Ru(0001), Nano Lett. 9 (2009) 2654–2660, https://doi.org/10.1021/nl901040v.

[75] D.F. Johnson, W.H. Weinberg, Quantification of the influence of surface structure on C–H bond activation by iridium and platinum, Science 261 (1993) 76–78, https://doi.org/10.1126/science.261.5117.76.

[76] S. Nie, A.L. Walter, N.C. Bartelt, E. Starodub, A. Bostwick, E. Rotenberg, K. F. McCarty, Growth from below: graphene bilayers on Ir(111), ACS Nano 5 (2011) 2298–2306, https://doi.org/10.1021/nn103582g.

[77] S. hyon Phark, J. Borme, A.L. Vanegas, M. Corbetta, D. Sander, J. Kirschner, Scanning tunneling spectroscopy of epitaxial graphene nanoisland on Ir(111), Nanoscale Res. Lett. 7 (2012) 255, https://doi.org/10.1186/1556-276x-7-255.

[78] K.A. Simonov, N.A. Vinogradov, A.S. Vinogradov, A.V. Generalov, E. M. Zagrebina, G.I. Svirskiy, A.A. Cafolla, T. Carpy, J.P. Cunniffe, T. Taketsugu, A. Lyalin, N. Mårtensson, A.B. Preobrajenski, From graphene nanoribbons on Cu (111) to nanographene onPCu(110): critical role of substrate structure in the bottom-up fabrication strategy, ACS Nano 9 (9) (2015) 8997–9011, https://doi.org/10.1021/acsnano.5b03280.

[79] D. Curcio, L. Omiciuolo, M. Pozzo, P. Lacovig, S. Lizzit, N. Jabeen, L. Petaccia, D. Alfè, A. Baraldi, Molecular lifting, twisting, and curling during metal-assisted polycyclic hydrocarbon dehydrogenation, J. Am. Chem. Soc. 138 (2016) 3395–3402, https://doi.org/10.1021/jacs.5b12504.

[80] H. Tetlow, D. Curcio, A. Baraldi, L. Kantorovich, Hydrocarbon decomposition kinetics on the Ir(111) surface, Phys. Chem. Chem. Phys. 20 (9) (2017) 6083–6099, https://doi.org/10.1039/c7cp07526j.

[81] E.L. Shirley, L.J. Terminello, A. Santoni, F.J. Himpsel, Brillouin-zone-selection effects in graphite photoelectron angular distributions, Phys. Rev. B 51 (1995), 13614, https://doi.org/10.1103/physrevb.51.13614.

[82] J.-G. Ahn, J. Bang, J. Jung, Y. Kim, H. Lim, Scanning tunneling microscopic investigations for studying conformational change of underlying Cu(111) and ni (111) during graphene growth, Surf. Sci. 693 (2020), 121526, https://doi.org/10.1016/j.susc.2019.121526.

[83] S. Ullah, X. Yang, H.Q. Ta, M. Hasan, A. Bachmatiuk, K. Tokarska, B. Trzebicka, L. Fu, M.H. Rummeli, Graphene transfer methods: a review, Nano Res. 14 (2021) 3756–3772, https://doi.org/10.1007/s12274-021-3345-8.

[84] P.R. Kidambi, B.C. Bayer, R. Blume, Z.-J. Wang, C. Baehtz, R.S. Weatherup, M.-G. Willinger, R. Schloegl, S. Hofmann, Observing graphene grow: catalyst-graphene interactions during scalable graphene growth on polycrystalline copper, Nano Lett. 13 (2013) 4769–4778, https://doi.org/10.1021/nl4023572.

[85] A. Grüneis, K. Kummer, D.V. Vyalikh, Dynamics of graphene growth on a metal surface: a time-dependent photoemission study, New J. Phys. 11 (2009), 073050, https://doi.org/10.1088/1367-2630/11/7/073050.

[86] L.L. Patera, C. Africh, R.S. Weatherup, R. Blume, S. Bhardwaj, C. Castellarin-Cudia, A. Knop-Gericke, R. Schloegl, G. Comelli, S. Hofmann, C. Cepek, In situ observations of the atomistic mechanisms of Ni catalyzed low temperature graphene growth, ACS Nano 7 (2013) 7901–7912, https://doi.org/10.1021/nn402927q.

[87] J. Lahiri, T.S. Miller, A.J. Ross, L. Adamska, I.I. Oleynik, M. Batzill, Graphene growth and stability at nickel surfaces, New J. Phys. 13 (2011), 025001, https://doi.org/10.1088/1367-2630/13/2/025001.

[88] A. Politano, M. Cattelan, D.W. Boukhvalov, D. Campi, A. Cupolillo, S. Agnoli, N. G. Apostol, P. Lacovig, S. Lizzit, D. Farías, G. Chiarello, G. Granozzi, R. Larciprete, Unveiling the mechanisms leading to H_2 production promoted by water decomposition on epitaxial graphene at room temperature, ACS Nano 10 (2016) 4543–4549, https://doi.org/10.1021/acsnano.6b00554.

[89] K. Yuan, J.-Q. Zhong, S. Sun, Y. Ren, J.L. Zhang, W. Chen, Reactive intermediates or inert graphene? temperature- and pressure-determined evolution of carbon in

[90] L.L. Patera, F. Bianchini, C. Africh, C. Dri, G. Soldano, M.M. Mariscal, M. Peressi, G. Comelli, Real-time imaging of adatom-promoted graphene growth on nickel, Science 359 (2018) 1243–1246, https://doi.org/10.1126/science.aan8782.

[91] S.C. Matysik, C. Papp, A. Görling, Solving the puzzle of the coexistence of different adsorption geometries of graphene on Ni(111), J. Phys. Chem. C 122 (2018) 26105–26110, https://doi.org/10.1021/acs.jpcc.8b09438.

[92] G. Drera, C. Cepek, L.L. Patera, F. Bondino, E. Magnano, S. Nappini, C. Africh, A. Lodi-Rizzini, N. Joshi, P. Ghosh, A. Barla, S.K. Mahatha, S. Pagliara, A. Giampietri, C. Pintossi, L. Sangaletti, Identification of ni$_2$C electronic states in graphene-Ni(111) growth through resonant and dichroic angle-resolved photoemission at the C *k*-edge, Phys. Rev. B 96 (2017), 165442, https://doi.org/10.1103/PhysRevB.96.165442.

[93] L. Bignardi, P. Lacovig, M.M. Dalmiglio, F. Orlando, A. Ghafari, L. Petaccia, A. Baraldi, R. Larciprete, S. Lizzit, Key role of rotated domains in oxygen intercalation at graphene on Ni(111), 2D Mater. 4 (2017), 025106, https://doi.org/10.1088/2053-1583/aa702c.

[94] A. Varykhalov, J. Sánchez-Barriga, A. Shikin, C. Biswas, E. Vescovo, A. Rybkin, D. Marchenko, O. Rader, Electronic and magnetic properties of quasifreestanding graphene on Ni, Phys. Rev. Lett. 101 (2008), 157601, https://doi.org/10.1103/physrevlett.101.157601.

[95] A. Varykhalov, D. Marchenko, J. Sánchez-Barriga, M.R. Scholz, B. Verberck, B. Trauzettel, T.O. Wehling, C. Carbone, O. Rader, Intact Dirac cones at broken sublattice symmetry: photoemission study of graphene on ni and co, Phys. Rev. X 2 (2012), 041017, https://doi.org/10.1103/PhysRevX.2.041017.

[96] Y. Dedkov, E. Voloshina, Graphene growth and properties on metal substrates, J. Phys. Condens. Matter 27 (2015), 303002, https://doi.org/10.1088/0953-8984/27/30/303002.

[97] C. Africh, C. Cepek, L.L. Patera, G. Zamborlini, P. Genoni, T.O. Menteş, A. Sala, A. Locatelli, G. Comelli, Switchable graphene-substrate coupling through formation/dissolution of an intercalated Ni-carbide layer, Sci. Rep. 6 (2016), 19734, https://doi.org/10.1038/srep19734.

[98] W. Zhao, S. Kozlov, O. Höfert, K. Gotterbarm, M. Lorenz, F. Viñes, C. Papp, A. Görling, H.-P. Steinrück, Graphene on Ni(111): coexistence of different surface structures, J. Phys. Chem. Lett. 2 (2011) 759–764, https://doi.org/10.1021/jz200043p.

[99] C.J. Weststrate, A.C. Kızılkaya, E.T.R. Rossen, M.W.G.M. Verhoeven, I.M. Ciobîcǎ, A.M. Saib, J.W.H. Niemantsverdriet, Atomic and polymeric carbon on Co(0001): surface reconstruction, graphene formation, and catalyst poisoning electronically-similar Co surfaces, J. Phys. Chem. C 116 (2012) 11575–11583, https://doi.org/10.1021/jp301706q.

[100] D.Y. Usachov, K.A. Bokai, D.E. Marchenko, A.V. Fedorov, V.O. Shevelev, O. Y. Vilkov, E.Y. Kataev, L.V. Yashina, E. Rühl, C. Laubschat, D.V. Vyalikh, Cobalt-assisted recrystallization and alignment of pure and doped graphene, Nanoscale 10 (2018) 12123–12132, https://doi.org/10.1039/c8nr03183e.

[101] A. Varykhalov, O. Rader, Graphene grown on co(0001) films and islands: electronic structure and its precise magnetization dependence, Phys. Rev. B 80 (2009), 035437, 10.1103/PhysRevB.80.035437, https://link.aps.org/doi/10.1103/PhysRevB.80.035437.

[102] D. Usachov, A. Fedorov, M.M. Otrokov, A. Chikina, O. Vilkov, A. Petukhov, A. G. Rybkin, Y.M. Koroteev, E.V. Chulkov, V.K. Adamchuk, A. Grüneis, C. Laubschat, D.V. Vyalikh, Observation of single-spin Dirac fermions at the graphene/ferromagnet interface, Nano Lett. 15 (2015) 2396–2401, https://doi.org/10.1021/nl504693u.

[103] D.Y. Usachov, A.V. Fedorov, O.Y. Vilkov, A.E. Petukhov, A.G. Rybkin, A. Ernst, M. M. Otrokov, E.V. Chulkov, I.I. Ogorodnikov, M.V. Kuznetsov, L.V. Yashina, E. Y. Kataev, A.V. Erofeevskaya, V.Y. Voroshnin, V.K. Adamchuk, C. Laubschat, D. V. Vyalikh, Large-scale sublattice asymmetry in pure and boron-doped graphene, Nano Lett. 16 (2016) 4535–4543, https://doi.org/10.1021/acs.nanolett.6b01795.

[104] C.J.K.-J. Weststrate, D. Sharma, D.G. Rodriguez, M.A. Gleeson, H.O. A. Fredriksson, J.W.H. Niemantsverdriet, Mechanistic insight into carbon-carbon bond formation on cobalt under simulated Fischer-Tropsch synthesis conditions, Nat. Commun. 11 (2020) 750, https://doi.org/10.1038/s41467-020-14613-5.

[105] M. Jugovac, F. Genuzio, E.G. Lazo, N. Stojić, G. Zamborlini, V. Feyer, T.O. Menteş, A. Locatelli, C.M. Schneider, Role of carbon dissolution and recondensation in graphene epitaxial alignment on cobalt, Carbon 152 (2019) 489–496, https://doi.org/10.1016/j.carbon.2019.06.033.

[106] N.A. Vinogradov, A.A. Zakharov, V. Kocevski, J. Rusz, K.A. Simonov, O. Eriksson, A. Mikkelsen, E. Lundgren, A.S. Vinogradov, N. Mårtensson, A.B. Preobrajenski, Formation and structure of graphene waves on Fe(110), Phys. Rev. Lett. 109 (2012), 026101, https://doi.org/10.1103/physrevlett.109.026101.

[107] N. Vinogradov, K. Simonov, A. Generalov, J. Drnec, F. Carlà, A. Vinogradov, A. Preobrajenski, N. Mårtensson, R. Felici, The structural evolution of graphene/Fe(110) systems upon annealing, Carbon 111 (2017) 113–120, https://doi.org/10.1016/j.carbon.2016.09.058.

[108] E. Miniussi, M. Pozzo, T. Menteş, M. Niño, A. Locatelli, E. Vesselli, G. Comelli, S. Lizzit, D. Alfè, A. Baraldi, The competition for graphene formation on Re (0001): a complex interplay between carbon segregation, dissolution and carburisation, Carbon 73 (2014) 389–402, https://doi.org/10.1016/j.carbon.2014.02.081.

[109] Y. Qi, C. Meng, X. Xu, B. Deng, N. Han, M. Liu, M. Hong, Y. Ning, K. Liu, J. Zhao, Q. Fu, Y. Li, Y. Zhang, Z. Liu, Unique transformation from graphene to carbide on Re(0001) induced by strong carbon–metal interaction, J. Am. Chem. Soc. 139 (2017) 17574–17581, https://doi.org/10.1021/jacs.7b09755.

[110] E. Miniussi, M. Pozzo, A. Baraldi, E. Vesselli, R.R. Zhan, G. Comelli, T.O. Mentes, M.A. Niño, A. Locatelli, S. Lizzit, D. Alfè, Thermal stability of corrugated epitaxial graphene grown on Re(0001), Phys. Rev. Lett. 106 (2011), 216101, https://doi.org/10.1103/physrevlett.106.216101.

[111] D. Alfè, M. Pozzo, E. Miniussi, S. Günther, P. Lacovig, S. Lizzit, R. Larciprete, B. S. Burgos, T.O. Menteş, A. Locatelli, A. Baraldi, Fine tuning of graphene-metal adhesion by surface alloying, Sci. Rep. 3 (2013) 2430, https://doi.org/10.1038/srep02430.

[112] E. Loginova, N.C. Bartelt, P.J. Feibelman, K.F. McCarty, Factors influencing graphene growth on metal surfaces, New J. Phys. 11 (2009), 063046, https://doi.org/10.1088/1367-2630/11/6/063046.

[113] H. Chen, W. Zhu, Z. Zhang, Contrasting behavior of carbon nucleation in the initial stages of graphene epitaxial growth on stepped metal surfaces, Phys. Rev. Lett. 104 (2010), 186101, https://doi.org/10.1103/physrevlett.104.186101.

[114] S. Marchini, S. Günther, J. Wintterlin, Scanning tunneling microscopy of graphene on Ru(0001), Phys. Rev. B 76 (2007), 075429, https://doi.org/10.1103/physrevb.76.075429.

[115] C. Enderlein, Y.S. Kim, A. Bostwick, E. Rotenberg, K. Horn, The formation of an energy gap in graphene on ruthenium by controlling the interface, New J. Phys. 12 (2010), 033014, https://doi.org/10.1088/1367-2630/12/3/033014.

[116] J.J. Navarro, S. Leret, F. Calleja, D. Stradi, A. Black, R. Bernardo-Gavito, M. Garnica, D. Granados, A.L.V. de Parga, E.M. Pérez, R. Miranda, Organic covalent patterning of nanostructured graphene with selectivity at the atomic level, Nano Lett. 16 (2015) 355–361, https://doi.org/10.1021/acs.nanolett.5b03928.

[117] T. Brugger, S. Günther, B. Wang, J.H. Dil, M.-L. Bocquet, J. Osterwalder, J. Wintterlin, T. Greber, Comparison of electronic structure and template function of single-layer graphene and a hexagonal boron nitride nanomesh on Ru(0001), Phys. Rev. B 79 (2009), 045407, https://doi.org/10.1103/physrevb.79.045407.

[118] B. Borca, S. Barja, M. Garnica, M. Minniti, A. Politano, J.M. Rodriguez-García, J. J. Hinarejos, D. Farías, A.L.V. de Parga, R. Miranda, Electronic and geometric corrugation of periodically rippled, self-nanostructured graphene epitaxially grown on Ru(0001), New J. Phys. 12 (2010), 093018, https://doi.org/10.1088/1367-2630/12/9/093018.

[119] W. Moritz, B. Wang, M.-L. Bocquet, T. Brugger, T. Greber, J. Wintterlin, S. Günther, Structure determination of the coincidence phase of graphene on Ru (0001), Phys. Rev. Lett. 104 (2010), 136102, https://doi.org/10.1103/physrevlett.104.136102.

[120] Z. Zhou, B.F. Habenicht, Q. Guo, Z. Yan, Y. Xu, L. Liu, D.W. Goodman, Graphene moiré structure grown on a pseudomorphic metal overlayer supported on Ru (0001), Surf. Sci. 611 (2013) 67–73, https://doi.org/10.1016/j.susc.2013.01.016.

[121] E. Voloshina, Y. Dedkov, Atomic force spectroscopy and density-functional study of graphene corrugation on Ru(0001), Phys. Rev. B 93 (2016), 235418, https://doi.org/10.1103/physrevb.93.235418.

[122] C.C. Silva, M. Iannuzzi, D.A. Duncan, P.T.P. Ryan, K.T. Clarke, J.T. Küchle, J. Cai, W. Jolie, C. Schlueter, T.-L. Lee, C. Busse, Valleys and hills of graphene on Ru (0001), J. Phys. Chem. C 122 (2018) 18554–18561, https://doi.org/10.1021/acs.jpcc.8b05671.

[123] S.-Y. Kwon, C.V. Ciobanu, V. Petrova, V.B. Shenoy, J. Bareño, V. Gambin, I. Petrov, S. Kodambaka, Growth of semiconducting graphene on palladium, Nano Lett. 9 (2009) 3985–3990, https://doi.org/10.1021/nl902140j.

[124] H.S. Mok, A. Ebnonnasir, Y. Murata, S. Nie, K.F. McCarty, C.V. Ciobanu, S. Kodambaka, Kinetics of monolayer graphene growth by segregation on Pd (111), Appl. Phys. Lett. 104 (2014), 101606, https://doi.org/10.1063/1.4868386.

[125] K. Gotterbarm, W. Zhao, O. Höfert, C. Gleichweit, C. Papp, H.-P. Steinrück, Growth and oxidation of graphene on Rh(111), Phys. Chem. Chem. Phys. 15 (2013) 19625–19631, https://doi.org/10.1039/c3cp53802h.

[126] R.S. Weatherup, B.C. Bayer, R. Blume, C. Baehtz, P.R. Kidambi, M. Fouquet, C. T. Wirth, R. Schlögl, S. Hofmann, On the mechanisms of Ni-catalysed graphene chemical vapour deposition, ChemPhysChem 13 (2012) 2544–2549, https://doi.org/10.1002/cphc.201101020.

[127] C. Weststrate, J. Niemantsverdriet, CO as a promoting spectator species of C_xH_y conversions relevant for fischer–tropsch chain growth on cobalt: evidence from temperature-programmed reaction and reflection absorption infrared spectroscopy, ACS Catal. 8 (2018) 10826–10835, https://doi.org/10.1021/acscatal.8b02743.

[128] C.J. Weststrate, I.M. Ciobîcă, J. van de Loosdrecht, J.W. Niemantsverdriet, Adsorption and decomposition of ethene and propene on Co(0001): the surface chemistry of Fischer-Tropsch chain growth intermediates, J. Phys. Chem. C 120 (2016) 29210–29224, https://doi.org/10.1021/acs.jpcc.6b09760.

[129] B. Wang, M.-L. Bocquet, S. Marchini, S. Günther, J. Wintterlin, Chemical origin of a graphene moiré overlayer on Ru(0001), Phys. Chem. Chem. Phys. 10 (2008) 3530–3534, https://doi.org/10.1039/b801785a.

[130] H. Zhang, Q. Fu, Y. Cui, D. Tan, X. Bao, Growth mechanism of graphene on Ru (0001) and O$_2$ adsorption on the graphene/Ru(0001) surface, J. Phys. Chem. C 113 (2009) 8296–8301, https://doi.org/10.1021/jp810514u.

[131] U. Starke, S. Forti, K. Emtsev, C. Coletti, Engineering the electronic structure of epitaxial graphene by transfer doping and atomic intercalation, MRS Bull. 37 (2012) 1177–1186, https://doi.org/10.1557/mrs.2012.272.

[132] M. Ruan, Y. Hu, Z. Guo, R. Dong, J. Palmer, J. Hankinson, C. Berger, W.A. de Heer, Epitaxial graphene on silicon carbide: introduction to structured graphene, MRS Bull. 37 (2012) 1138–1147, https://doi.org/10.1557/mrs.2012.231.

[133] C. Riedl, U. Starke, J. Bernhardt, M. Franke, K. Heinz, Structural properties of the graphene-SiC(0001) interface as a key for the preparation of homogeneous large-terrace graphene surfaces, Phys. Rev. B 76 (2007), 245406, https://doi.org/10.1103/physrevb.76.245406.

[134] C. Riedl, C. Coletti, U. Starke, Structural and electronic properties of epitaxial graphene on SiC(0001): a review of growth, characterization, transfer doping and hydrogen intercalation, J. Phys. D Appl. Phys. 43 (2010), 374009, https://doi.org/10.1088/0022-3727/43/37/374009.

[135] K.V. Emtsev, F. Speck, T. Seyller, L. Ley, J.D. Riley, Interaction, growth, and ordering of epitaxial graphene on SiC{0001} surfaces: a comparative photoelectron spectroscopy study, Phys. Rev. B 77 (2008), 155303, https://doi.org/10.1103/PhysRevB.77.155303.

[136] K.V. Emtsev, A. Bostwick, K. Horn, J. Jobst, G.L. Kellogg, L. Ley, J.L. McChesney, T. Ohta, S.A. Reshanov, J. Röhrl, E. Rotenberg, A.K. Schmid, D. Waldmann, H. B. Weber, T. Seyller, Towards wafer-size graphene layers by atmospheric pressure graphitization of silicon carbide, Nat. Mater. 8 (2009) 203–207, https://doi.org/10.1038/nmat2382.

[137] U. Starke, C. Riedl, Epitaxial graphene on SiC(0001) and $\mathrm{SiC}(000\bar{1})$: from surface reconstructions to carbon electronics, J. Phys. Condens. Matter 21 (2009), 134016, https://doi.org/10.1088/0953-8984/21/13/134016.

[138] I. Forbeaux, J.-M. Themlin, J.-M. Debever, Heteroepitaxial graphite on 6H-SiC (0001): interface formation through conduction-band electronic structure, Phys. Rev. B 58 (1998) 16396–16406, https://doi.org/10.1103/PhysRevB.58.16396.

[139] W.A. de Heer, C. Berger, X. Wu, P.N. First, E.H. Conrad, X. Li, T. Li, M. Sprinkle, J. Hass, M.L. Sadowski, M. Potemski, G. Martinez, Epitaxial graphene, Solid State Commun. 143 (2007) 92–100, https://doi.org/10.1016/j.ssc.2007.04.023.

[140] L. Daukiya, M. Nair, M. Cranney, F. Vonau, S. Hajjar-Garreau, D. Aubel, L. Simon, Functionalization of 2D materials by intercalation, Prog. Surf. Sci. 94 (2018) 1–20, https://doi.org/10.1016/j.progsurf.2018.07.001.

[141] S. Wu, Q. Zhang, H. Yang, Y. Ma, T. Zhang, L. Liu, H.-J. Gao, Y. Wang, Advances in two-dimensional heterostructures by mono-element intercalation underneath epitaxial graphene, Prog. Surf. Sci. 96 (2021), 100637, https://doi.org/10.1016/j.progsurf.2021.100637.

[142] M. Bazarnik, J. Brede, R. Decker, R. Wiesendanger, Tailoring molecular self-assembly of magnetic phthalocyanine molecules on Fe-and Co-intercalated graphene, ACS Nano 7 (2013) 11341–11349, https://doi.org/10.1021/nn405172q.

[143] G. Li, H. Zhou, L. Pan, Y. Zhang, L. Huang, W. Xu, S. Du, M. Ouyang, A.C. Ferrari, H.-J. Gao, Role of cooperative interactions in the intercalation of heteroatoms between graphene and a metal substrate, J. Am. Chem. Soc. 137 (2015) 7099–7103, https://doi.org/10.1021/ja5113657.

[144] M. Sicot, D. Tristant, I.C. Gerber, B. Kierren, F. Chérioux, Y. Fagot-Revurat, L. Moreau, J. Granet, D. Malterre, Polymorphism of two-dimensional halogen bonded supramolecular networks on a graphene/iridium(111) surface, J. Phys. Chem. C 121 (2017) 2201–2210, https://doi.org/10.1021/acs.jpcc.6b09892.

[145] A. Kumar, K. Banerjee, P. Liljeroth, Molecular assembly on two-dimensional materials, Acs Sym Ser 28 (2017), 082001, https://doi.org/10.1088/1361-6528/aa564f.

[146] G. Avvisati, C. Cardoso, D. Varsano, A. Ferretti, P. Gargiani, M.G. Betti, Ferromagnetic and antiferromagnetic coupling of spin molecular interfaces with high thermal stability, Nano Lett. 18 (2018) 2268–2273, https://doi.org/10.1021/acs.nanolett.7b04836.

[147] G. Avvisati, P. Gargiani, P. Mondelli, F. Presel, L. Bignardi, A. Baraldi, M.G. Betti, Metal phthalocyanines interaction with Co mediated by a moiré graphene superlattice, J. Chem. Phys. 150 (2019), 054704, https://doi.org/10.1063/1.5080533.

[148] A. Calloni, G. Bussetti, G. Avvisati, M.S. Jagadeesh, D. Pacilè, A. Ferretti, D. Varsano, C. Cardoso, L. Duò, F. Ciccacci, M.G. Betti, Empty electron states in cobalt-intercalated graphene, J. Chem. Phys. 153 (2020), 214703, https://doi.org/10.1063/5.0021814.

[149] R. Mu, Q. Fu, L. Jin, L. Yu, G. Fang, D. Tan, X. Bao, Visualizing chemical reactions confined under graphene, Angew. Chem. Int. Ed. 51 (2012) 4856–4859, https://doi.org/10.1002/ange.201200413.

[150] A. Picone, A. Lodesani, M. Capra, A. Brambilla, F. Bottegoni, M. Jugovac, A. K. Kundu, P. Sheverdyaeva, P. Moras, From Cr carbide to Cr oxide through a graphene layer, Appl. Surf. Sci. 599 (2022), 153926, https://doi.org/10.1016/j.apsusc.2022.153926.

[151] R. Decker, J. Brede, N. Atodiresei, V. Caciuc, S. Blügel, R. Wiesendanger, Atomic-scale magnetism of cobalt-intercalated graphene, Phys. Rev. B 87 (2013), 041403, https://doi.org/10.1103/physrevb.87.041403.

[152] H. Vita, P. Leicht, K. Horn, A. Shick, F. Máca, et al., Electronic structure and magnetic properties of cobalt intercalated in graphene on Ir(111), Phys. Rev. B 90 (2014), 165432, https://doi.org/10.1103/physrevb.90.165432.

[153] F. Presel, N. Jabeen, M. Pozzo, D. Curcio, L. Omiciuolo, P. Lacovig, S. Lizzit, D. Alfè, A. Baraldi, Unravelling the roles of surface chemical composition and geometry for the graphene–metal interaction through C1s core-level spectroscopy, Carbon 93 (2015) 187–198, https://doi.org/10.1016/j.carbon.2015.05.041.

[154] M. Cattelan, G.W. Peng, E. Cavaliere, L. Artiglia, A. Barinov, L.T. Roling, M. Favaro, I. Píš, S. Nappini, E. Magnano, F. Bondino, L. Gavioli, S. Agnoli, M. Mavrikakis, G. Granozzi, The nature of the Fe–graphene interface at the nanometer level, Nanoscale 7 (2015) 2450–2460, https://doi.org/10.1063/1.4952924.

[155] A. Dahal, M. Batzill, Growth from behind: intercalation-growth of two-dimensional FeO moiré structure underneath of metal-supported graphene, Sci. Rep. 5 (2015), 11378, https://doi.org/10.1038/srep11378.

[156] R.C. de Campos Ferreira, L.H. de Lima, L. Barreto, C.C. Silva, R. Landers, A. de Siervo, Unraveling the atomic structure of Fe intercalated under graphene on Ir

(111): a multitechnique approach, Chem. Mater. 30 (2018) 7201–7210, https://doi.org/10.1021/acs.chemmater.8b03186.

[157] P. Zhao, P. Ren, C.J.K.-J. Weststrate, X. Yu, D.-B. Cao, H. Xiang, J. Xu, Y. Yang, Y.-W. Li, J.W.H. Niemantsverdriet, X. Wen, X. Yu, Intercalation mechanisms of Fe atoms underneath a graphene monolayer on Ru(0001), J. Phys. Chem. C 122 (2018) 22903–22910, https://doi.org/10.1021/acs.jpcc.8b05370.

[158] I. Píš, S. Nappini, F. Bondino, T.O. Menteş, A. Sala, A. Locatelli, E. Magnano, Fe intercalation under graphene and hexagonal boron nitride in-plane heterostructure on Pt(111), Carbon 134 (2018) 274–282, https://doi.org/10.1016/j.carbon.2018.03.086.

[159] P. Rosenzweig, U. Starke, Large-area synthesis of a semiconducting silver monolayer via intercalation of epitaxial graphene, Phys. Rev. B 101 (2020), 201407, https://doi.org/10.1103/physrevb.101.201407.

[160] S. Forti, A. Stöhr, A.A. Zakharov, C. Coletti, K.V. Emtsev, U. Starke, Mini-Dirac cones in the band structure of a copper intercalated epitaxial graphene superlattice, 2D Mater. 3 (2016), 035003, https://doi.org/10.1088/2053-1583/3/3/035003.

[161] L. Jin, Q. Fu, Y. Yang, X. Bao, A comparative study of intercalation mechanism at graphene/Ru(0001) interface, Surf. Sci. 617 (2013) 81–86, https://doi.org/10.1016/j.susc.2013.07.008.

[162] I.I. Klimovskikh, M.M. Otrokov, V.Y. Voroshnin, D. Sostina, L. Petaccia, G. D. Santo, S. Thakur, E.V. Chulkov, A.M. Shikin, Spin–orbit coupling induced gap in graphene on Pt(111) with intercalated Pb monolayer, ACS Nano 11 (2017) 368–374, https://doi.org/10.1021/acsnano.6b05982.

[163] S. Chen, P.A. Thiel, E. Conrad, M.C. Tringides, Growth and stability of Pb intercalated phases under graphene on SiC, Phys. Rev. Mater. 4 (2020), 124005, https://doi.org/10.1103/physrevmaterials.4.124005.

[164] M. Petrović, I.Š. Rakić, S. Runte, C. Busse, J. Sadowski, P. Lazić, I. Pletikosić, Z.-H. Pan, M. Milun, P. Pervan, et al., The mechanism of cesium intercalation of graphene, Nat. Commun. 4 (2013) 1–8, https://doi.org/10.1038/ncomms3772.

[165] A.V. Fedorov, N.I. Verbitskiy, D. Haberer, C. Struzzi, L. Petaccia, D. Usachov, O. Y. Vilkov, D.V. Vyalikh, J. Fink, M. Knupfer, B. Büchner, A. Grüneis, Observation of a universal donor-dependent vibrational mode in graphene, Nat. Commun. 5 (2014) 3257, https://doi.org/10.1038/ncomms4257.

[166] P. Pervan, P. Lazić, M. Petrović, I.Š. Rakić, I. Pletikosić, M. Kralj, M. Milun, T. Valla, Li adsorption versus graphene intercalation on Ir(111): from quenching to restoration of the Ir surface state, Phys. Rev. B 92 (2015), 245415, https://doi.org/10.1103/physrevb.92.245415.

[167] C.C. Silva, J. Cai, W. Jolie, D. Dombrowski, F.H.F. zum Hagen, A.J. Martínez-Galera, C. Schlueter, T.-L. Lee, C. Busse, Lifting epitaxial graphene by intercalation of alkali metals, J. Phys. Chem. C 123 (2019) 13712–13719, https://doi.org/10.1021/acs.jpcc.9b02442.

[168] U.A. Schröder, M. Petrović, T. Gerber, A.J. Martínez-Galera, E. Grånäs, M. A. Arman, C. Herbig, J. Schnadt, M. Kralj, J. Knudsen, T. Michely, Core level shifts of intercalated graphene, 2D Mater. 4 (2016), 015013, https://doi.org/10.1088/2053-1583/4/1/015013.

[169] S. Schumacher, F. Huttmann, M. Petrović, C. Witt, D.F. Förster, C. Vo-Van, J. Coraux, A.J. Martínez-Galera, V. Sessi, I. Vergara, et al., Europium underneath graphene on Ir(111): intercalation mechanism, magnetism, and band structure, Phys. Rev. B 90 (2014), 235437, https://doi.org/10.1103/physrevb.90.235437.

[170] S. Link, S. Forti, A. Stöhr, K. Küster, M. Rösner, D. Hirschmeier, C. Chen, J. Avila, M. Asensio, A. Zakharov, et al., Introducing strong correlation effects into graphene by gadolinium intercalation, Phys. Rev. B 100 (2019), 121407, https://doi.org/10.1103/physrevb.100.121407.

[171] L. Daukiya, M.N. Nair, S. Hajjar-Garreau, F. Vonau, D. Aubel, J.L. Bubendorff, M. Cranney, E. Denys, A. Florentin, G. Reiter, L. Simon, Highly n-doped graphene generated through intercalated terbium atoms, Phys. Rev. B 97 (2018), 035309, https://doi.org/10.1103/PhysRevB.97.035309.

[172] I. Klimovskikh, M. Krivenkov, A. Varykhalov, D. Estyunin, A. Shikin, Reconstructed fermi surface in graphene on Ir(111) by Gd-Ir surface alloying, Carbon 147 (2019) 182–186, https://doi.org/10.1016/j.carbon.2019.02.037.

[173] N.A. Anderson, M. Hupalo, D. Keavney, M. Tringides, D. Vaknin, Intercalated rare-earth metals under graphene on SiC, J. Magn. Magn Mater. 474 (2019) 666–670, https://doi.org/10.1016/j.jmmm.2018.11.007.

[174] E. Voloshina, A. Generalov, M. Weser, S. Böttcher, K. Horn, Y.S. Dedkov, Structural and electronic properties of the graphene/Al/Ni(111) intercalation system, New J. Phys. 13 (2011) 113028, https://doi.org/10.1088/1367-2630/13/11/113028.

[175] M. Weser, E.N. Voloshina, K. Horn, Y.S. Dedkov, Electronic structure and magnetic properties of the Graphene/Fe/Ni(111) intercalation-like system, Phys. Chem. Chem. Phys. 13 (2011) 7534, https://doi.org/10.1039/c1cp00014d.

[176] N. Ligato, A. Cupolillo, L. Caputi, Study of the intercalation of graphene on Ni (111) with Cs atoms: towards the quasi-free graphene, Thin Solid Films 543 (2013) 59–62, https://doi.org/10.1016/j.tsf.2013.02.121.

[177] S. Günther, T. Menteş, R. Reichelt, E. Miniussi, B. Santos, A. Baraldi, A. Locatelli, Au intercalation under epitaxial graphene on Ru(0001): the role of graphene edges, Carbon 162 (2020) 292–299, https://doi.org/10.1016/j.carbon.2020.02.025.

[178] O. Vilkov, A. Fedorov, D. Usachov, L.V. Yashina, A.V. Generalov, K. Borygina, N. I. Verbitskiy, A. Grüneis, D.V. Vyalikh, Controlled assembly of graphene-capped nickel, cobalt and iron silicides, Sci. Rep. 3 (2013) 2168, https://doi.org/10.1038/srep02168.

[179] J. Brede, J. Sławińska, M. Abadia, C. Rogero, J.E. Ortega, I. Piquero-Zulaica, J. Lobo-Checa, A. Arnau, J.I. Cerdá, Tuning the graphene on Ir(111) adsorption regime by Fe/Ir surface-alloying, 2D Mater. 4 (2016), 015016, https://doi.org/10.1088/2053-1583/4/1/015016.

[180] A. Rybkina, A. Rybkin, A. Fedorov, D. Usachov, M. Yachmenev, D. Marchenko, O. Vilkov, A. Nelyubov, V. Adamchuk, A. Shikin, Interaction of graphene with intercalated Al: the process of intercalation and specific features of the electronic structure of the system, Surf. Sci. 609 (2013) 7–17, https://doi.org/10.1016/j.susc.2012.08.022.

[181] R. Addou, A. Dahal, M. Batzill, Graphene on ordered Ni-alloy surfaces formed by metal (Sn, Al) intercalation between graphene/Ni(111), Surf. Sci. 606 (2012) 1108–1112, https://doi.org/10.1016/j.susc.2012.03.009.

[182] J. Drnec, S. Vlaic, I. Carlomagno, C.J. Gonzalez, H. Isern, F. Carlà, R. Fiala, N. Rougemaille, J. Coraux, R. Felici, Surface alloying upon co intercalation between graphene and Ir(111), Carbon 94 (2015) 554–559, https://doi.org/10.1016/j.carbon.2015.07.039.

[183] S. Oida, F. McFeely, J. Hannon, R. Tromp, M. Copel, Z. Chen, Y. Sun, D. Farmer, J. Yurkas, Decoupling graphene from SiC(0001) via oxidation, Phys. Rev. B 82 (2010), 041411, https://doi.org/10.1103/physrevb.82.041411.

[184] R. Larciprete, S. Ulstrup, P. Lacovig, M. Dalmiglio, M. Bianchi, F. Mazzola, L. Hornekær, F. Orlando, A. Baraldi, P. Hofmann, S. Lizzit, Oxygen switching of the epitaxial graphene–metal interaction, ACS Nano 6 (2012) 9551–9558, https://doi.org/10.1021/nn302729j.

[185] E. Grånäs, J. Knudsen, U.A. Schröder, T. Gerber, C. Busse, M.A. Arman, K. Schulte, J.N. Andersen, T. Michely, Oxygen intercalation under graphene on Ir(111): energetics, kinetics, and the role of graphene edges, ACS Nano 6 (2012) 9951–9963, https://doi.org/10.1021/nn303548z.

[186] P. Sutter, J.T. Sadowski, E.A. Sutter, Chemistry under cover: tuning metal-graphene interaction by reactive intercalation, J. Am. Chem. Soc. 132 (2010) 8175–8179, https://doi.org/10.1021/ja102398n.

[187] P. Sutter, P. Albrecht, X. Tong, E. Sutter, Mechanical decoupling of graphene from Ru(0001) by interfacial reaction with oxygen, J. Phys. Chem. C 117 (2013) 6320–6324, https://doi.org/10.1021/jp400838j.

[188] R. Blume, P.R. Kidambi, B.C. Bayer, R.S. Weatherup, Z.-J. Wang, G. Weinberg, M.-G. Willinger, M. Greiner, S. Hofmann, A. Knop-Gericke, R. Schlögl, The influence of intercalated oxygen on the properties of graphene on polycrystalline Cu under various environmental conditions, Phys. Chem. Chem. Phys. 16 (2014) 25989–26003, https://doi.org/10.1039/c4cp04025b.

[189] L. Omiciuolo, E.R. Hernández, E. Miniussi, F. Orlando, P. Lacovig, S. Lizzit, T. O. Menteş, A. Locatelli, R. Larciprete, M. Bianchi, S. Ulstrup, P. Hofmann, D. Alfè, A. Baraldi, Bottom-up approach for the low-cost synthesis of graphene-alumina nanosheet interfaces using bimetallic alloys, Nat. Commun. 5 (2014) 5062, https://doi.org/10.1038/ncomms6062.

[190] Y. Dedkov, W. Klesse, A. Becker, F. Späth, C. Papp, E. Voloshina, Decoupling of graphene from Ni(111) via formation of an interfacial NiO layer, Carbon 121 (2017) 10–16, https://doi.org/10.1016/j.carbon.2017.05.068.

[191] S. Ulstrup, P. Lacovig, F. Orlando, D. Lizzit, L. Bignardi, M. Dalmiglio, M. Bianchi, F. Mazzola, A. Baraldi, R. Larciprete, et al., Photoemission investigation of oxygen intercalated epitaxial graphene on Ru(0001), Surf. Sci. 678 (2018) 57–64, https://doi.org/10.1016/j.susc.2018.03.017.

[192] K.A. Bokai, V.O. Shevelev, D. Marchenko, A.A. Makarova, V.Y. Mikhailovskii, A. A. Zakharov, O.Y. Vilkov, M. Krivenkov, D.V. Vyalikh, D.Y. Usachov, Visualization of graphene grain boundaries through oxygen intercalation, Appl. Surf. Sci. (2021) 150476doi, https://doi.org/10.1016/j.apsusc.2021.150476.

[193] E. Grånäs, M. Andersen, M.A. Arman, T. Gerber, B. Hammer, J. Schnadt, J. N. Andersen, T. Michely, J. Knudsen, CO intercalation of graphene on Ir(111) in the millibar regime, J. Phys. Chem. C 117 (2013) 16438–16447, https://doi.org/10.1021/jp4043045.

[194] D.A. Leon, A. Ferretti, D. Varsano, E. Molinari, C. Cardoso, Graphene decoupling through oxygen intercalation on Gr/Co and Gr/Co/Ir interfaces, Phys Rev Mater 6 (2022), 064004, https://doi.org/10.1103/physrevmaterials.6.064004.

[195] S.D. Puppo, V. Carnevali, D. Perilli, F. Zarabara, A.L. Rizzini, G. Fornasier, E. Zupanič, S. Fiori, L.L. Patera, M. Panighel, S. Bhardwaj, Z. Zou, G. Comelli, C. Africh, C. Cepek, C.D. Valentin, M. Peressi, Tuning graphene doping by carbon monoxide intercalation at the Ni(111) interface, Carbon 176 (2021) 253–261, https://doi.org/10.1016/j.carbon.2021.01.120.

[196] C. Riedl, C. Coletti, T. Iwasaki, A.A. Zakharov, U. Starke, Quasi-free-standing epitaxial graphene on SiC obtained by hydrogen intercalation, Phys. Rev. Lett. 103 (2009), 246804, https://doi.org/10.1103/physrevlett.103.246804.

[197] S. Forti, K.V. Emtsev, C. Coletti, A.A. Zakharov, C. Riedl, U. Starke, Large-area homogeneous quasifree standing epitaxial graphene on SiC(0001): electronic and structural characterization, Phys. Rev. B 84 (2011), 125449, https://doi.org/10.1103/physrevb.84.125449.

[198] S. Ulstrup, M. Andersen, M. Bianchi, L. Barreto, B. Hammer, L. Hornekær, P. Hofmann, Sequential oxygen and alkali intercalation of epitaxial graphene on Ir(111): enhanced many-body effects and formation of pn -interfaces, 2D Mater. 1 (2014), 025002, https://doi.org/10.1088/2053-1583/1/2/025002.

[199] S. Lizzit, R. Larciprete, P. Lacovig, M. Dalmiglio, F. Orlando, A. Baraldi, L. Gammelgaard, L. Barreto, M. Bianchi, E. Perkins, et al., Transfer-free electrical insulation of epitaxial graphene from its metal substrate, Nano Lett. 12 (2012) 4503 4507, https://doi.org/10.1021/nl301614j.

[200] U.A. Schröder, E. Grånäs, T. Gerber, M.A. Arman, A.J. Martínez-Galera, K. Schulte, J.N. Andersen, J. Knudsen, T. Michely, Etching of graphene on Ir(111) with molecular oxygen, Carbon 96 (2016) 320–331, https://doi.org/10.1016/j.carbon.2015.09.063.

[201] A.C. Ferrari, F. Bonaccorso, V. Fal'ko, K.S. Novoselov, S. Roche, P. Bøggild, S. Borini, F.H.L. Koppens, V. Palermo, N. Pugno, J.A. Garrido, R. Sordan, A. Bianco, L. Ballerini, M. Prato, E. Lidorikis, J. Kivioja, C. Marinelli, T. Ryhänen, A. Morpurgo, J.N. Coleman, V. Nicolosi, L. Colombo, A. Fert, M. Garcia-Hernandez, A. Bachtold, G.F. Schneider, F. Guinea, C. Dekker, M. Barbone, Z. Sun,

C. Galiotis, A.N. Grigorenko, G. Konstantatos, A. Kis, M. Katsnelson, L. Vandersypen, A. Loiseau, V. Morandi, D. Neumaier, E. Treossi, V. Pellegrini, M. Polini, A. Tredicucci, G.M. Williams, B.H. Hong, J.-H. Ahn, J.M. Kim, H. Zirath, B.J. van Wees, H. van der Zant, L. Occhipinti, A.D. Matteo, I.A. Kinloch, T. Seyller, E. Quesnel, X. Feng, K. Teo, N. Rupesinghe, P. Hakonen, S.R.T. Neil, Q. Tannock, T. Löfwander, J. Kinaret, Science and technology roadmap for graphene, related two-dimensional crystals, and hybrid systems, Nanoscale 7 (2015) 4598–4810, https://doi.org/10.1039/c4nr01600a.

[202] H.-J. Freund, G. Pacchioni, Oxide ultra-thin films on metals: new materials for the design of supported metal catalysts, Chem. Soc. Rev. 37 (2008) 2224, https://doi.org/10.1039/b718768h.

[203] R. Larciprete, P. Lacovig, F. Orlando, M. Dalmiglio, L. Omiciuolo, A. Baraldi, S. Lizzit, Chemical gating of epitaxial graphene through ultrathin oxide layers, Nanoscale 7 (2015) 12650–12658, https://doi.org/10.1039/c5nr02936h.

[204] Y. Ma, E. Travaglia, H. Bana, L. Bignardi, P. Lacovig, S. Lizzit, M. Batzill, Periodic modulation of graphene by a 2D-FeO/Ir(111) moiré interlayer, J. Phys. Chem. C 121 (2017) 2762 2770, https://doi.org/10.1021/acs.jpcc.6b11112.

[205] D.D. Angelis, F. Presel, N. Jabeen, L. Bignardi, D. Lizzit, P. Lacovig, S. Lizzit, T. Montini, P. Fornasiero, D. Alfè, A. Baraldi, Interfacial two-dimensional oxide enhances photocatalytic activity of graphene/titania via electronic structure modification, Carbon 157 (2020) 350–357, https://doi.org/10.1016/j.carbon.2019.10.053.

[206] U. Diebold, The surface science of titanium dioxide, Surf. Sci. Rep. 48 (2003) 53–229, https://doi.org/10.1016/s0167-5729(02)00100-0.

[207] N. Briggs, S. Subramanian, Z. Lin, X. Li, X. Zhang, K. Zhang, K. Xiao, D. Geohegan, R. Wallace, L.-Q. Chen, M. Terrones, A. Ebrahimi, S. Das, J. Redwing, C. Hinkle, K. Momeni, A.v. Duin, V. Crespi, S. Kar, J.A. Robinson, A roadmap for electronic grade 2D materials, 2D Mater. 6 (2019) 022001, https://doi.org/10.1088/2053-1583/aaf836.

[208] W. Zhou, J. Jia, J. Lu, L. Yang, D. Hou, G. Li, S. Chen, Recent developments of carbon-based electrocatalysts for hydrogen evolution reaction, Nano 28 (2016) 29–43, https://doi.org/10.1016/j.nanoen.2016.08.027.

[209] A. Lodesani, A. Picone, A. Brambilla, D. Giannotti, M.S. Jagadeesh, A. Calloni, G. Bussetti, G. Berti, M. Zani, M. Finazzi, L. Duò, F. Ciccacci, Graphene as an ideal buffer layer for the growth of high-quality ultrathin Cr₂O₃ layers on Ni(111), ACS Nano 13 (2019) 4361–4367, https://doi.org/10.1021/acsnano.8b09588.

[210] G. Giovannetti, P.A. Khomyakov, G. Brocks, V.M. Karpan, J.v. d. Brink, P.J. Kelly, Doping graphene with metal contacts, Phys. Rev. Lett. 101 (2008), 026803, https://doi.org/10.1103/physrevlett.101.026803.

[211] P.A. Khomyakov, G. Giovannetti, P.C. Rusu, G. Brocks, J.v. d. Brink, P.J. Kelly, First-principles study of the interaction and charge transfer between graphene and metals, Phys. Rev. B 79 (2009), 195425, https://doi.org/10.1103/physrevb.79.195425.

[212] A.L. Torre, F.B. Romdhane, W. Baaziz, I. Janowska, C. Pham-Huu, S. Begin-Colin, G. Pourroy, F. Banhart, Formation and characterization of graphene-metal nano-contacts, Carbon 77 (2014) 906–911, https://doi.org/10.1016/j.carbon.2014.06.004.

[213] A. Grüneis, Synthesis and electronic properties of chemically functionalized graphene on metal surfaces, J. Phys. Condens. Matter 25 (2013), 043001, https://doi.org/10.1088/0953-8984/25/4/043001.

[214] L.G. Bulusheva, M.A. Kanygin, V.E. Arkhipov, K.M. Popov, Y.V. Fedoseeva, D. A. Smirnov, A.V. Okotrub, In situ x-ray photoelectron spectroscopy study of lithium interaction with graphene and nitrogen-doped graphene films produced by chemical vapor deposition, J. Phys. Chem. C 121 (2017) 5108–5114, https://doi.org/10.1021/acs.jpcc.6b12687.

[215] B. Huang, H. Xiang, Q. Xu, S.-H. Wei, Overcoming the phase inhomogeneity in chemically functionalized graphene: the case of graphene oxides, Phys. Rev. Lett. 110 (2013), 085501, https://doi.org/10.1103/physrevlett.110.085501.

[216] J.H. Jørgensen, A.G. Čabo, R. Balog, L. Kyhl, M.N. Groves, A.M. Cassidy, A. Bruix, M. Bianchi, M. Dendzik, M.A. Arman, L. Lammich, J.I. Pascual, J. Knudsen, B. Hammer, P. Hofmann, L. Hornekaer, Symmetry-driven band gap engineering in hydrogen functionalized graphene, ACS Nano 10 (2016) 10798–10807, https://doi.org/10.1021/acsnano.6b04671.

[217] K. Schulte, N. Vinogradov, M. Ng, N. Mårtensson, A. Preobrajenski, Bandgap formation in graphene on Ir(111) through oxidation, Appl. Surf. Sci. 267 (2013) 74–76, https://doi.org/10.1016/j.apsusc.2012.07.122.

[218] C. Bie, H. Yu, B. Cheng, W. Ho, J. Fan, J. Yu, Design, fabrication, and mechanism of nitrogen-doped graphene-based photocatalyst, Adv. Mater. 33 (9) (2021), 2003521, https://doi.org/10.1002/adma.202003521.

[219] H.-Y. Zhuo, X. Zhang, J.-X. Liang, Q. Yu, H. Xiao, J. Li, Theoretical understandings of graphene-based metal single-atom catalysts: stability and catalytic performance, Chem. Rev. 120 (21) (2020) 12315–12341, https://doi.org/10.1021/acs.chemrev.0c00818.

[220] H. Xu, L. Ma, Z. Jin, Nitrogen-doped graphene: synthesis, characterizations and energy applications, J. Energy Chem. 27 (1) (2018) 146–160, https://doi.org/10.1016/j.jechem.2017.12.006.

[221] R. Balog, M. Andersen, B. Jørgensen, Z. Sljivancanin, B. Hammer, A. Baraldi, R. Larciprete, P. Hofmann, L. Hornekær, S. Lizzit, Controlling hydrogenation of graphene on Ir(111), ACS Nano 7 (2013) 3823–3832, https://doi.org/10.1021/nn400780x.

[222] J.O. Sofo, A.S. Chaudhari, G.D. Barber, Graphane: a two-dimensional hydrocarbon, Phys. Rev. B 75 (2007), 153401, https://doi.org/10.1103/physrevb.75.153401.

[223] R. Balog, B. Jørgensen, L. Nilsson, M. Andersen, E. Rienks, M. Bianchi, M. Fanetti, E. Lægsgaard, A. Baraldi, S. Lizzit, Z. Sljivancanin, F. Besenbacher, B. Hammer, T. G. Pedersen, P. Hofmann, L. Hornekær, Bandgap opening in graphene induced by

[224] A. Bostwick, J.L. McChesney, K.V. Emtsev, T. Seyller, K. Horn, S.D. Kevan, E. Rotenberg, Quasiparticle transformation during a metal-insulator transition in graphene, Phys. Rev. Lett. 103 (2009), 056404, https://doi.org/10.1103/physrevlett.103.056404.

[225] N.P. Guisinger, G.M. Rutter, J.N. Crain, P.N. First, J.A. Stroscio, Exposure of epitaxial graphene on SiC(0001) to atomic hydrogen, Nano Lett. 9 (2009) 1462–1466, https://doi.org/10.1021/nl803331q.

[226] M.L. Ng, R. Balog, L. Hornekær, A.B. Preobrajenski, N.A. Vinogradov, N. Mårtensson, K. Schulte, Controlling hydrogenation of graphene on transition metals, J. Phys. Chem. C 114 (2010) 18559–18565, https://doi.org/10.1021/jp106361y.

[227] R. Balog, A. Cassidy, J. Jørgensen, L. Kyhl, M. Andersen, A.G. Čabo, F. Ravani, L. Bignardi, P. Lacovig, S. Lizzit, L. Hornekær, Hydrogen interaction with graphene on Ir(111): a combined intercalation and functionalization study, J. Phys. Condens. Matter 31 (2019), 085001, https://doi.org/10.1088/1361-648x/aaf76b.

[228] L. Kyhl, R. Balog, A. Cassidy, J. Jørgensen, A. Grubisic-Čabo, L. Trotochaud, H. Bluhm, L. Hornekær, Enhancing graphene protective coatings by hydrogen-induced chemical bond formation, ACS Appl. Nano Mater. 1 (2018) 4509–4515, https://doi.org/10.1021/acsanm.8b00610.

[229] M. Panahi, N. Solati, A. Kahraman, T. Balkan, I. Píš, F. Bondino, S. Kaya, Charge transfer controlled hydrogenation of graphene on an electronically modified Pt (111) surface, Carbon 170 (2020) 636–645, https://doi.org/10.1016/j.carbon.2020.08.037.

[230] D. Haberer, D.V. Vyalikh, S. Taioli, B. Dora, M. Farjam, J. Fink, D. Marchenko, T. Pichler, K. Ziegler, S. Simonucci, M.S. Dresselhaus, M. Knupfer, B. Büchner, A. Grüneis, Tunable band gap in hydrogenated quasi-free-standing graphene, Nano Lett. 10 (2010) 3360–3366, https://doi.org/10.1021/nl101066m.

[231] A. Paris, N. Verbitskiy, A. Nefedov, Y. Wang, A. Fedorov, D. Haberer, M. Oehzelt, L. Petaccia, D. Usachov, D. Vyalikh, H. Sachdev, C. Wöll, M. Knupfer, B. Büchner, L. Calliari, L. Yashina, S. Irle, A. Grüneis, Kinetic isotope effect in the hydrogenation and deuteration of graphene, Adv. Funct. Mater. 23 (2012) 1628–1635, https://doi.org/10.1002/adfm.201202355.

[232] W. Zhao, J. Gebhardt, F. Späth, K. Gotterbarm, C. Gleichweit, H.-P. Steinrück, A. Görling, C. Papp, Reversible hydrogenation of graphene on ni(111)—synthesis of "graphone", Eur. J. Chem. 21 (8) (2015) 3347–3358, https://doi.org/10.1002/chem.201404938.

[233] D. Lizzit, M.I. Trioni, L. Bignardi, P. Lacovig, S. Lizzit, R. Martinazzo, R. Larciprete, Dual-route hydrogenation of the graphene/Ni interface, ACS Nano 13 (2019) 1828–1838, https://doi.org/10.1021/acsnano.8b07996.

[234] R. Larciprete, S. Fabris, T. Sun, P. Lacovig, A. Baraldi, S. Lizzit, Dual path mechanism in the thermal reduction of graphene oxide, J. Am. Chem. Soc. 133 (2011) 17315–17321, https://doi.org/10.1021/ja205168x.

[235] E. Bahn, A. Tamtögl, J. Ellis, W. Allison, P. Fouquet, Structure and dynamics investigations of a partially hydrogenated graphene/Ni(111) surface, Carbon 114 (2017) 504–510, https://doi.org/10.1016/j.carbon.2016.12.055.

[236] G. Petrone, F. Zarotti, P. Lacovig, D. Lizzit, E. Tosi, R. Felici, S. Lizzit, R. Larciprete, The effect of structural disorder on the hydrogen loading into the graphene/nickel interface, Carbon 199 (2022) 357–366, https://doi.org/10.1016/j.carbon.2022.07.050.

[237] P.P. Brisebois, M. Siaj, Harvesting graphene oxide – years 1859 to 2019: a review of its structure, synthesis, properties and exfoliation, J. Mater. Chem. C 8 (2020) 1517–1547, https://doi.org/10.1039/c9tc03251g.

[238] L. Camilli, F. Yu, A. Cassidy, L. Hornekær, P. Bøggild, Challenges for continuous graphene as a corrosion barrier, 2D Mater. 6 (2019), 022002, https://doi.org/10.1088/2053-1583/ab04d4.

[239] T. Szabó, O. Berkesi, P. Forgó, K. Josepovits, Y. Sanakis, D. Petridis, I. Dékány, Evolution of surface functional groups in a series of progressively oxidized graphite oxides, Chem. Mater. 18 (2006) 2740–2749, https://doi.org/10.1021/cm060258.

[240] O.C. Compton, S.T. Nguyen, Graphene oxide, highly reduced graphene oxide, and graphene: versatile building blocks for carbon-based materials, Small 6 (2010) 711–723, https://doi.org/10.1002/smll.200901934.

[241] D.R. Dreyer, S. Park, C.W. Bielawski, R.S. Ruoff, The chemistry of graphene oxide, Chem. Soc. Rev. 39 (2010) 228–240, https://doi.org/10.1039/b917103g.

[242] G. Eda, M. Chhowalla, Chemically derived graphene oxide: towards large-area thin-film electronics and optoelectronics, Adv. Mater. 22 (2010) 2392–2415, https://doi.org/10.1002/adma.200903689.

[243] N.A. Vinogradov, K. Schulte, M.L. Ng, A. Mikkelsen, E. Lundgren, N. Mårtensson, A.B. Preobrajenski, Impact of atomic oxygen on the structure of graphene formed on Ir(111) and Pt(111), J. Phys. Chem. C 115 (2011) 9568–9577, https://doi.org/10.1021/jp111962k.

[244] R. Larciprete, P. Lacovig, S. Gardonio, A. Baraldi, S. Lizzit, Atomic oxygen on graphite: chemical characterization and thermal reduction, J. Phys. Chem. C 116 (2012) 9900–9908, https://doi.org/10.1021/jp2098153.

[245] J. Jung, H. Lim, J. Oh, Y. Kim, Functionalization of graphene grown on metal substrate with atomic oxygen: enolate vs epoxide, J. Am. Chem. Soc. 136 (2014) 8528–8531, https://doi.org/10.1021/ja503664k.

[246] A. Cassidy, S. Pedersen, H. Bluhm, V. Calisti, T. Angot, E. Salomon, R. Bisson, L. Hornekær, Patterned formation of enolate functional groups on the graphene basal plane, Phys. Chem. Chem. Phys. 20 (2018) 28370–28374, https://doi.org/10.1039/c8cp05730c.

[247] Z. Novotny, M.-T. Nguyen, F.P. Netzer, V.-A. Glezakou, R. Rousseau, Z. Dohnálek, Formation of supported graphene oxide: evidence for enolate species, J. Am. Chem. Soc. 140 (2018) 5102–5109, https://doi.org/10.1021/jacs.7b12791.

[248] D. Wei, Y. Liu, Y. Wang, H. Zhang, L. Huang, G. Yu, Synthesis of n-doped graphene by chemical vapor deposition and its electrical properties, Nano Lett. 9 (2009) 1752–1758, https://doi.org/10.1021/nl803279t.

[249] D. Usachov, O. Vilkov, A. Grüneis, D. Haberer, A. Fedorov, V.K. Adamchuk, A. B. Preobrajenski, P. Dudin, A. Barinov, M. Oehzelt, C. Laubschat, D.V. Vyalikh, Nitrogen-doped graphene: efficient growth, structure, and electronic properties, Nano Lett. 11 (2011) 5401–5407, https://doi.org/10.1021/nl2031037.

[250] D. Usachov, A. Fedorov, O. Vilkov, B. Senkovskiy, V.K. Adamchuk, L.V. Yashina, A.A. Volykhov, M. Farjam, N.I. Verbitskiy, A. Grüneis, C. Laubschat, D.V. Vyalikh, The chemistry of imperfections in N-graphene, Nano Lett. 14 (2014) 4982 4988, https://doi.org/10.1021/nl501389h.

[251] D.Y. Usachov, A.V. Fedorov, A.E. Petukhov, O.Y. Vilkov, A.G. Rybkin, M. M. Otrokov, A. Arnau, E.V. Chulkov, L.V. Yashina, M. Farjam, V.K. Adamchuk, B. V. Senkovskiy, C. Laubschat, D.V. Vyalikh, Epitaxial B-graphene: large-scale growth and atomic structure, ACS Nano 9 (2015) 7314–7322, https://doi.org/10.1021/acsnano.5b02322.

[252] F. Orlando, P. Lacovig, M. Dalmiglio, A. Baraldi, R. Larciprete, S. Lizzit, Synthesis of nitrogen-doped epitaxial graphene via plasma-assisted method: role of the graphene–substrate interaction, Surf. Sci. 643 (2015) 214–221, https://doi.org/10.1016/j.susc.2015.06.017.

[253] M. Scardamaglia, T. Susi, C. Struzzi, R. Snyders, G.D. Santo, L. Petaccia, C. Bittencourt, Spectroscopic observation of oxygen dissociation on nitrogen-doped graphene, Sci. Rep. 7 (1) (2017) 7960, https://doi.org/10.1038/s41598-017-08651-1.

[254] A.T. N'Diaye, S. Bleikamp, P.J. Feibelman, T. Michely, Two-dimensional Ir cluster lattice on a graphene moire on Ir(111), Phys. Rev. Lett. 97 (2006), 215501, https://doi.org/10.1103/physrevlett.97.215501.

[255] A.T. N'Diaye, T. Gerber, C. Busse, J. Mysliveček, J. Coraux, T. Michely, A versatile fabrication method for cluster superlattices, New J. Phys. 11 (2009), 103045, https://doi.org/10.1088/1367-2630/11/10/103045.

[256] T. Hartl, M. Will, D. Čapeta, R. Singh, D. Scheinecker, V.B.d. l. Cruz, S. Dellmann, P. Lacovig, S. Lizzit, B.V. Senkovskiy, A. Grüneis, M. Kralj, J. Knudsen, J. Kotakoski, T. Michely, P. Bampoulis, Cluster superlattice membranes, ACS Nano 14 (2020) 13629–13637, https://doi.org/10.1021/acsnano.0c05740.

[257] M. Will, P. Bampoulis, T. Hartl, P. Valerius, T. Michely, Conformal embedding of cluster superlattices with carbon, ACS Appl. Mater. Interfaces 11 (2019) 40524–40532, https://doi.org/10.1021/acsami.9b14616.

[258] X. Liu, C.Z. Wang, M. Hupalo, W.C. Lu, M.C. Tringides, Y.X. Yao, K.M. Ho, Metals on graphene: correlation between adatom adsorption behavior and growth morphology, Phys. Chem. Chem. Phys. 14 (2012) 9157–9166, https://doi.org/10.1039/c2cp40527j.

[259] R.T. Frederick, Z. Novotny, F.P. Netzer, G.S. Herman, Z. Dohnálek, Growth and stability of titanium dioxide nanoclusters on graphene/Ru(0001), J. Phys. Chem. B 122 (2018) 640–648, https://doi.org/10.1021/acs.jpcb.7b05518.

[260] Z. Zhou, F. Gao, D.W. Goodman, Deposition of metal clusters on single-layer graphene/Ru(0001): factors that govern cluster growth, Surf. Sci. 604 (2010) L31–L38, https://doi.org/10.1016/j.susc.2010.03.008.

[261] A. Locatelli, C. Wang, C. Africh, N. Stojić, T.O. Menteş, G. Comelli, N. Binggeli, Temperature-driven reversible rippling and bonding of a graphene superlattice, ACS Nano 7 (2013) 6955–6963, https://doi.org/10.1021/nn402178u.

[262] A. Varykhalov, O. Rader, W. Gudat, Structure and quantum-size effects in a surface carbide: W(110)/C-R(15 × 3), Phys. Rev. B 72 (2004), 115440, https://doi.org/10.1103/PhysRevB.72.115440.

[263] B. Casarin, A. Cian, Z. Feng, E. Monachino, F. Randi, G. Zamborlini, M. Zonno, E. Miniussi, P. Lacovig, S. Lizzit, A. Baraldi, The thinnest carpet on the smallest staircase: the growth of graphene on Rh(533), J. Phys. Chem. C 118 (2014) 6242–6250, https://doi.org/10.1021/jp411582a.

[264] I.Š. Rakić, M. Kralj, W. Jolie, P. Lazić, W. Sun, J. Avila, M.-C. Asensio, F. Craes, V. M. Trontl, C. Busse, P. Pervan, Step-induced faceting and related electronic effects for graphene on Ir(332), Carbon 110 (2016) 267–277, https://doi.org/10.1016/j.carbon.2016.09.024.

[265] A. Celis, M.N. Nair, M. Sicot, F. Nicolas, D. Malterre, A. Taleb-Ibrahimi, A. Tejeda, Superlattice-induced minigaps in graphene band structure due to underlying one-dimensional nanostructuration, Phys. Rev. B 97 (2018), 195410, https://doi.org/10.1103/physrevb.97.195410.

[266] E.Y. Kataev, D.Y. Usachov, A.S. Frolov, A.A. Rulev, A.A. Volykhov, A. Y. Kozmenkova, M. Krivenkov, D. Marchenko, A. Varykhalov, M.V. Kuznetsov, D. V. Vyalikh, L.V. Yashina, Native and graphene-coated flat and stepped surfaces of TiC, Carbon 132 (2018) 656–666, https://doi.org/10.1016/j.carbon.2018.02.065.

[267] A. Celis, M.N. Nair, M. Sicot, F. Nicolas, S. Kubsky, A. Taleb-Ibrahimi, D. Malterre, A. Tejeda, Growth, morphology and electronic properties of epitaxial graphene on vicinal Ir(332) surface, Acs Sym Ser 31 (2020), 285601, https://doi.org/10.1088/1361-6528/ab866a.

[268] G. Zamborlini, M. Imam, L.L. Patera, T.O. Menteş, N. Stojić, C. Africh, A. Sala, N. Binggeli, G. Comelli, A. Locatelli, Nanobubbles at GPa pressure under graphene, Nano Lett. 15 (2015) 6162–6169, https://doi.org/10.1021/acs.nanolett.5b02475.

[269] F. Späth, K. Gotterbarm, M. Amende, U. Bauer, C. Gleichweit, O. Höfert, H.-P. Steinrück, C. Papp, Keeping argon under a graphene lid–Argon intercalation between graphene and nickel(111), Surf. Sci. 643 (2016) 222–226, https://doi.org/10.1016/j.susc.2015.05.009.

[270] R. Larciprete, S. Colonna, F. Ronci, R. Flammini, P. Lacovig, N. Apostol, A. Politano, P. Feulner, D. Menzel, S. Lizzit, Self-assembly of graphene nanoblisters sealed to a bare metal surface, Nano Lett. 16 (2016) 1808–1817, https://doi.org/10.1021/acs.nanolett.5b04849.

[271] M. Pozzo, D. Alfè, P. Lacovig, P. Hofmann, S. Lizzit, A. Baraldi, Thermal expansion of supported and freestanding graphene: lattice constant versus interatomic distance, Phys. Rev. Lett. 106 (2011), 135501, https://doi.org/10.1103/physrevlett.106.135501.

[272] C. Lee, X. Wei, J.W. Kysar, J. Hone, Measurement of the elastic properties and intrinsic strength of monolayer graphene, Science 321 (2008) 385–388, https://doi.org/10.1126/science.1157996.

[273] W. Bao, F. Miao, Z. Chen, H. Zhang, W. Jang, C. Dames, C.N. Lau, Controlled ripple texturing of suspended graphene and ultrathin graphite membranes, Nat. Nanotechnol. 4 (2009) 562–566, https://doi.org/10.1038/nnano.2009.191.

[274] N. Bonini, M. Lazzeri, N. Marzari, F. Mauri, Phonon anharmonicities in graphite and graphene, Phys. Rev. Lett. 99 (2007), 176802, https://doi.org/10.1103/physrevlett.99.176802.

[275] J.-W. Jiang, J.-S. Wang, B. Li, Thermal expansion in single-walled carbon nanotubes and graphene: nonequilibrium Green's function approach, Phys. Rev. B 80 (2009), 205429, https://doi.org/10.1103/physrevb.80.205429.

[276] N. Mounet, N. Marzari, First-principles determination of the structural, vibrational and thermodynamic properties of diamond, graphite, and derivatives, Phys. Rev. B 71 (2005), 205214, https://doi.org/10.1103/physrevb.71.205214.

[277] K.V. Zakharchenko, M.I. Katsnelson, A. Fasolino, Finite temperature lattice properties of graphene beyond the quasiharmonic approximation, Phys. Rev. Lett. 102 (2009), 046808, https://doi.org/10.1103/physrevlett.102.046808.

[278] K.A. Gschneidner, in: Physical Properties and Interrelationships of Metallic and Semimetallic Elements, vol. 16, Academic Press, Cambridge, MA), 1964, pp. 275–426, https://doi.org/10.1016/S0081-1947(08)60518-4, of Solid State Physics.

[279] Y.Y. Illarionov, T. Knobloch, M. Jech, M. Lanza, D. Akinwande, M.I. Vexler, T. Mueller, M.C. Lemme, G. Fiori, F. Schwierz, et al., Insulators for 2D nanoelectronics: the gap to bridge, Nat. Commun. 11 (2020) 3385, https://doi.org/10.1038/s41467-020-16640-8.

[280] C. Becker, K. Wandelt, Surfaces: two-dimensional templates, in: P. Broekmann, K.-H. Dötz, C.A. Schalley (Eds.), Templates in Chemistry III, vol. 287, Springer Verlag, 2005, pp. 45–86, https://doi.org/10.1007/128_2008_151, of Topics in Current Chemistry-Series.

[281] W. Auwärter, Hexagonal boron nitride monolayers on metal supports: versatile templates for atoms, molecules and nanostructures, Surf. Sci. Rep. 74 (2018) 1–95, https://doi.org/10.1016/j.surfrep.2018.10.001.

[282] H. Hibino, S. Wang, C. Orofeo, H. Kageshima, Growth and low-energy electron microscopy characterizations of graphene and hexagonal boron nitride, Prog. Cryst. Growth Char. 62 (2016) 155–176, https://doi.org/10.1016/j.pcrysgrow.2016.04.008.

[283] H. Wang, Y. Zhao, Y. Xie, X. Ma, X. Zhang, Recent progress in synthesis of two-dimensional hexagonal boron nitride, J. Semiconduct. 38 (2017), 031003, https://doi.org/10.1088/1674-4926/38/3/031003.

[284] A. Preobrajenski, A. Vinogradov, N. Martensson, Ni 3d-BN π hybridization at the h-BN/Ni(111) interface observed with core-level spectroscopies, Phys. Rev. B 70 (2004), 165404, https://doi.org/10.1103/PhysRevB.70.165404.

[285] A. Preobrajenski, A. Vinogradov, N. Martensson, Monolayer of h-BN chemisorbed on Cu(111) and Ni(111): the role of the transition metal 3d states, Surf. Sci. 582 (2005) 21–30, https://doi.org/10.1016/j.susc.2005.02.047.

[286] A. Preobrajenski, M. Nesterov, M.L. Ng, A. Vinogradov, N. Mårtensson, Monolayer h-BN on lattice-mismatched metal surfaces: on the formation of the nanomesh, Chem. Phys. Lett. 446 (2007) 119–123, https://doi.org/10.1016/j.cplett.2007.08.028.

[287] A.B. Preobrajenski, S.A. Krasnikov, A.S. Vinogradov, M.L. Ng, T. Käämbre, A. A. Cafolla, N. Mårtensson, Adsorption-induced gap states of h-BN on metal surfaces, Phys. Rev. B 77 (2008), 085421, https://doi.org/10.1103/PhysRevB.77.085421.

[288] N.A. Vinogradov, A.A. Zakharov, M.L. Ng, A. Mikkelsen, E. Lundgren, N. Mårtensson, A.B. Preobrajenski, One-dimensional corrugation of the h-BN monolayer on Fe(110), Langmuir 28 (2012) 1775–1781, https://doi.org/10.1021/la2035642.

[289] M. Schwarz, A. Riss, M. Garnica, J. Ducke, P.S. Deimel, D.A. Duncan, P.K. Thakur, T.-L. Lee, A.P. Seitsonen, J.V. Barth, F. Allegretti, W. Auwärter, Corrugation in the weakly interacting hexagonal-BN/Cu(111) system: structure determination by combining noncontact atomic force microscopy and X-ray standing waves, ACS Nano 11 (2017) 9151–9161, https://doi.org/10.1021/acsnano.7b04022.

[290] M. Schwarz, M. Garnica, F. Fasano, N. Demitri, D. Bonifazi, W. Auwaerter, BN-patterning of metallic substrates through metal coordination of decoupled borazines, Chem. Eur J. 24 (2018) 9565–9571, https://doi.org/10.1002/chem.201800849.

[291] L. Camilli, E. Sutter, P. Sutter, Growth of two-dimensional materials on non-catalytic substrates: h-BN/Au(111), 2D Mater. 1 (2014) 025003, https://doi.org/10.1088/2053-1583/1/2/025003.

[292] E. Ćavar, R. Westerström, A. Mikkelsen, E. Lundgren, A. Vinogradov, M.L. Ng, A. Preobrajenski, A. Zakharov, N. Mårtensson, A single h-BN layer on Pt(111), Surf. Sci. 602 (2008) 1722–1726, https://doi.org/10.1016/j.susc.2008.03.008.

[293] F.H. F.z. Hagen, D.M. Zimmermann, C.C. Silva, C. Schlueter, N. Atodiresei, W. Jolie, A.J. Martinez-Galera, D. Dombrowski, U.A. Schroder, M. Will, P. Lazic, V. Caciuc, S. Blugel, T.-L. Lee, T. Michely, C. Busse, Structure and growth of hexagonal boron nitride on Ir(111), ACS Nano 10 (2016) 11012–11026, https://doi.org/10.1021/acsnano.6b05819.

[294] J. Hadid, I. Colombo, C. Boyaval, N. Nuns, P. Dudin, J. Avila, X. Wallart, D. Vignaud, Molecular beam epitaxial growth of hexagonal boron nitride on Ni foils, 2D Mater. 8 (2021), 045007, https://doi.org/10.1088/2053-1583/ac1502.

[295] W. Yang, G. Chen, Z. Shi, C.-C. Liu, L. Zhang, G. Xie, M. Cheng, D. Wang, R. Yang, D. Shi, K. Watanabe, T. Taniguchi, Y. Yao, Y. Zhang, G. Zhang, Epitaxial growth of single-domain graphene on hexagonal boron nitride, Nat. Mater. 12 (2013) 792–797, https://doi.org/10.1038/nmat3695.

[296] J. Wrigley, J. Bradford, T. James, T.S. Cheng, J. Thomas, C.J. Mellor, A. N. Khlobystov, L. Eaves, C.T. Foxon, S.V. Novikov, P.H. Beton, Epitaxy of boron nitride monolayers for graphene-based lateral heterostructures, 2D Mater. 8 (2021), 034001, https://doi.org/10.1088/2053-1583/abea66.

[297] S. Wang, J. Crowther, H. Kageshima, H. Hibino, Y. Taniyasu, Epitaxial intercalation growth of scalable hexagonal boron nitride/graphene bilayer moiré materials with highly convergent interlayer angles, ACS Nano 15 (2021) 14384–14393, https://doi.org/10.1021/acsnano.1c03698.

[298] A. Nagashima, N. Tejima, Y. Gamou, T. Kawai, C. Oshima, Electronic structure of monolayer hexagonal boron nitride physisorbed on metal surfaces, Phys. Rev. Lett. 75 (1995) 3918–3921, https://doi.org/10.1103/physrevlett.75.3918.

[299] A. Nagashima, N. Tejima, Y. Gamou, T. Kawai, C. Oshima, Electronic dispersion relations of monolayer hexagonal boron nitride formed on the ni(111) surface, Phys. Rev. B 51 (1995) 4606–4613, https://doi.org/10.1103/physrevb.51.4606.

[300] C. Oshima, A. Nagashima, Ultra-thin epitaxial films of graphite and hexagonal boron nitride on solid surfaces, J. Phys. Condens. Matter 9 (1997) 1–20, https://doi.org/10.1088/0953-8984/9/1/004.

[301] F. Orlando, R. Larciprete, P. Lacovig, I. Boscarato, A. Baraldi, S. Lizzit, Epitaxial growth of hexagonal boron nitride on Ir(111), J. Phys. Chem. C 116 (2012) 157–164, https://doi.org/10.1021/jp207571n.

[302] F. Orlando, P. Lacovig, L. Omiciuolo, N.G. Apostol, R. Larciprete, A. Baraldi, S. Lizzit, Epitaxial growth of a single-domain hexagonal boron nitride mono layer, ACS Nano 8 (2014) 12063–12070, https://doi.org/10.1021/nn5058968.

[303] F.J. G.d. Abajo, M.A.V. Hove, C.S. Fadley, Multiple scattering of electrons in solids and molecules: a cluster-model approach, Phys. Rev. B 63 (2001), 075404, https://doi.org/10.1103/physrevb.63.075404.

[304] F. Späth, J. Gebhardt, F. Düll, U. Bauer, P. Bachmann, C. Gleichweit, A. Görling, H.-P. Steinrück, C. Papp, Hydrogenation and hydrogen intercalation of hexagonal boron nitride on Ni(111): reactivity and electronic structure, 2D Mater. 4 (2017), 035026, https://doi.org/10.1088/2053-1583/aa7d6b.

[305] K.A. Simonov, N.A. Vinogradov, M.L. Ng, A.S. Vinogradov, N. Martensson, A. B. Preobrajenski, Controllable oxidation of h-BN monolayer on Ir(111) studied by core-level spectroscopies, Surf. Sci. 606 (2012) 564–570, https://doi.org/10.1016/j.susc.2011.11.031.

[306] M.C. Patterson, B.F. Habenicht, R.L. Kurtz, L. Liu, Y. Xu, P.T. Sprunger, Formation and stability of dense arrays of Au nanoclusters on hexagonal boron nitride/Rh (111), Phys. Rev. B 89 (2014), 205423, https://doi.org/10.1103/physrevb.89.205423.

[307] M. Will, N. Atodiresei, V. Caciuc, P. Valerius, C. Herbig, T. Michely, A monolayer of hexagonal boron nitride on Ir(111) as a template for cluster superlattices, ACS Nano 12 (2018) 6871–6880, https://doi.org/10.1021/acsnano.8b02127.

[308] M. Will, T. Hartl, V.b.d. l. Cruz, P. Lacovig, S. Lizzit, J. Knudsen, T. Michely, P. Bampoulis, Growth, stability, and electronic decoupling of Pt clusters on h-BN/ Ir(111), J. Phys. Chem. C 125 (2021) 3880–3889, https://doi.org/10.1021/acs.jpcc.0c10136.

[309] F. Düll, M. Meusel, F. Späth, S. Schötz, U. Bauer, P. Bachmann, J. Steinhauer, H.-P. Steinrück, A. Bayer, C. Papp, Growth and stability of Pt nanoclusters from 1 to 50 atoms on h-BN/Rh(111), Phys. Chem. Chem. Phys. 21 (2019) 21287–21295, https://doi.org/10.1039/c9cp04095a.

[310] T. Brugger, H. Ma, M. Iannuzzi, S. Berner, A. Winkler, J. Hutter, J. Osterwalder, T. Greber, Nanotexture switching of single-layer hexagonal boron nitride on rhodium by intercalation of hydrogen atoms, Angew. Chem. Int. Ed. 49 (2010) 6120–6124, https://doi.org/10.1002/ange.201001064.

[311] M.S. Driver, J.D. Beatty, O. Olanipekun, K. Reid, A. Rath, P.M. Voyles, J. A. Kelber, Atomic layer epitaxy of h-BN(0001) multilayers on Co(0001) and molecular beam epitaxy growth of graphene on h-BN(0001)/Co(0001), Langmuir 32 (2016) 2601–2607, https://doi.org/10.1021/acs.langmuir.5b03653.

[312] M. Wei, Q. Fu, H. Wu, A. Dong, X. Bao, Hydrogen intercalation of graphene and boron nitride monolayers grown on Pt(111), Top. Catal. 59 (2016) 543–549, https://doi.org/10.1007/s11244-015-0516-4.

[313] A.B. Preobrajenski, M.L. Ng, N.A. Vinogradov, A.S. Vinogradov, E. Lundgren, A. Mikkelsen, N. Martensson, Impact of oxygen coadsorption on intercalation of cobalt under the h-BN nanomesh, Nano Lett. 9 (2009) 2780–2787, https://doi.org/10.1021/nl901316p.

[314] A. Fedorov, C.S. Praveen, N.I. Verbitskiy, D. Haberer, D. Usachov, D.V. Vyalikh, A. Nefedov, C. Wöll, L. Petaccia, S. Piccinin, H. Sachdev, B. Büchner, S. Fabris, A. Grüneis, Efficient gating of epitaxial boron nitride monolayers by substrate functionalization, Phys. Rev. B 92 (2015), 125440, https://doi.org/10.1103/physrevb.92.125440.

[315] N.I. Verbitskiy, A.V. Fedorov, G. Profeta, A. Stroppa, L. Petaccia, B. Senkovskiy, A. Nefedov, C. Woell, D.Y. Usachov, D.V. Vyalikh, L.V. Yashina, A.A. Eliseev, T. Pichler, A. Grueneis, Atomically precise semiconductor-graphene and hBN interfaces by Ge intercalation, Sci. Rep. 5 (2015), 17700, https://doi.org/10.1038/srep17700.

[316] R. Gubó, G. Vári, J. Kiss, A.P. Farkas, K. Palotás, L. Óvári, A. Berkó, Z. Kónya, Tailoring the hexagonal boron nitride nanomesh on Rh(111) with gold, Phys. Chem. Chem. Phys. 20 (2018) 15473–15485, https://doi.org/10.1039/c8cp00790j.

[317] D. Usachov, V.K. Adamchuk, D. Haberer, A. Grüneis, H. Sachdev, A. B. Preobrajenski, C. Laubschat, D.V. Vyalikh, Quasifreestanding single-layer hexagonal boron nitride as a substrate for graphene synthesis, Phys. Rev. B 82 (2010), 075415, https://doi.org/10.1103/physrevb.82.075415.

[318] A. Goriachko, M. Knapp He, H. Over, M. Corso, T. Brugger, S. Berner, J. Osterwalder, T. Greber, Self-assembly of a hexagonal boron nitride nanomesh on Ru(0001), Langmuir 23 (6) (2007) 2928–2931, https://doi.org/10.1021/la062990t.

[319] M. Ng, A. Preobrajenski, A. Vinogradov, N. Mårtensson, Formation and temperature evolution of Au nanoparticles supported on the h-BN nanomesh, Surf. Sci. 602 (2008) 1250–1255, https://doi.org/10.1016/j.susc.2008.01.028.

[320] B. Radisavljevic, A. Radenovic, J. Brivio, V. Giacometti, A. Kis, Single-layer mos2 transistors, Nat. Nanotechnol. 6 (3) (2011) 147–150, https://doi.org/10.1038/nnano.2010.279.

[321] K.F. Mak, J. Shan, Photonics and optoelectronics of 2D semiconductor transition metal dichalcogenides, Nat. Photonics 10 (2016) 216–226, https://doi.org/10.1038/nphoton.2015.282.

[322] K.F. Mak, J. Shan, Opportunities and challenges of interlayer exciton control and manipulation, Nat. Nanotechnol. 13 (2018) 974–976, https://doi.org/10.1038/s41565-018-0301-1.

[323] M. Chhowalla, H.S. Shin, G. Eda, L.-J. Li, K.P. Loh, H. Zhang, The chemistry of two-dimensional layered transition metal dichalcogenide nanosheets, Nat. Chem. 5 (2013) 263 275, https://doi.org/10.1038/nchem.1589.

[324] M. Chhowalla, D. Jena, H. Zhang, Two-dimensional semiconductors for transistors, Nat. Rev. Mater. 1 (2016) 1–15, https://doi.org/10.1038/natrevmats.2016.52.

[325] Y. Liu, X. Duan, H.-J. Shin, S. Park, Y. Huang, X. Duan, Promises and prospects of two-dimensional transistors, Nature 591 (7848) (2021) 43–53, https://doi.org/10.1038/s41586-021-03339-z.

[326] K.-A.N. Duerloo, Y. Li, E.J. Reed, Structural phase transitions in two-dimensional Mo- and W-dichalcogenide monolayers, Nat. Commun. 5 (2014) 4214, https://doi.org/10.1038/ncomms5214.

[327] Z. Wang, Y.-Y. Sun, I. Abdelwahab, L. Cao, W. Yu, H. Ju, J. Zhu, W. Fu, L. Chu, H. Xu, K.P. Loh, Surface-limited superconducting phase transition on 1T-TaS₂, ACS Nano 12 (2018) 12619–12628, https://doi.org/10.1021/acsnano.8b07379.

[328] A. Splendiani, L. Sun, Y. Zhang, T. Li, J. Kim, C.-Y. Chim, G. Galli, F. Wang, Emerging photoluminescence in monolayer MoS₂, Nano Lett. 10 (2010) 1271–1275, https://doi.org/10.1021/nl903868w, cited By 6543.

[329] K. Lasek, J. Li, S. Kolekar, P.M. Coelho, L. Guo, M. Zhang, Z. Wang, M. Batzill, Synthesis and characterization of 2D transition metal dichalcogenides: recent progress from a vacuum surface science perspective, Surf. Sci. Rep. 76 (2021), 100523, https://doi.org/10.1016/j.surfrep.2021.100523.

[330] S. Manzeli, D. Ovchinnikov, D. Pasquier, O.V. Yazyev, A. Kis, 2D transition metal dichalcogenides, Nat. Rev. Mater. 2 (2017) 17033 15, https://doi.org/10.1038/natrevmats.2017.33.

[331] J.R. Brent, N. Savjani, P. O'Brien, Synthetic approaches to two-dimensional transition metal dichalcogenide nanosheets, Prog. Mater. Sci. 89 (2017) 411–478, https://doi.org/10.1016/j.pmatsci.2017.06.002.

[332] F. Arnold, R.M. Stan, S.K. Mahatha, H.E. Lund, D. Curcio, M. Dendzik, H. Bana, E. Travaglia, L. Bignardi, P. Lacovig, D. Lizzit, Z. Li, M. Bianchi, J.A. Miwa, M. Bremholm, S. Lizzit, P. Hofmann, C.E. Sanders, Novel single-layer vanadium sulphide phases, 2D Mater. 5 (2018), 045009, https://doi.org/10.1088/2053-1583/aad0c8.

[333] H. Bana, E. Travaglia, L. Bignardi, P. Lacovig, C.E. Sanders, M. Dendzik, M. Michiardi, M. Bianchi, D. Lizzit, F. Presel, D.D. Angelis, N. Apostol, P.K. Das, J. Fujii, I. Vobornik, R. Larciprete, A. Baraldi, P. Hofmann, S. Lizzit, Epitaxial growth of single-orientation high-quality MoS₂ monolayers, 2D Mater. 5 (2018), 035012, https://doi.org/10.1088/2053-1583/aabb74.

[334] H. Beyer, G. Rohde, A.G. Čabo, A. Stange, T. Jacobsen, L. Bignardi, D. Lizzit, C.E. Sanders, S. Lizzit, K. Rossnagel, P. Hofmann, M. Bauer, 80% valley polarization of free carriers in singly oriented single-layer WS₂ on Au(111), Phys. Rev. Lett. 123 (2019), 236802, https://doi.org/10.1103/PhysRevLett.123.236802.

[335] L. Bignardi, D. Lizzit, H. Bana, E. Travaglia, P. Lacovig, C.E. Sanders, M. Dendzik, M. Michiardi, M. Bianchi, M. Ewert, L. Buß, J. Falta, J.I. Flege, A. Baraldi, R. Larciprete, P. Hofmann, S. Lizzit, Growth and structure of singly oriented single-layer tungsten disulfide on Au(111), Phys. Rev. Mater. 3 (2019), 014003, https://doi.org/10.1103/physrevmaterials.3.014003.

[336] M. Dendzik, M. Michiardi, C. Sanders, M. Bianchi, J.A. Miwa, S.S.G. nborg, J. V. Lauritsen, A. Bruix, B.r. Hammer, P. Hofmann, Growth and electronic structure of epitaxial single-layer WS₂ on Au(111), Phys. Rev. B 92 (2015) 245442, https://doi.org/10.1103/PhysRevB.92.245442.

[337] R.-M. Stan, S. Mahatha, M. Bianchi, C. Sanders, D. Curcio, P. Hofmann, J. Miwa, Epitaxial single-layer NbS₂ on Au(111): synthesis, structure, and electronic properties, Phys. Rev. Mater. 3 (2019), 044003, https://doi.org/10.1103/PhysRevMaterials.3.044003.

[338] M. Dendzik, A. Bruix, M. Michiardi, A. Ngankeu, M. Bianchi, J. Miwa, B. Hammer, P. Hofmann, C. Sanders, Substrate-induced semiconductor-to-metal transition in monolayer WS₂, Phys. Rev. B 96 (2017) 235440, https://doi.org/10.1103/PhysRevB.96.235440.

[339] P. Eickholt, C. Sanders, M. Dendzik, L. Bignardi, D. Lizzit, S. Lizzit, A. Bruix, P. Hofmann, M. Donath, Spin structure of K valleys in single-layer WS₂ on Au (111), Phys. Rev. Lett. 121 (2018), 136402, https://doi.org/10.1103/PhysRevLett.121.136402.

[340] S.S. Grønborg, S. Ulstrup, M. Bianchi, M. Dendzik, C.E. Sanders, J.V. Lauritsen, P. Hofmann, J.A. Miwa, Synthesis of epitaxial single-layer MoS₂ on Au(111),

Langmuir 31 (2015) 9700–9706, https://doi.org/10.1021/acs. langmuir.5b02533.

[341] U. Kamber, S. Pakdel, R.-M. Stan, A. Kamlapure, B. Kiraly, F. Arnold, A. Eich, A. S. Ngankeu, M. Bianchi, J.A. Miwa, C.E. Sanders, N. Lanatà, P. Hofmann, A. A. Khajetoorians, Moiré-induced electronic structure modifications in monolayer V$_2$S$_3$ on Au(111), Phys. Rev. B 103 (2021), 115414, https://doi.org/10.1103/PhysRevB.103.115414.

[342] J.A. Miwa, S. Ulstrup, S.G. Sørensen, M. Dendzik, A.G. Čabo, M. Bianchi, J. V. Lauritsen, P. Hofmann, Electronic structure of epitaxial single-layer MoS$_2$, Phys. Rev. Lett. 114 (2015), 046802, https://doi.org/10.1103/PhysRevLett.114.046802.

[343] M.K. Prabhu, D. Boden, M.J. Rost, J. Meyer, I.M.N. Groot, Structural characterization of a novel two-dimensional material: cobalt sulfide sheets on Au (111), J. Phys. Chem. Lett. 11 (2020) 9038–9044, https://doi.org/10.1021/acs. jpclett.0c02268.

[344] C.C. Silva, D. Dombrowski, A. Samad, J. Cai, W. Jolie, J. Hall, P.T.P. Ryan, P. K. Thakur, D.A. Duncan, T.-L. Lee, U. Schwingenschlögl, C. Busse, Structure of monolayer 2H-TaS$_2$ on Au(111), Phys. Rev. B 104 (2021), 205414, https://doi.org/10.1103/PhysRevB.104.205414.

[345] C.C. Silva, D. Dombrowski, N. Atodiresei, W. Jolie, F.F.z. Hagen, J. Cai, P.T. P. Ryan, P.K. Thakur, V. Caciuc, S. Blügel, D.A. Duncan, T. Michely, T.-L. Lee, C. Busse, Spatial variation of geometry, binding, and electronic properties in the moiré superstructure of MoS$_2$ on Au(111), 2D Mater. 9 (2022), 025003, https://doi.org/10.1088/2053-1583/ac4958.

[346] D. Dombrowski, A. Samad, C. Murray, M. Petrović, P. Ewen, T. Michely, M. Kralj, U. Schwingenschlögl, C. Busse, Two phases of monolayer tantalum sulfide on Au (111), ACS Nano 15 (2021) 13516–13525, https://doi.org/10.1021/acsnano.1c04249.

[347] P. Dreher, W. Wan, A. Chikina, M. Bianchi, H. Guo, R. Harsh, S. Mañas-Valero, E. Coronado, A.J. Martínez-Galera, P. Hofmann, J.A. Miwa, M.M. Ugeda, Proximity effects on the charge density wave order and superconductivity in single-layer NbSe$_2$, ACS Nano 15 (2021) 19430–19438, https://doi.org/10.1021/acsnano.1c06012.

[348] D. Ding, S. Wang, Y. Xia, P. Li, D. He, J. Zhang, S. Zhao, G. Yu, Y. Zheng, Y. Cheng, M. Xie, F. Ding, C. Jin, Atomistic insight into the epitaxial growth mechanism of single-crystal two-dimensional transition-metal dichalcogenides on au(111) substrate, ACS Nano 16 (2022) 17356–17364, https://doi.org/10.1021/acsnano.2c08188.

[349] S.G. Sørensen, H.G. Füchtbauer, A.K. Tuxen, A.S. Walton, J.V. Lauritsen, Structure and electronic properties of in situ synthesized single-layer MoS$_2$ on a gold surface, ACS Nano 8 (2014) 6788–6796, https://doi.org/10.1021/nn502812n.

[350] A. Bruix, H.G. Füchtbauer, A.K. Tuxen, A.S. Walton, M. Andersen, S. Porsgaard, F. Besenbacher, B. Hammer, J.V. Lauritsen, In situ detection of active edge sites in single-layer MoS$_2$ catalysts, ACS Nano 9 (2015) 9322–9330, https://doi.org/10.1021/acsnano.5b03199.

[351] N. Salazar, I. Beinik, J.V. Lauritsen, Single-layer MoS$_2$ formation by sulfidation of molybdenum oxides in different oxidation states on Au(111), Phys. Chem. Chem. Phys. 19 (2017) 14020–14029, https://doi.org/10.1039/C7CP00958E.

[352] A. Syari'ati, S. Kumar, A. Zahid, A.A.E. Yumin, J. Ye, P. Rudolf, Photoemission spectroscopy study of structural defects in molybdenum disulfide (MoS$_2$) grown by chemical vapor deposition (CVD), Chem. Commun. 55 (2019) 10384–10387, https://doi.org/10.1039/C9CC01577A.

[353] M. Batzill, Mirror twin grain boundaries in molybdenum dichalcogenides, J. Phys. Condens. Matter 30 (2018), 493001, https://doi.org/10.1088/1361-648x/aae9cf.

[354] G.M.d. Amaral, I.d.C. Tonon, R.J.P. Román, H.d.O. Plath, T.M. Taniguchi, L.H. d. Lima, L.F. Zagonel, R. Landers, A.d. Siervo, Epitaxial growth, electronic hybridization and stability under oxidation of monolayer MoS$_2$ on Ag(111), Appl. Surf. Sci. 538 (2021), 148138, https://doi.org/10.1016/j.apsusc.2020.148138.

[355] L. Bignardi, S.K. Mahatha, D. Lizzit, H. Bana, E. Travaglia, P. Lacovig, C. Sanders, A. Baraldi, P. Hofmann, S. Lizzit, Anisotropic strain in epitaxial single-layer molybdenum disulfide on Ag(110), Nanoscale 13 (2021), 18789, https://doi.org/10.1039/d1nr05584d.

[356] D. Dumcenco, D. Ovchinnikov, O.L. Sanchez, P. Gillet, D.T.L. Alexander, S. Lazar, A. Radenovic, A. Kis, Large-area MoS$_2$ grown using H$_2$S as the sulphur source, 2D Mater. 2 (2015), 044005, https://doi.org/10.1088/2053-1583/2/4/044005.

[357] D. Dumcenco, D. Ovchinnikov, K. Marinov, P. Lazić, M. Gibertini, N. Marzari, O. Lopez-Sanchez, Y.-C. Kung, D. Krasnozhon, M.-W. Chen, S. Bertolazzi, P. Gillet, A.F.i. Morral, A. Radenovic, A. Kis, Large-area epitaxial monolayer MoS$_2$, ACS Nano 9 (2015) 4611 4620, https://doi.org/10.1021/acsnano.5b01281.

[358] S. Najmaei, Z. Liu, W. Zhou, X. Zou, G. Shi, S. Lei, B.I. Yakobson, J.-C. Idrobo, P. M. Ajayan, J. Lou, Vapour phase growth and grain boundary structure of molybdenum disulphide atomic layers, Nat. Mater. 12 (2013) 754–759, https://doi.org/10.1038/nmat3673.

[359] Y. Shi, W. Zhou, A.-Y. Lu, W. Fang, Y.-H. Lee, A.L. Hsu, S.M. Kim, K.K. Kim, H. Y. Yang, L.-J. Li, J.-C. Idrobo, J. Kong, van der Waals epitaxy of MoS$_2$ layers using graphene as growth templates, Nano Lett. 12 (2012) 2784–2791, https://doi.org/10.1021/nl204562j.

[360] F. Zhang, K. Momeni, M.A. AlSaud, A. Azizi, M.F.H. Jr, J.M. Redwing, L.-Q. Chen, N. Alem, Controlled synthesis of 2D transition metal dichalcogenides: from vertical to planar MoS$_2$, 2D Mater. 4 (2017-06), 025029, https://doi.org/10.1088/2053-1583/aa5b01.

[361] J. Hall, B. Pielić, C. Murray, W. Jolie, T. Wekking, C. Busse, M. Kralj, T. Michely, Molecular beam epitaxy of quasi-freestanding transition metal disulphide monolayers on van der Waals substrates: a growth study, 2D Mater. 5 (2018), 025005, https://doi.org/10.1088/2053-1583/aaa1c5.

[362] F. Loi, L. Sbuelz, P. Lacovig, D. Lizzit, L. Bignardi, S. Lizzit, A. Baraldi, Growth mechanism and thermal stability of a MoS$_2$-graphene interface: a high-resolution core-level photoelectron spectroscopy study, J. Phys. Chem. C 124 (2020) 20889–20897, https://doi.org/10.1021/acs.jpcc.0c05037.

[363] M. Bonilla, S. Kolekar, J. Li, Y. Xin, P.M. Coelho, K. Lasek, K. Zberecki, D. Lizzit, E. Tosi, P. Lacovig, S. Lizzit, M. Batzill, Compositional phase change of early transition metal diselenide (VSe$_2$ and TiSe$_2$) ultrathin films by postgrowth annealing, Adv. Mater. Interfac. 7 (2020), 2000497, https://doi.org/10.1002/admi.202000497.

[364] J. Wilson, A. Yoffe, The transition metal dichalcogenides discussion and interpretation of the observed optical, electrical and structural properties, Adv. Phys. 18 (73) (1969) 193–335, https://doi.org/10.1080/00018736900101307, 10.1080/00018736900101307.

[365] J. Li, S. Kolekar, Y. Xin, P.M. Coelho, K. Lasek, F.A. Nugera, H.R. Gutiérrez, M. Batzill, Thermal phase control of two-dimensional Pt-chalcogenide (Se and Te) ultrathin epitaxial films and nanocrystals, Chem. Mater. 33 (2021) 8018–8027, https://doi.org/10.1021/acs.chemmater.1c02163.

[366] E.G. Shkvarina, A.I. Merentsov, M.S. Postnikov, A.S. Shkvarin, S. V. Pryanichnikov, I. Píš, S. Nappini, F. Bondino, A.N. Titov, Electronic and crystal structure of bi-intercalated titanium diselenide CuxNiyTiSe$_2$, J. Mater. Chem. C 9 (2021) 1657–1670, https://doi.org/10.1039/D0TC03277H.

[367] H. Wang, X. Huang, J. Lin, J. Cui, Y. Chen, C. Zhu, F. Liu, Q. Zeng, J. Zhou, P. Yu, X. Wang, H. He, S.H. Tsang, W. Gao, K. Suenaga, F. Ma, C. Yang, L. Lu, T. Yu, E.H. T. Teo, G. Liu, Z. Liu, High-quality monolayer superconductor NbSe$_2$ grown by chemical vapour deposition, Nat. Commun. 8 (2017) 394, https://doi.org/10.1038/s41467-017-00427-5.

[368] A. Roy, H. Movva, S. Satpati, K. Kim, R. Dey, A. Rai, T. Pramanik, S. Guchhait, E. Tutuc, S. Banerjee, Structural and electrical properties of MoTe$_2$ and MoSe$_2$ grown by molecular beam epitaxy, ACS Appl. Mater. Interfaces 8 (2016) 7396–7402, https://doi.org/10.1021/acsami.6b00961.

[369] L. Walsh, R. Yue, Q. Wang, A. Barton, R. Addou, C. Smyth, H. Zhu, J. Kim, L. Colombo, M. Kim, R. Wallace, C. Hinkle, WTe$_2$ thin films grown by beam-interrupted molecular beam epitaxy, 2D Mater. 4 (2017), 025044, https://doi.org/10.1088/2053-1583/aa61e1.

[370] H. Diaz, R. Chaghi, Y. Ma, M. Batzill, Molecular beam epitaxy of the van der waals heterostructure MoTe$_2$ on MoS$_2$: phase, thermal, and chemical stability, 2D Mater. 4 (2015), 025094, https://doi.org/10.1088/2053-1583/2/4/044010.

[371] H. Diaz, Y. Ma, S. Kolekar, J. Avila, C. Chen, M. Asensio, M. Batzill, Substrate dependent electronic structure variations of van der waals heterostructures of MoSe$_2$ or MoSe$_{2(1-x)}$Te$_{2x}$ grown by van der waals epitaxy, 2D Mater. 4 (2017), 025094, https://doi.org/10.1088/2053-1583/aa6e6a.

[372] J. Zhou, F. Liu, J. Lin, X. Huang, J. Xia, B. Zhang, Q. Zeng, H. Wang, C. Zhu, L. Niu, X. Wang, W. Fu, P. Yu, T. Chang, C. Hsu, D. Wu, H. Jeng, Y. Huang, H. Lin, Z. Shen, C. Yang, L. Lu, K. Suenaga, W. Zhou, S.T. Pantelides, G. Liu, Z. Liu, Large-area and high-quality 2D transition metal telluride, Adv. Mater. 29 (2017), 1603471, https://doi.org/10.1002/adma.201603471.

[373] Y. Zhou, H. Jang, J.M. Woods, Y. Xie, P. Kumaravadivel, G.A. Pan, J. Liu, Y. Liu, D.G. Cahill, J.J. Cha, Direct synthesis of large-scale WTe$_2$ thin films with low thermal conductivity, Adv. Funct. Mater. 27 (2017), 1605928, https://doi.org/10.1002/adfm.201605928.

[374] Y. Tong, Y. Bouaziz, W. Zhang, B. Obeid, A. Loncle, H. Oughaddou, H. Enriquez, K. Chaouchi, V. Esaulov, Z. Chen, H. Xiong, Y. Cheng, A. Bendounan, Evidence of New 2D Material: Cu$_2$Te, 2D Mater, 2020, 035010, https://doi.org/10.1088/2053-1583/ab8918, 7.

[375] K. Lasek, P. Coelho, K. Zberecki, Y. Xin, S. Kolekar, J. Li, M. Batzill, Molecular beam epitaxy of transition metal (Ti-, V-, and Cr-) tellurides: from monolayer ditellurides to multilayer self-intercalation compounds, ACS Nano 14 (2020) 8473–8484, https://doi.org/10.1021/acsnano.0c02712.

[376] P. Coelho, H.-P. Komsa, H.C. Diaz, Y. Ma, A. Krasheninnikov, M. Batzill, Post-synthesis modifications of two-dimensional MoSe$_2$ or MoTe$_2$ by incorporation of excess metal atoms into the crystal structure, ACS Nano 12 (2018) 3975–3984, https://doi.org/10.1021/acsnano.8b01580.

[377] K. Lasek, M. Ghorbani-Asl, V. Pathirage, A.V. Krasheninnikov, M. Batzill, Controlling stoichiometry in ultrathin van der Waals films: PtTe$_2$, Pt$_2$Te$_3$, Pt$_3$Te$_4$, and Pt$_2$Te$_2$, ACS Nano 16 (2022) 9908–9919, https://doi.org/10.1021/acsnano.2c04303.

[378] L. Ju, J. Bie, J. Shang, X. Tang, L. Kou, Anus transition metal dichalcogenides: a superior platform for photocatalytic water splitting, J. Phys. Mater. 3 (2020), 022004, https://doi.org/10.1088/2515-7639/ab7c57.

[379] L. Zhang, Y. Xia, X. Li, L. Li, X. Fu, J. Cheng, R. Pan, Janus two-dimensional transition metal dichalcogenides, J. Appl. Phys. 131 (2022), 230902, https://doi.org/10.1063/5.0095203.

[380] A.-Y. Lu, H. Zhu, J. Xiao, C.-P. Chuu, Y. Han, M.-H. Chiu, C.-C. Cheng, C.-W. Yang, K.-H. Wei, Y. Yang, Y. Wang, D. Sokaras, D. Nordlund, P. Yang, D.A. Muller, M.-Y. Chou, X. Zhang, L.-J. Li, Janus monolayers of transition metal dichalcogenides, Nat. Nanotechnol. 12 (2017) 744–749, https://doi.org/10.1038/nnano.2017.100.

[381] J. Zhang, S. Jia, I. Kholmanov, L. Dong, D. Er, W. Chen, H. Guo, Z. Jin, V. B. Shenoy, L. Shi, J. Lou, Janus monolayer transition-metal dichalcogenides, ACS Nano 11 (2017) 8192–8198, https://doi.org/10.1021/acsnano.7b03186.

[382] R. Sant, M. Gay, A. Marty, S. Lisi, R. Harrabi, C. Vergnaud, M.T. Dau, X. Weng, J. Coraux, N. Gauthier, O. Renault, G. Renaud, M. Jamet, Synthesis of epitaxial monolayer Janus SPtSe, npj 2D Mater, Appl 4 (2020) 41, https://doi.org/10.1038/s41699-020-00175-z.

[383] S. Mahatha, M. Dendzik, C. Sanders, M. Michiardi, M. Bianchi, J. Miwa, P. Hofmann, Quasi-free-standing single-layer WS$_2$ achieved by intercalation,

Phys. Rev. Mater. 2 (2018), 124001, https://doi.org/10.1103/PhysRevMaterials.2.124001.

[384] Y. Yu, G. Li, L. Huang, A. Barrette, Y.-Q. Cai, Y. Yu, K. Gundogdu, Y.-W. Zhang, L. Cao, Enhancing multifunctionalities of transition-metal dichalcogenide monolayers via cation intercalation, ACS Nano 11 (2017) 9390–9396, https://doi.org/10.1021/acsnano.7b04880.

[385] R. Sant, S. Lisi, V.D. Nguyen, E. Mazaleyrat, A.C.G. Herrero, O. Geaymond, V. Guisset, P. David, A. Marty, M. Jamet, C. Chapelier, L. Magaud, Y.J. Dappe, M. Bianchi, P. Hofmann, G. Renaud, J. Coraux, Decoupling molybdenum disulfide from its substrate by cesium intercalation, J. Phys. Chem. C 124 (2020) 12397–12408, https://doi.org/10.1021/acs.jpcc.0c00970.

[386] A. Tedstone, D. Lewis, P. O'Brien, Synthesis, properties, and applications of transition metal-doped layered transition metal dichalcogenides, Chem. Mater. 28 (2016) 1965–1974, https://doi.org/10.1021/acs.chemmater.6b00430.

[387] S. Park, A.T. Garcia-Esparza, H. Abroshan, B. Abraham, J. Vinson, A. Gallo, D. Nordlund, J. Park, T.R. Kim, L. Vallez, R. Alonso-Mori, D. Sokaras, X. Zheng, Operando study of thermal oxidation of monolayer MoS₂, Adv. Sci. 8 (2021), 2002768, https://doi.org/10.1002/advs.202002768.

[388] M. Vera-Hidalgo, E. Giovanelli, C. Navío, E.M. Pérez, Mild covalent functionalization of transition metal dichalcogenides with maleimides: a "click" reaction for 2H-MoS₂ and WS₂, J. Am. Chem. Soc. 141 (2019) 3767–3771, https://doi.org/10.1021/jacs.8b10930.

[389] S.M. Gali, D. Beljonne, Combined healing and doping of transition metal dichalcogenides through molecular functionalization, J. Mater. Chem. C 9 (2021) 16247–16256, https://doi.org/10.1039/d1tc01329g.

[390] K. Qi, X. Cui, L. Gu, S. Yu, X. Fan, M. Luo, S. Xu, N. Li, L. Zheng, Q. Zhang, J. Ma, Y. Gong, F. Lv, K. Wang, H. Huang, W. Zhang, S. Guo, W. Zheng, P. Liu, Single-atom cobalt array bound to distorted 1T-MoS₂ with ensemble effect for hydrogen evolution catalysis, Nat. Commun. 10 (2019) 5231, https://doi.org/10.1038/s41467-019-12997-7.

[391] P. Ranjan, J.M. Lee, P. Kumar, A. Vinu, Borophene: new sensation in flatland, Adv. Mater. 32 (2020) 2000531, https://doi.org/10.1002/adma.202000531.

[392] Z. Xie, X. Meng, X. Li, W. Liang, W. Huang, K. Chen, J. Chen, C. Xing, M. Qiu, B. Zhang, G. Nie, N. Xie, X. Yan, H. Zhang, Two-dimensional borophene: properties, fabrication, and promising applications, Research 2020 (2020), 2624617, https://doi.org/10.34133/2020/2624617.

[393] C. Hou, G. Tai, Z. Wu, J. Hao, Borophene: current status, challenges and opportunities, ChemPlusChem 85 (2020) 2186–2196, https://doi.org/10.1002/cplu.202000550.

[394] D. Ciuparu, R.F. Klie, Y. Zhu, L. Pfefferle, Synthesis of pure boron single-wall nanotubes, J. Phys. Chem. B 108 (2004) 3967–3969, https://doi.org/10.1002/chin.200426199.

[395] H.-J. Zhai, Y.-F. Zhao, W.-L. Li, Q. Chen, H. Bai, H.-S. Hu, Z.A. Piazza, W.-J. Tian, H.-G. Lu, Y.-B. Wu, Y.-W. Mu, G.-F. Wei, Z.-P. Liu, J. Li, S.-D. Li, L.-S. Wang, Observation of an all-boron fullerene, Nat. Chem. 6 (2014) 727–731, https://doi.org/10.1038/nchem.1999.

[396] P. Ranjan, T.K. Sahu, R. Bhushan, S.S. Yamijala, D.J. Late, P. Kumar, A. Vinu, Freestanding borophene and its hybrids, Adv. Mater. 31 (2019), 1900353, https://doi.org/10.1002/adma.201900353.

[397] A.J. Mannix, X.-F. Zhou, B. Kiraly, J.D. Wood, D. Alducin, B.D. Myers, X. Liu, B. L. Fisher, U. Santiago, J.R. Guest, M.J. Yacaman, A. Ponce, A.R. Oganov, M. C. Hersam, N.P. Guisinger, Synthesis of borophenes: anisotropic, two-dimensional boron polymorphs, Science 350 (2015) 1513–1516, https://doi.org/10.1126/science.aad1080.

[398] W.-L. Li, X. Chen, T. Jian, T.-T. Chen, J. Li, L.-S. Wang, From planar boron clusters to boronenes and metalloborophenes, Nat. Rev. Chem 1 (2017), 0071, https://doi.org/10.1038/s41570-017-0071.

[399] B. Albert, H. Hillebrecht, Boron: elementary challenge for experimenters and theoreticians, Angew. Chem. Int. Ed. 48 (46) (2009) 8640–8668, https://doi.org/10.1002/anie.200903246, arXiv:https://onlinelibrary.wiley.com/doi/pdf/10.1002/anie.200903246, https://onlinelibrary.wiley.com/doi/abs/10.1002/anie.200903246.

[400] H. Bergeron, D. Lebedev, M.C. Hersam, Polymorphism in post-dichalcogenide two-dimensional materials, Chem. Rev. 121 (2021) 2713–2775, https://doi.org/10.1021/acs.chemrev.0c00933.

[401] E.S. Penev, S. Bhowmick, A. Sadrzadeh, B.I. Yakobson, Polymorphism of two-dimensional boron, Nano Lett. 12 (2012) 2441–2445, https://doi.org/10.1021/nl3004754.

[402] G.P. Campbell, A.J. Mannix, J.D. Emery, T.-L. Lee, N.P. Guisinger, M.C. Hersam, M.J. Bedzyk, Resolving the chemically discrete structure of synthetic borophene polymorphs, Nano Lett. 18 (2018) 2816 2821, https://doi.org/10.1021/acs.nanolett.7b05178.

[403] M.G. Cuxart, K. Seufert, V. Chesnyak, W.A. Waqas, A. Robert, M.-L. Bocquet, G. S. Duesberg, H. Sachdev, W. Auwärter, Borophenes made easy, Sci. Adv. 7 (2021), eabk1490, https://doi.org/10.1126/sciadv.abk1490.

[404] B. Feng, J. Zhang, Q. Zhong, W. Li, S. Li, H. Li, P. Cheng, S. Meng, L. Chen, K. Wu, Experimental realization of two-dimensional boron sheets, Nat. Chem. 8 (2016) 563–568, https://doi.org/10.1038/nchem.2491.

[405] X. Liu, L. Wang, S. Li, M.S. Rahn, B.I. Yakobson, M.C. Hersam, Geometric imaging of borophene polymorphs with functionalized probes, Nat. Commun. 10 (2019) 1642, https://doi.org/10.1038/s41467-019-09686-w.

[406] Q. Zhong, L. Kong, J. Gou, W. Li, S. Sheng, S. Yang, P. Cheng, H. Li, K. Wu, L. Chen, Synthesis of borophene nanoribbons on Ag(110) surface, Phys. Rev. Mater. 1 (2017), 021001, https://doi.org/10.1103/physrevmaterials.1.021001.

[407] B. Kiraly, X. Liu, L. Wang, Z. Zhang, A.J. Mannix, B.L. Fisher, B.I. Yakobson, M. C. Hersam, N.P. Guisinger, Borophene synthesis on Au(111), ACS Nano 13 (2019) 3816–3822, https://doi.org/10.1021/acsnano.8b09339.

[408] R. Wu, I.K. Drozdov, S. Eltinge, P. Zahl, S. Ismail-Beigi, I. Božović, A. Gozar, Large-area single-crystal sheets of borophene on cu(111) surfaces, Nat. Nanotechnol. 14 (1) (2019) 44–49, https://doi.org/10.1038/s41565-018-0317-6.

[409] N.A. Vinogradov, A. Lyalin, T. Taketsugu, A.S. Vinogradov, A. Preobrajenski, Single-phase borophene on Ir(111): formation, structure, and decoupling from the support, ACS Nano 13 (2019) 14511–14518, https://doi.org/10.1021/acsnano.9b08296.

[410] K.M. Omambac, M. Petrović, P. Bampoulis, C. Brand, M.A. Kriegel, P. Dreher, D. Janoschka, U. Hagemann, N. Hartmann, P. Valerius, T. Michely, F.J. M. z. Heringdorf, M.H.-v. Hoegen, Segregation-enhanced epitaxy of borophene on Ir (111) by thermal decomposition of borazine, ACS Nano 15 (2021) 7421–7429, https://doi.org/10.1021/acsnano.1c00819.

[411] W. Li, L. Kong, C. Chen, J. Gou, S. Sheng, W. Zhang, H. Li, L. Chen, P. Cheng, K. Wu, Experimental realization of honeycomb borophene, Sci. Bull. 63 (2018) 282–286, https://doi.org/10.1016/j.scib.2018.02.006.

[412] A.B. Preobrajenski, A. Lyalin, T. Taketsugu, N.A. Vinogradov, A.S. Vinogradov, Honeycomb boron on Al(111): from the concept of borophene to the two-dimensional boride, ACS Nano 15 (2021) 15153–15165, https://doi.org/10.1021/acsnano.1c05603.

[413] A.J. Mannix, Z. Zhang, N.P. Guisinger, B.I. Yakobson, M.C. Hersam, Borophene as a prototype for synthetic 2D materials development, Nat. Nanotechnol. 13 (2018) 444 450, https://doi.org/10.1038/s41565-018-0157-4.

[414] Y.V. Kaneti, D.P. Benu, X. Xu, B. Yuliarto, Y. Yamauchi, D. Golberg, Borophene: two-dimensional boron monolayer: synthesis, properties, and potential applications, Chem. Rev. 122 (2022) 1000–1051, https://doi.org/10.1021/acs.chemrev.1c00233.

[415] N. Mounet, M. Gibertini, P. Schwaller, D. Campi, A. Merkys, A. Marrazzo, T. Sohier, I.E. Castelli, A. Cepellotti, G. Pizzi, N. Marzari, Two-dimensional materials from high-throughput computational exfoliation of experimentally known compounds, Nat. Nanotechnol. 13 (2018) 246–252, https://doi.org/10.1038/s41565-017-0035-5.

[416] M. Batzill, U. Diebold, The surface and materials science of tin oxide, Prog. Surf. Sci. 79 (2005) 47–154, https://doi.org/10.1016/j.progsurf.2005.09.002.

[417] J. Azadmanjiri, P. Kumar, V.K. Srivastava, Z. Sofer, Surface functionalization of 2D transition metal oxides and dichalcogenides via covalent and non-covalent bonding for sustainable energy and biomedical applications, ACS Appl. Nano Mater. 3 (2020) 3116–3143, https://doi.org/10.1021/acsanm.0c00120.

[418] H.T. Tan, W. Sun, L. Wang, Q. Yan, 2D transition metal oxides/hydroxides for energy-storage applications, ChemNanoMat 2 (2016) 562–577, https://doi.org/10.1002/cnma.201500177.

[419] T. Yang, T.T. Song, M. Callsen, J. Zhou, J.W. Chai, Y.P. Feng, S.J. Wang, M. Yang, Atomically thin 2D transition metal oxides: structural reconstruction, interaction with substrates, and potential applications, Adv. Mater. Interfac. 6 (2019), 1801160, https://doi.org/10.1002/admi.201801160.

[420] Y. Gogotsi, B. Anasori, The rise of MXenes, ACS Nano 13 (2019) 8491–8494, https://doi.org/10.1021/acsnano.9b06394.

[421] X. Wu, Y. Ke, Z. Wang, W. Zhang, A.T.S. Wee, The metallic nature of two-dimensional transition-metal dichalcogenides and MXenes, Surf. Sci. Rep. 76 (2021), 100542, https://doi.org/10.1016/j.surfrep.2021.100542.

[422] M. Salmeron, R. Schlögl, Ambient pressure photoelectron spectroscopy: a new tool for surface science and nanotechnology, Surf. Sci. Rep. 63 (4) (2008) 169–199, https://doi.org/10.1016/j.surfrep.2008.01.001.

[423] S. Yamamoto, H. Bluhm, K. Andersson, G. Ketteler, H. Ogasawara, M. Salmeron, A. Nilsson, In situ x-ray photoelectron spectroscopy studies of water on metals and oxides at ambient conditions, J. Phys. Condens. Matter 20 (18) (2008), 184025, https://doi.org/10.1088/0953-8984/20/18/184025.

[424] D.E. Starr, Z. Liu, M. Hävecker, A. Knop-Gericke, H. Bluhm, Investigation of solid/vapor interfaces using ambient pressure X-ray photoelectron spectroscopy, Chem. Soc. Rev. 42 (2013) 5833–5857, https://doi.org/10.1039/C3CS60057B.

[425] V. Pérez-Dieste, L. Aballe, S. Ferrer, J. Nicolàs, C. Escudero, A. Milán, E. Pellegrin, Near ambient pressure XPS at ALBA, J. Phys.: Conf. Ser. 425 (7) (2013), 072023, https://doi.org/10.1088/1742-6596/425/7/072023.

[426] S. Zhu, M. Scardamaglia, J. Kundsen, R. Sankari, H. Tarawneh, R. Temperton, L. Pickworth, F. Cavalca, C. Wang, H. Tissot, J. Weissenrieder, B. Hagman, J. Gustafson, S. Kaya, F. Lindgren, I. Källquist, J. Maibach, M. Hahlin, V. Boix, T. Gallo, F. Rehman, G. D'Acunto, J. Schnadt, A. Shavorskiy, HIPPIE: a new platform for ambient-pressure X-ray photoelectron spectroscopy at the MAX IV Laboratory, J. Synchrotron Radiat. 28 (2) (2021) 624–636, https://doi.org/10.1107/S160057752100103X.